bioRxiv preprint doi: https://doi.org/10.1101/2021.05.06.442886; this version posted September 4, 2021. The copyright holder for this preprint (which was not certified by peer review) is the author/funder, who has granted bioRxiv a license to display the preprint in perpetuity. It is made available under aCC-BY-NC-ND 4.0 International license.

Toward Reliable Network Neuroscience for Mapping Individual Differences

Chao Jiang[1,2,3], **Richard Betzel**[4], **Ye He**[5], **Yin-Shan Wang**[1,6,7], **Xiu-Xia Xing**[8] ✉, **and Xi-Nian Zuo**[1,3,6,7] ✉

[1]State Key Laboratory of Cognitive Neuroscience and Learning, Beijing Normal University, Beijing 100875, China
[2]School of Psychology, Capital Normal University, Beijing 100048, China
[3]Institute of Psychology, Chinese Academy of Sciences, Beijing 100101, China
[4]Department of Psychological and Brain Sciences, Indiana University, Bloomington, United States
[5]School of Artificial Intelligence, Beijing University of Posts and Telecommunications, Beijing 100876, China
[6]National Basic Science Data Center, Beijing 100190, China
[7]IDG/McGovern Institute for Brain Research, Beijing Normal University, Beijing 100875, China
[8]Department of Applied Mathematics, College of Mathematics, Faculty of Science, Beijing University of Technology, Beijing 100124, China

A rapidly emerging application of network neuroscience in neuroimaging studies has provided useful tools to understand individual differences in complex brain function. However, the variability of methodologies applied across studies - with respect to node definition, edge construction, and graph measurements- makes it difficult to directly compare findings and also challenging for end users to select the optimal strategies for mapping individual differences in brain networks. Here, we aim to provide a benchmark for best practices by systematically comparing the reliability of human brain network measurements of individual differences under different analytical strategies using the test-retest design of the resting-state functional magnetic resonance imaging from the Human Connectome Project. The results uncovered four essential principles to guide reliable network neuroscience of individual differences: 1) use a whole brain parcellation to define network nodes, including subcortical and cerebellar regions, 2) construct functional connectome using spontaneous brain activity in multiple slow bands, 3) optimize topological economy of networks at individual level, 4) characterise information flow with metrics of integration and segregation.

connectome | individual difference | reliability | fMRI | open science
Correspondence: *xinian.zuo@bnu.edu.cn, xingxx@bjut.edu.cn*

Over the past two decades, network neuroscience has helped transform the field of neuroscience (1), providing a quantitative methodology framework for modeling brains as graphs (or networks) composed of nodes (brain regions) and edges (their connections), namely connectomics (2). The organization and topology of macro-scale brain networks can be characterized by a growing suite of connectomic measurements including efficiency, centrality, clustering, small-word topology, rich-club, etc (3–5). In parallel, resting-state fMRI (rfMRI) has opened up new avenues towards understanding the human brain function (6). In conjunction with network neuroscience, rfMRI has led to the emergence of a multidisciplinary field, functional connectomics or functional network neuroscience (FNN) (7–9), in which the brain's intrinsic, interregional connectivity is estimated from rfMRI recordings. FNN has been widely used to investigate the system-level organization of the human brain function (10) and its relationship with individual differences (11) in developmental (12), socio-cultural (13) and clinical conditions (14).

An important topic in FNN and, indeed, any scientific discipline, is the notion of measurement reliability. In general, reliability characterises a proportion of measurement variability between different subjects relative to the overall variability including both between-subject and within-subject (i.e., random) components (15), and is commonly used to assess the consistency or agreement between measurements. However, measurement reliability can also serve as a measure of discriminablity. For example, if a measurement can sufficiently capture individual characteristics, its reliability will be higher than measurements that underestimate between-subject variability. Thus, high reliability is essential for any measurement to better differentiate a group of individuals, i.e., inter-individual differences (16). Recent studies have demonstrated that the reliability of measurements is equivalent to the fingerprint or discriminablity of the measurement under the Gaussian distribution (17) while it has well-established statistical theory and applications to psychology (i.e., psychometric theory) (18) and medicine (i.e., diagnosis theory) (19). Reliability also provides an upper bound of the measurement validity (5, 16), which cannot be readily quantified as the reliability (16). Therefore, high levels of reliability is the first and most basic requirement for quantifying individual differences in FNN. Accordingly, the optimization of measurement reliability of the individual differences can help guide FNN processing and analysis pipelines for neurodevelopmental (20) and clinical applications (21).

Previous studies have demonstrated that many measurements made on networks estimated from rfMRI have limited reliability (22, 23). These low levels of reliability could be an indication of failure in handling individual variability at different levels (24, 25). In particular, experimental design and processing decisions related to scan duration, determining frequency range, and regressing global signal have impacts on rfMRI measurements and thus their reliability (23, 26). Although less focused on reliability, existing studies also revealed that their findings are influenced by choices of parcellation templates (27), edge construction and definition, and choice of graph metrics (28). How these decisions affect the reliability of FNN measurements deserves further investigation. These analytical choices have been implemented in different software packages (29) but can vary from one package

bioRxiv preprint doi: https://doi.org/10.1101/2021.05.06.442886; this version posted September 4, 2021. The copyright holder for this preprint (which was not certified by peer review) is the author/funder, who has granted bioRxiv a license to display the preprint in perpetuity. It is made available under aCC-BY-NC-ND 4.0 International license.

to another in terms of their parameterization. Beyond limited examinations on reliability (30–32), a systematic investigation into the reliability of FNN measurements is warranted to guide FNN software use and analyses.

In this paper, we conducted a systematic FNN reliability analysis using the test-retest rfMRI data from the Human Connectome Project (HCP) (33). Note that the HCP imaging acquisition settings and data pre-processing have integrated various strategies to optimize the measurement reliability (22, 34). We thus analyzed the minimally pre-processed HCP rfMRI data and focused our work on four key post-processing stages: node definition, edge construction, network measurement, and reliability assessments. In the end, we propose a set of principles to guide researchers in performing reliable FNN, advancing the field-standard call for the best practices in network neuroscience. Toward an open FNN, we released all the codes and reliability data by building an online platform for sharing the data and computational resources.

Results

A typical analysis pipeline in FNN includes steps for node definition (parcellations) and edge construction (frequency bands, connectivity estimation and filtering schemes) (Fig. 1a). To determine an optimal pipeline, our aim is to combine the most reliable strategies across different parts of the analysis by comparing the reliability of derived global network metrics. The HCP test-retest data were employed for reliability evaluation (Fig. 1b) using the intraclass correlation (ICC) statistics on the measurement reliability with five levels (36): $0 < \mathrm{ICC} \leq 0.2$ (**slight**); $0.2 < \mathrm{ICC} \leq 0.4$ (**fair**); $0.4 < \mathrm{ICC} \leq 0.6$ (**moderate**); $0.6 < \mathrm{ICC} \leq 0.8$ (**substantial**); and $0.8 < \mathrm{ICC} < 1.0$ (**almost perfect**). Our analyses produce massive amounts of reliability statistics: 524,160 ICCs. In this section we first present overall reliability assessments associated with the various analytic strategies as well as their impact on between- and within-subject variability (Fig. 1c). We then determine the optimized pipelines based on the highest reliability measurements, while documenting the derived both global and local network metrics and both their reliability and variability at an individual level. Based upon these results, we built the open resources for reliable FNN, including all the codes, reliability matrices and computation *via* an online platform (`http://ibraindata.com/research/reliablenetworkneuroscience`).

Whole brain networks are more reliable than cortical networks. Elements derived from a brain parcellation (i.e., parcel) define the network nodes. Here, we evaluated reliability based on 24 different parcellation choices (Fig. 2a, see more details of these parcellations in **Online Methods**). In the following parts of the paper, we name a parcellation as '*ParcAbbr-NumberOfParcels*' (e.g., LGP-100 or its whole-brain version wbLGP-458).

We found significant differences in ICC distributions across the 24 parcellation choices (Fig. 2b, Friedman rank sum test: $\chi^2 = 20379.07, df = 23, p < 2.2 \times 10^{-16}$, effect size $W_{\mathrm{Kendall}} = 0.377$). The mean ICCs range from slight (LGP-1000) to substantial (wbLGP-458). Given a particular parcellation and definition of nodes, we illustrate the density distribution of its ICCs under all other strategies (edge definition and metric derivation). Notably, whole-brain parcellations yield higher measurement reliability than parcellations of cerebral cortex on their own (the effect sizes > 0.65). This improvement in reliability seems not simply a bi-product of having more parcels. We chose the parcellations in which the number of parcels ($400 \leq n \leq 1000$) almost overlapped between the cortex and the whole brain, and found no correlation between the number of parcels and the median ICCs ($r = -0.11, p = 0.7$). We report the mean ICC and the number of almost perfect (noap) ICCs (≥ 0.8) as the descriptive statistics for the density distributions. The wbLGP-458 (mean ICC: 0.671; noap ICC: 519), wbLGP-558 (mean ICC: 0.671; noap ICC: 540) and The wbBNP-568 (mean ICC: 0.664; noap ICC: 511) are the three most reliable choices (see more details of the post-hoc Wilcoxon signed rank test in Table S7). Among the cortical parcellations, the LGP-500 (mean ICC: 0.362; noap ICC: 0), LGP-400 (mean ICC: 0.342; noap ICC: 0) and LGP-600 (mean ICC: 0.340; noap ICC: 0) are the three most reliable choices (Table S3).

To better understand the effect of introducing 358 subcortical parcels into the cortical parcellations, we decomposed the reliability changes into a two-dimensional representation of changes of individual variability (Fig. 2c,d). This idea was motivated by the analysis of reliability derived with individual variability (15, 16) as in Fig. 1c. For each ICC under a given parcellation choice, we calculated the related between-subject variability V_b and within-subject variability V_w. Changes in the individual variability associated with the reliability improvements from cortical to whole-brain pipelines were plotted along with ΔV_b and ΔV_w as arrows. These arrows are distributed across the three quadrants (quadI: 0.94%; quadII: 59.99%; quadIII: 39.07%). We noticed that most of these arrows were distributed into the optimal quadrant where the improvements of test-retest reliability by the whole-brain parcellation choices largely attributing to the increases of between-subject variability and decreases of within-subject variability. The decreases of both between-subject and within-subject variability may also strengthen the measurement reliability (the suboptimal quadIII in Fig. 2).

Spontaneous brain activity portrays more reliable networks in higher slow bands. Brain oscillations are hierarchically organized, and their frequency bands were theoretically driven by the natural logarithm linear law (35, 37). By analogy, rfMRI oscillations can, similarly, be partitioned into distinct frequency bands. Advanced by the fast imaging protocols (TR = 720ms), HCP test-retest data allows to obtain more oscillation classes than traditional rfMRI acquisitions (typical TR = 2s). We incorporate the Buzsáki's framework (35, 38) with the HCP dataset using the DREAM toolbox (39) in the Connectome Computation System (29) to decompose the time series into the six slow bands (Fig. 3a):

- **slow-6** (0.0069-0.0116 Hz)
- **slow-5** (0.0116-0.0301 Hz)

bioRxiv preprint doi: https://doi.org/10.1101/2021.05.06.442886; this version posted September 4, 2021. The copyright holder for this preprint (which was not certified by peer review) is the author/funder, who has granted bioRxiv a license to display the preprint in perpetuity. It is made available under aCC-BY-NC-ND 4.0 International license.

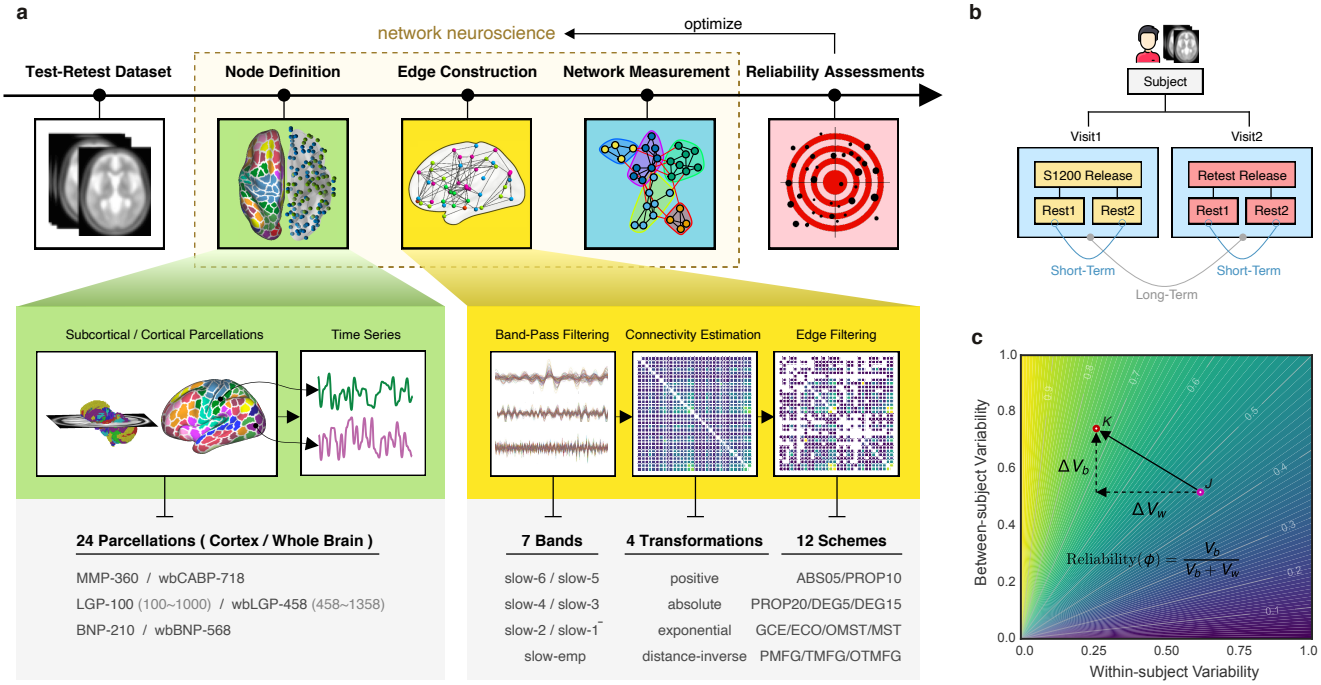

Fig. 1. Analytical pipelines for reliable FNN. a) There are five stages during our analyses: (1) test-retest dataset (white box) downloaded from HCP website, (2) node definition (green box) defining nodes using a set of brain areas of 24 different partitions of the human brain, (3) edge construction (yellow box) estimating individual correlation matrices using the six frequency bands (slow 1-6) from Buzsáki's theoretical framework on the brain oscillations (35) as well as the widely used empirical frequency band (Slow-emp) (6) and transferring these matrices into adjacency matrices using $7 \times 4 \times 12$ different strategies on edge construction including band-pass filtering, connectivity estimation and edge filtering, (4) network analysis (blue box) systematically calculating various brain graph metrics on measurements of information flow, and (5) reliability assessment (red box) evaluating test-retest reliability with massive linear mixed models. b) The test-retest data shared multimodal MRI datasets of 46 subjects in the HCP S1200 release and the HCP Retest release. Each subject underwent the first four test scans on two days (two scans per day: Rest1 and Rest2) and return several months later to finish the four retest scans on another two days. This was designed for evaluation of both the short-term (Rest1 vs. Rest2) and the long-term (Visit1 vs. Visit2) reliability. c) Measurement reliability refers to the inter-individual or between-subject variability V_b relative to the intra-individual or within-subject variability V_w. Variability of both between-subject (V_b) and within-subject (V_w) are normalized into between 0 and 1 by the total sample variances. Their changes (ΔV_b and ΔV_w) introduce a reliability gradient as represented by the vector (the black arrow). The length of the arrow reflects the amplitude of reliability changes when the reliability assessment from one choice (pink circle, J) to another choice (red circle, K). Further, the arrow's direction ($\mathbf{JK}$) indicates the sources of this reliability change. Here the reliability becomes from moderate to substantial level with increases of between-subject variability ($\Delta V_b > 0$) and decreases of within-subject variability ($\Delta V_w < 0$).

- **slow-4** (0.0301-0.0822 Hz)
- **slow-3** (0.0822-0.2234 Hz)
- **slow-2** (0.2234-0.6065 Hz)
- **slow-1**$^-$ (0.6065-0.6944 Hz)

We noticed that, due to the limited sampling rate (TR), this **slow-1**$^-$ only covers a small part of the full **slow-1** band (0.6065-1.6487 Hz) – we indicate this above. We also included the frequency band, **slow-emp** (0.01-0.08 Hz) for the sake of comparison, as it is covers a range commonly used in rfMRI studies. A significant effect on order ($\chi^2 = 9283.536, df = 6, p < 2.2 \times 10^{-16}, W_{\text{Kendall}} = 0.192$) across the frequency bands was revealed based on the density distributions of ICC (Fig. 3b): slow-2, slow-1$^-$, slow-3, slow-emp, slow-4, slow-5, slow-6. Post-hoc paired tests indicated that any pairs of neighbouring bands are significantly different from one another (for more details, see Table S9-13), with measurement reliability increasing with faster frequency bands. Note, however, that slow-1$^-$ (mean ICC: 0.564) did not fit into this trend, possibly due to its limited coverage of the full band. But remarkably, slow-1$^-$ exhibited the largest number of almost prefect ICCs for potential reliability (noap ICC: 1746, for more details, see Figure S8). Slow-emp (mean ICC: 0.519; noap ICC: 434) contains overlapping frequencies with both slow-4 (mean ICC: 0.560; noap ICC: 441) and slow-5 (mean ICC: 0.494; noap ICC: 285), and higher ICCs than the two bands but the effect sizes are small to moderate (slow-emp vs. slow-4: 0.193; slow-emp vs. slow-5: 0.485). Slow-6 is the choice with the lowest ICCs (mean ICC: 0.331; noap ICC: 154) compared to other bands (large effect sizes: $r > 0.57$).

To visualize variation in reliability across frequency bands, we plotted a trajectory tracing reliability flow along the five full (slow-6 to 2) bands in the reliability plane, whose axes correspond to between- *versus* within-subject variability (Fig. 3c). As expected, this nonlinear trajectory contains two stages of almost linear changes of the network measurement reliability from slow to fast oscillations: whole brain versus cortex. In each case, the reliability improvements attribute to both increases of between-subject variability and decreases of within-subject variability while the improvements of whole-brain network measurement reliability were largely driven by the increased variability between subjects.

Topological economics individualize highly reliable functional brain networks. Estimating functional connections can be highly challenging due to the absence of a

bioRxiv preprint doi: https://doi.org/10.1101/2021.05.06.442886; this version posted September 4, 2021. The copyright holder for this preprint (which was not certified by peer review) is the author/funder, who has granted bioRxiv a license to display the preprint in perpetuity. It is made available under aCC-BY-NC-ND 4.0 International license.

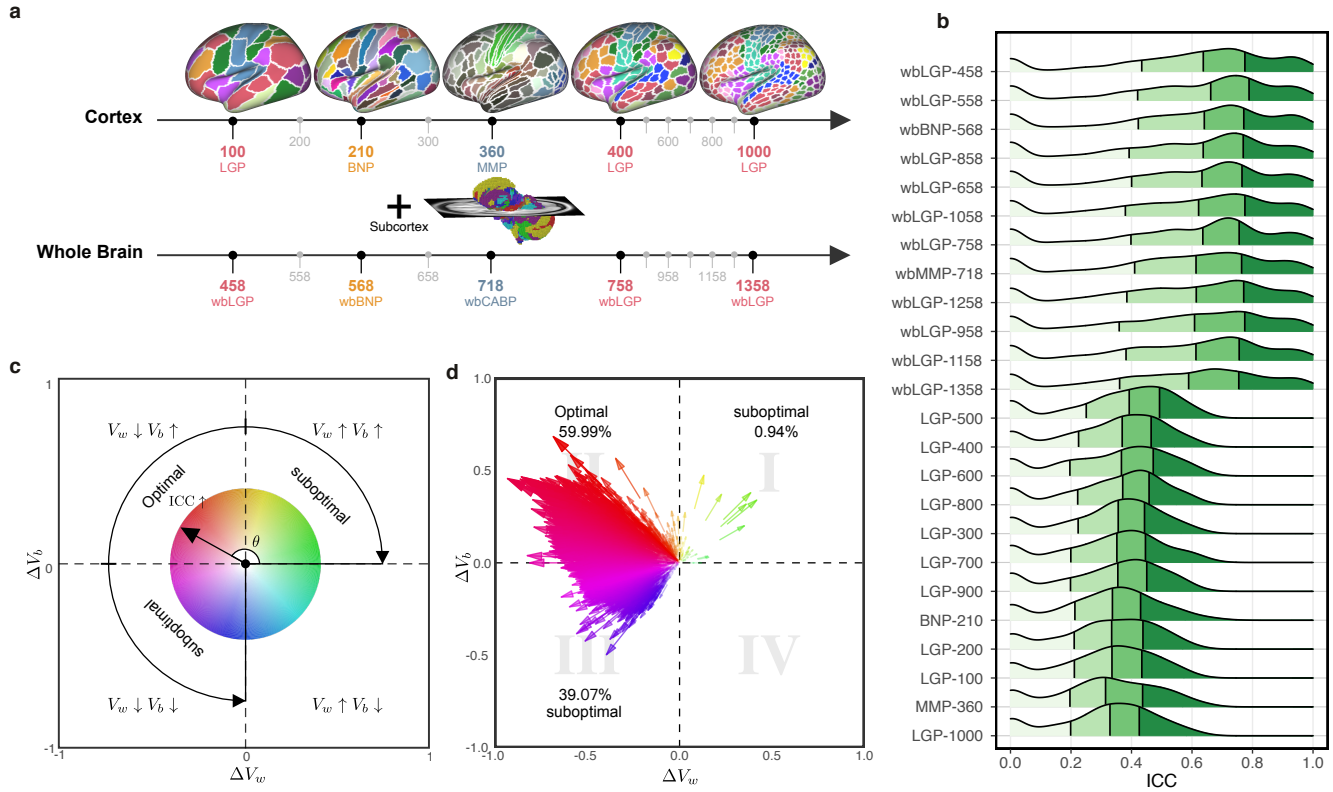

Fig. 2. Parcellation choices impact measurement reliability and individual variability. a) Node definitions are derived from different resolutions of spatial parcellation on the human cortex and whole brain (see more details of these name abbreviations in **Online Methods**). b) Density plots are visualized for distributions of the ICCs under the various parcellation choices on node definition. These density distributions are ranked from top to bottom according to decreases of the mean ICCs while the four colors depict the four quantiles. c) Reliability gradient between any one whole-brain parcellation choice and its corresponding cortical parcellation choice is decomposed into the axis of changes of the between-subject variability (ΔV_b) and the axis of changes of the within-subject variability (ΔV_w). This gradient can be represented as an vector, which is the black arrow from the origin with an angle θ with the $x-$axis while the color encodes this angle and the transparency or the length reflects the magnitude of the degree of ICC improvement. According to the anatomy of reliability, the optimal space is in the second quadrant (quadII) while the first and third quadrant (quadI and quadIII) are suboptimal for reliability. d) Improvements of reliability by the whole-brain node definition pipelines are represented as gradient arrows in the plane of individual variability.

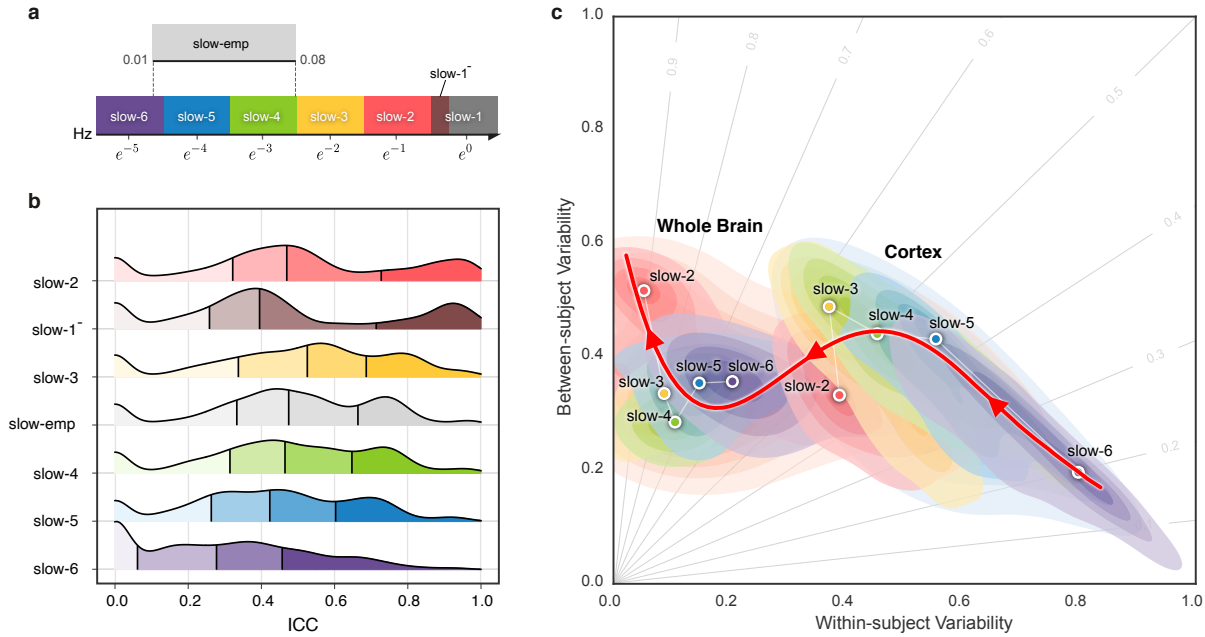

Fig. 3. Reliability gradient across the slow bands and changes of related individual variability. a) Classes of frequency bands for slow oscillations derived from the natural logarithm linear law (35, 37). b) Density plots are visualized for the ICC distributions under the various frequency bands. These density distributions are ranked from top to bottom according to decreases of the mean ICCs while the vertical lines depict the four quartiles. c) Network measurements are projected onto the reliability anatomy plane coordinated by both between- and within-subject variability. These dot plots are fitted into the topographic (contour) maps where the local maxima for each band is labeled as a circle. The red line shows the entire modeled trajectory tracing the reliability flow along slow-to-fast oscillations in cortex and whole brain.

bioRxiv preprint doi: https://doi.org/10.1101/2021.05.06.442886; this version posted September 4, 2021. The copyright holder for this preprint (which was not certified by peer review) is the author/funder, who has granted bioRxiv a license to display the preprint in perpetuity. It is made available under aCC-BY-NC-ND 4.0 International license.

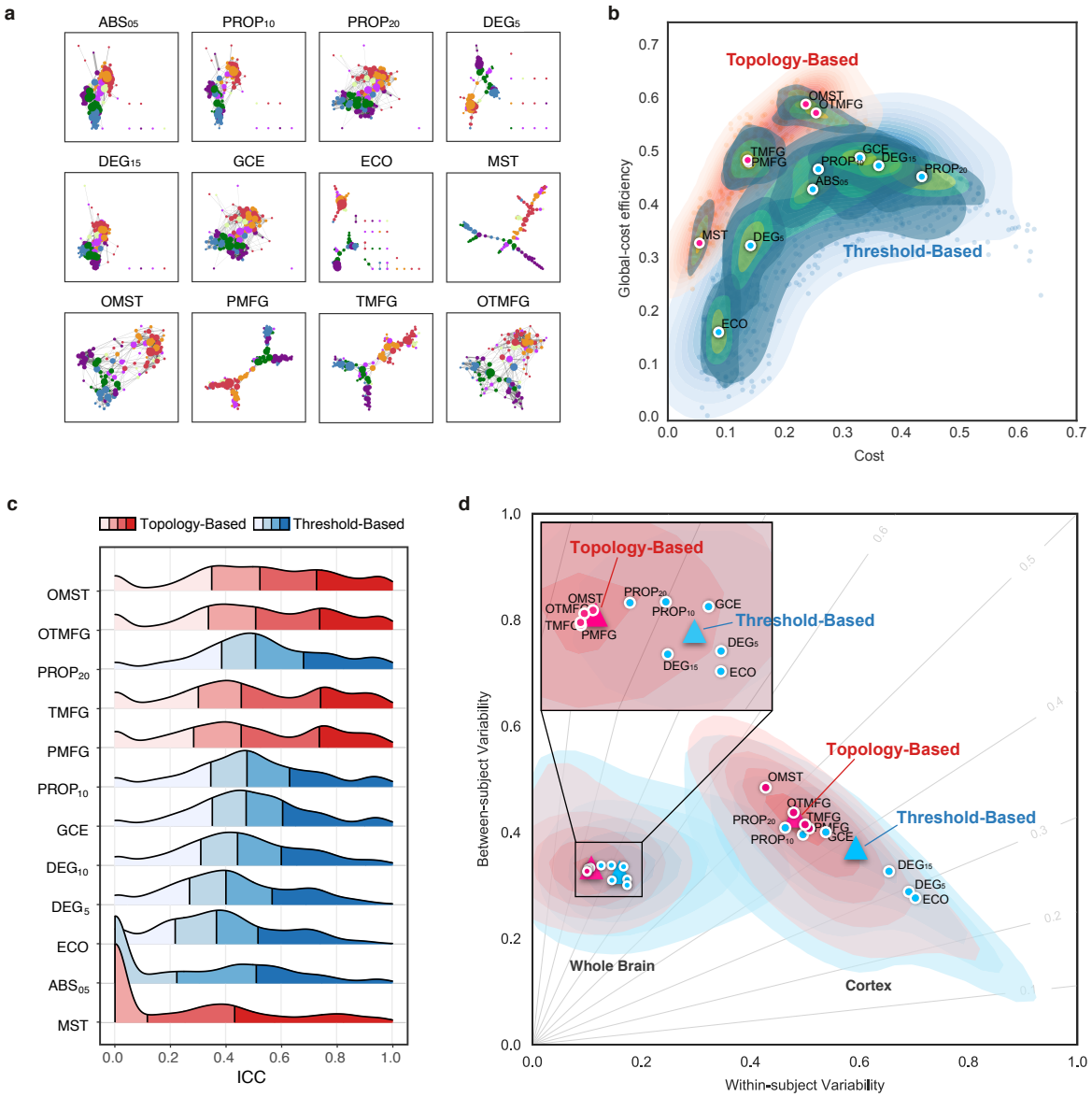

Fig. 4. Edge filtering schemes and their networking performance. (a) Twelve schemes of filtering edge are applied to an individual connectivity matrix, resulting in the 12 brain networks with their nodes colored as the Yeo2011-7Networks (40). (b) Global cost efficiency are plotted against network wiring costs of all the brain networks derived with the 12 edge filtering schemes from all the individual rfMRI scans. Red dots represent the topology-based while blue dots are for threshold-based networks. These dot plots are fitted into the topographic (contour) maps where the local maxima for each filtering choice is labeled as a circle. (c) Density plots are for ICC distributions under various the 12 edge filtering schemes. These density distributions are ranked from top to bottom according to decreases of the mean ICCs while the two colors depict the topology-based and threshold-based schemes. Four quartiles were indicated by vertical lines. (d) Network measurements are projected onto the reliability anatomy plane coordinated by both between- and within-subject variability. Red dots represent the topology-based while blue dots are for threshold-based networks. The topographic (contour) maps fit the dots and label the local maxima as a circle for each scheme and the global maxima as a triangle for the topology and threshold groups, respectively.

'ground truth' human functional connectome. To provide a reliable way of building candidate edges of the connections, we sampled the 12 schemes on graph edge filtering (Fig. 4a), which turn a fully connected matrix into a sparse graphical representation of the corresponding brain network. These schemes can be categorized into two classes: threshold-based *versus* topology-based schemes. Absolute weight thresholding (ABS_{05}), proportional thresholding ($PROP_{10}$, $PROP_{20}$), degree thresholding (DEG_5, DEG_{15}), overall efficiency cost optimization (ECO) and global cost efficiency optimization (GCE) commonly employ an threshold for filtering edges with higher strengths than a cut-off value. These schemes are widely used in network neuroscience and ignore the intrinsic topological structure of the entire brain network (e.g, leading to multiple connected components or isolated nodes). In contrast, topology-based schemes such as minimum spanning tree (MST), orthogonal MST (OMST), planar maximally filtered graph (PMFG) and triangulated maximally filtered graph (TMFG) come from other scientific disciplines and are optimized based on the entire network topology (41–44). To combine both the TMFG's efficiency and OMST's accuracy, we proposed the orthogonal TMF graph (OTMFG). All the schemes are plotted in the plane of cost *versus* global-cost efficiency (45) to better visualize the economical properties of the derived networks (Fig. 4b). These plots are fitted into the topographic (contour) maps where the local maxima

bioRxiv preprint doi: https://doi.org/10.1101/2021.05.06.442886; this version posted September 4, 2021. The copyright holder for this preprint (which was not certified by peer review) is the author/funder, who has granted bioRxiv a license to display the preprint in perpetuity. It is made available under aCC-BY-NC-ND 4.0 International license.

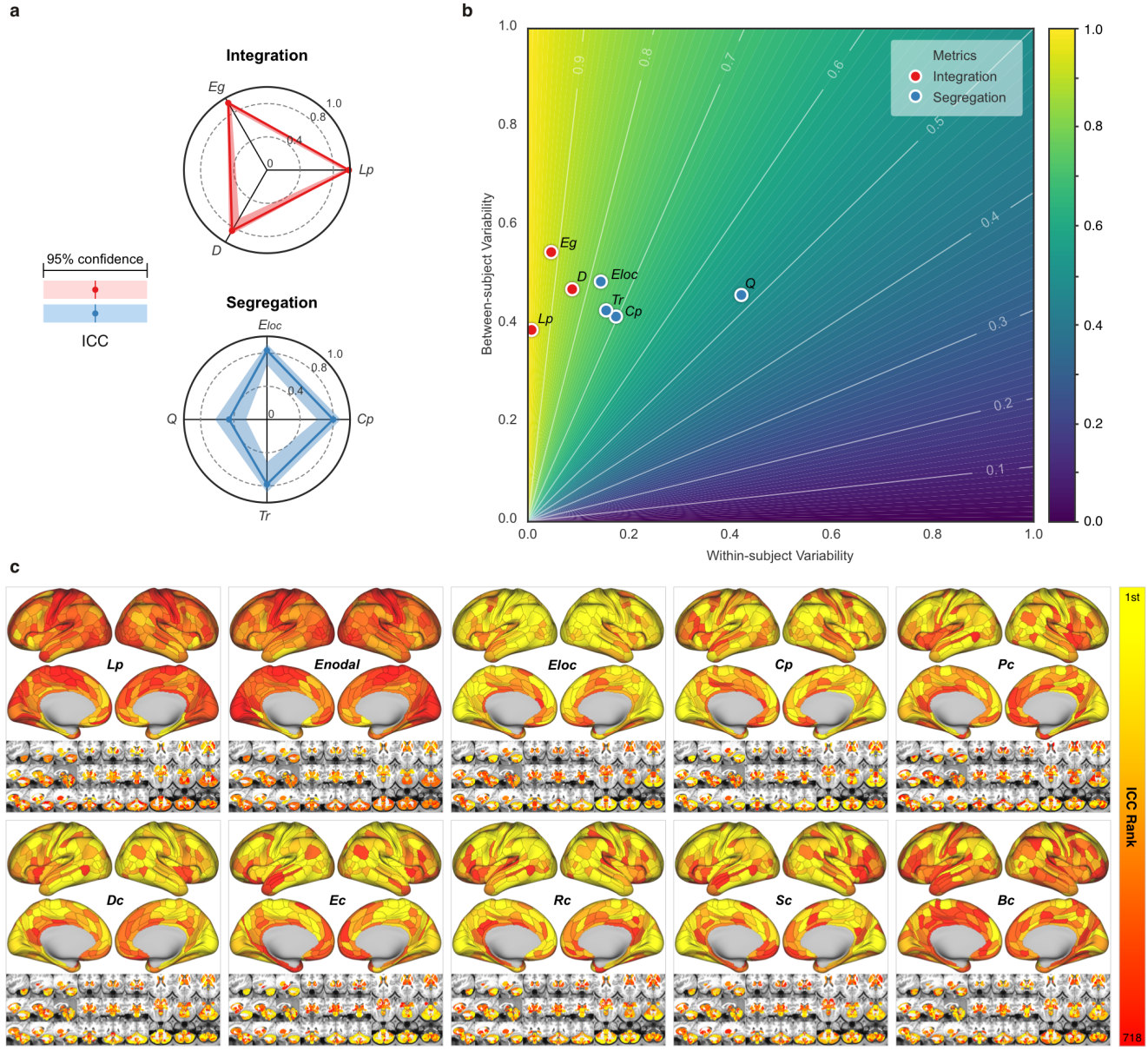

Fig. 5. Measurement reliability and variability of global/nodal network metrics under the optimized pipeline. (a) Spider plots are visualized for ICCs (test-retest) with the 95% confidence intervals (CIs, shadow bands) for the metrics of network integration, segregation, centrality and resilience. The associated symbols of the metrics can be found in supplementary material Table S31. (b) The reliability anatomy was plotted as a function of between-subject variability (V_b) and within-subject variability (V_w). (c) Ranks of ICCs across the 360 cortical parcels and the 358 subcortical parcels in the optimal pipeline (wbCABP-718, slow-2, pos, OMST) are depicted. Ten nodal metrics are assessed including average shortest path length L_p, nodal efficiency E_{nodal}, local efficiency E_{local}, clustering coefficient C_p, pagerank centrality P_c, degree centrality D_c, eigenvector centrality E_c, resolvent centrality R_c, subgraph centrality S_c and betweeness centrality B_c.

for each filtering choice is labeled as a circle. The human brain networks achieve higher global efficiency with lower cost using topology-based schemes compared to threshold-based schemes, suggesting increasingly optimal economics.

Significant differences in test-retest reliability were detectable across these 12 edge-filtering schemes ($\chi^2 = 9784.317, df = 11, p < 2.2 \times 10^{-16}, W_{\text{Kendall}} = 0.189$, see Fig. 4c). Among the topology-based schemes, OMST (mean ICC: 0.608; noap ICC: 765), OTMFG (mean ICC: 0.602; noap ICC: 781) and TMFG (mean ICC: 0.570; noap ICC: 767) were the three most reliable choices. They showed significantly greater reliability than the three most reliable threshold-based, respectively: PROP_{20} (mean ICC: 0.593; noap ICC: 632), PROP_{10} (mean ICC: 549; noap ICC: 445) and GCE (mean ICC: 0.533; noap ICC: 352). Mean reliability of MST are slight to fair (mean ICC: 0.309) but its number of almost perfect reliability (noap ICC:362) is still higher than all threshold-based schemes except PROP_{10} and PROP_{20} (see more details in Figure S21).

Network measurements are labeled based on topology and threshold groups and projected onto the reliability anatomy plane, whose axes represent between- and within-subject variability (Fig. 4d). The contour maps are reconstructed for each scheme based upon the individual variability of all the related network measurements. The topology-based methods (red) showed overall higher ICCs than the

bioRxiv preprint doi: https://doi.org/10.1101/2021.05.06.442886; this version posted September 4, 2021. The copyright holder for this preprint (which was not certified by peer review) is the author/funder, who has granted bioRxiv a license to display the preprint in perpetuity. It is made available under aCC-BY-NC-ND 4.0 International license.

threshold-based methods (blue), improvements that could be attributed to increases in between-subject variability and decreases of within-subject variability. These observations are consistent between cortex and whole brain networks while topology-based whole brain network are almost perfectly reliable (meaning almost perfect reliability, i.e., $\mathrm{ICC} \geq 0.8$).

We also explored connection transformation and edge weights, two factors included in edge filtering, the choices of connectivity transformation and weighing edges, regarding their measurement reliability. Positive (Eq.pos) (mean ICC: 0.512; noap ICC: 1,031) and exponential (Eq.exp) transformation (mean ICC: 0.509; noap ICC: 1,855) were the two most reliable choices. Comparing to the positive and absolute (Eq.abs) (mean ICC: 0.508; noap ICC: 1,050) transformation, the exponential and distance-inverse (Eq.div) (mean ICC: 0.500; noap ICC: 1,031) transformation show larger number of almost perfect ICCs (see Table S15-21). Weighted graphs are also more reliable than the binary graphs while the normalized weighted graphs demonstrated the highest ICCs, reflecting both the increased between-subject variability and decreased within-subject variability.

Network integration and segregation can serve reliable metrics of information flow. The previous big data analysis suggests that the optimally reliable pipeline should: 1) define network nodes using a whole-brain parcellation, 2) filter the time series with higher frequency bands, 3) transform the connectivity using positive transformation, 4) construct network edges using individualized methods and normalized weights. Using the optimal pipelines, we evaluated the reliability levels of various metrics from network neuroscience and their differences across individuals. Focusing on the optimized pipeline with the highest ICCs of the various choices (wbLGP-458, slow-2, pos, OMST), we reported test-retest reliability of the measurements as well as their corresponding individual variability. In Fig. 5a, we found that the global network measurements of information segregation and integration are at the level of almost perfect reliability except for the modularity Q (ICC=0.46, 95% CI = [0.252,0.625]). These high-level ICCs are derived with large between-subject variability and small within-subject variability (Fig. 5b). These findings are reproducible across the other two parcellation choices (wbCABP-718, wbBNP-458).

Similar to the global metrics, shortest path length L_p and nodal efficiency E_{nodal} exhibited the highest ICCs (almost perfect test-retest reliability) while ICCs of other nodal metrics remained less than 0.6. To visualize node-level network metrics, we reported results derived from the wbCABP-718 choice. To improve spatial contrasts of reliability, we ranked the parcels according to their ICCs and visualized the ranks in Fig. 5c. Most nodal metrics are more reliable across the 360 cortical areas than the 358 subcortical areas (Wilcoxon tests: all p-values less than 0.001, corrected for multiple comparisons). However, L_p, E_{nodal} and B_c exhibited higher across subcortical areas than cortical areas (corrected $p < 0.001$). Across the human cerebral cortex, the right hemispheric areas demonstrated more reliable C_p (corrected $p < 0.0036$) than the left hemispheric areas. Interesting patterns of the reliability gradient are also observable along large-scale anatomical directions (dorsal>ventral, posterior>anterior) across the nodal metrics of information segregation and centrality. These spatial configuration profiles on the reliability reflected their correspondence on inter-individual variability of these metrics, characterising the network information flow through the slow-2 band.

Building an open resource for reliable network neuroscience. The results presented here represent huge costs in terms of computational resources (more than 1,728,000 core-hours on **CNGrid**, supported by Chinese Academy of Sciences (http://cscgrid.cas.cn). Derivations of the ICCs and their linear mixed models were implemented in **R** and **Python**. As our practice in open science, we have started to provide an online platform on the reliability assessments (http://ibraindata.com/research/reliablenetworkneuroscience/reliabilityassessment). The big reliability data were designed into an online database for providing the community a resource to search reliable choices and help the final decision-making. The website for this online database provided more details of the reliability data use (http://ibraindata.com/research/reliablenetworkneuroscience/database). Finally, we shared all the codes, figures and other reliability resources via the website for boosting reliable FNN.

Discussions

This study examined the series of processing and analysis decisions in constructing graphical representations of brains. The focus, here, was on identifying the pipeline that generated reliable, individualized networks and network metrics. The results of our study suggest that to derive reliable global network metrics with higher inter-individual variances and lower inner-individual variances, one should use whole-brain parcellations to define network nodes, focus on higher frequencies in the slow band for time-series filtering to derive the connectivity, and use topology-based methods for edge filtering to construct sparse graphs. Regarding network metrics, multi-level or multi-modal metrics appear more reliable than single-level or single-model metrics. Derive reliable measurements is critical in network neuroscience, especially for translating network neuroscience into clinical practice, which requires precise and specific biomarkers. Based on these results, we provide four principles of reliable functional connectomics which we discuss further in this section.

Principle I: Use a whole brain parcellation to define network nodes. The basic unit of a graph is the node. However, variability across brain parcellations can yield dissimilar graphs, distorting network metrics and making it difficult to compare findings across studies(27, 46–48). In many clinical applications (14, 21), researchers aim to identify disease-specific connectivity profiles of the whole brain, including cortical and subcortical structures, as well as cerebellum. A recent review has raised the concern that many studies have

bioRxiv preprint doi: https://doi.org/10.1101/2021.05.06.442886; this version posted September 4, 2021. The copyright holder for this preprint (which was not certified by peer review) is the author/funder, who has granted bioRxiv a license to display the preprint in perpetuity. It is made available under aCC-BY-NC-ND 4.0 International license.

focused on restricted sets of nodes, e.g. cortex only, called a field standard for the best practices in clinical network neuroscience (24), which requires almost perfectly reliable measurements (15, 49). Our meta-reliability assessments revealed high reliability of measurements made involving functional brain networks can be achieved, through the inclusion of high-resolution subcortical nodes. This provides strong evidences that the whole-brain node use should be part of the standard analysis pipeline for network neuroscience applications. These improvements of reliability can be attributed to increases in between-subject variability coupled with reductions in within-subject variability relative to networks of cortical regions alone. One possible neuroanatomical explanation is that distant areas of cerebral cortex are interconnected by the basal ganglia and thalamus (50) while also communicating with different regions of the cerebellum *via* polysynaptic circuits (51, 52), forming an integrated connectome. These subcortical structures have been suggested to play a role in both primary (e.g., motor) as well as higher-order function (e.g., learning and memory (53)). Studies using rfMRI have delineated the resting-state functional connectivity (RSFC) maps between these subcortical structures and cortical networks of both primary and high-order functions (54–56). A recent work revealed that inter-individual variance in cerebellar RSFC networks exceeds that of cortex (57). Meanwhile, these RSFC maps are highly individualized and stable within individuals (58–60), indicating that they possess reliable characteristics. In line with our observations, we argue that inclusion of the subcortical structures as network nodes can enhance the between-subject variability and stabilize the within-subject variability by providing a more comprehensive measurements on the entirety of the brain connectivity. Larger between-subject variability implies that the associated measurements are more recognizable between different subjects, leading to improved subject discrimination, a finding that has been demonstrated (61, 62).

Principle II: Generate functional networks using spontaneous brain activity in multiple slow bands. It has been a common practice in RSFC research area to estimate the RSFC profile based on the low-frequency (0.01 - 0.1 Hz or 0.01 - 0.08 Hz) fMRI time series (6). However, the test-retest reliability of measurements made based on this frequency band has been limited, with ICCs less than 0.4 (see (22, 23) for systematic reviews). Other applications, however, have advocated adopting a multi-frequency perspective to examine the amplitude of brain activity at rest (63) and its network properties (64). This approach has been spurred along by recent advances in multi-banded acquisitions and fast imaging protocols, offering fMRI studies a way to examine resting-state brain activity at relatively higher frequencies that may contain neurobiologically meaningful signals (39, 65). Our study provides strong evidence of highly reliable signals across higher slow-frequency bands, which are derived with the hierarchical frequency band theory of neuronal oscillation system (35). Specifically, a spectrum of reliability increases was evident from slow bands to fast bands. This reflects greater variability of the network measurements between subjects and less measurement variability within subject between the higher and lower bands of the slow frequencies. In theory, each frequency band has an independent role in supporting brain function. Lower frequency bands are thought to support more general or global computation with long-distance connections to integrate specific or local computation, which are driven by higher slow bands based on short-distance connections (37). Our findings of high reliability (inter-individual differences) are perfectly consistent with this theory from a perspective of individual variability. Previous findings have found that high-order associative (e.g., default mode and cognitive control) networks are more reliable than the primary (e.g., somatomotor and visual) networks (16, 22, 23). Our findings offer a novel frequency-based perspective on these network-level individual differences.

Principle III: Optimize topological economy to construct network connections at individual level. There is no gold standard on for human functional connectomes, leading to plurality of approaches for inferring and constructing brain network connections. Threshold-based methods focus on the absolute strength of connectivity, retaining connections that are above some user-defined threshold and oftentimes involve applying the same threshold to all subjects. Although this approach mitigate potential biases in network metrics associated with differences in network density, it may inadvertently also lead to decreased variability between subjects. This is supported by our result finding that threshold-based method yield low reliability of network measurements. On the other hand, the human brain is a complex network that is also near-optimal in terms of connectional economy, balancing tradeoffs of cost with functionality (66). In line with this view, certain classes of topology-based methods for connection definition may hold promise for individualized network construction. Specifically, each individual brain optimizes its economic wiring in terms of cost and efficiency, reaching a trade-off between minimizing costs and allowing the emergence of adaptive topology. Our results demonstrate that such highly individualized functional connectomes generated by the topology-based methods are more reliable than those by the threshold-methods. This reflects the increases of individual differences in functional connectomes attributing to the optimal wiring economics at individual level. The topological optimization also brings other benefits such as ensuring that a graph forms a single connected component and preserving weak connections. Indeed ,there is increasing evidence supporting the hypothesis that weak connections are neurobiologically meaningful and explain individual differences in mind, behavior and demographics as well as disorders (67–69). Weak connections in a graph may be consistent across datasets and reproducible within the same individual over multiple scan sessions and therefore be reliable. Weak connections might also play non-trivial roles in transformed versions of the original brain network, e.g. so-called "edge-based functional connectivity" (70). Among these topology-based methods, MST is the simplest and promising filtering method if computational efficiency is the priority. MST can obtain a graph with the same number of nodes and edges, and

bioRxiv preprint doi: https://doi.org/10.1101/2021.05.06.442886; this version posted September 4, 2021. The copyright holder for this preprint (which was not certified by peer review) is the author/funder, who has granted bioRxiv a license to display the preprint in perpetuity. It is made available under aCC-BY-NC-ND 4.0 International license.

it is not sensitive to scaling effects, because its structure only depends on the order rather than the absolute values of the edges (71). Although MST loses some local network measurements due to the limited number of edges, it has some other unique metrics that can be calculated (e.g., leaf fraction, tree hierarchy). A better alternative might be TMFG which computationally very efficient and statistically robust, while the OMST and OTMFG are the most reliable choices given priority to large individual differences.

Principle IV: Characterise information flow with network integration and segregation metrics. Functional connectomes reflect the outcome of communication processes and information flows between pairs of brain regions. How information and other signals propagate between pairs of brain regions can be assayed using network neuroscientific metrics and is essential to understanding normative connectome function and its variation in clinical settings (72). While the ground truth functional connectome is unknown (and may not exist (73)), network models can help validate the imaging-based reconstructions of human functional connectomes (1). From a perspective of individual differences, reliable FNN is the basis of achieving valid measurements of the individual differences in FNN metrics (16). Our findings indicated that both the brain network segregation and integration could be reliably measured with functional connectomics using rfMRI by the optimized pipelines. At the global level, measures of information integration, e.g. characteristic path length and efficiency, were more reliable than those of information segregation, e.g. modularity and clustering coefficient. Our results also revealed that measures of integration were more stable across different scan sessions (i.e., the test-retest) for an individual subject than the segregation measurements while the inter-individual variability are measured at the similar level for both integration and segregation metrics. At nodal level, mapping reliability of the network measurements revealed interesting spatial patterns. Specifically, we found that cortical areas were generally associated with more reliable local measurements compared to subcortical areas. This may reflect different functional roles for human cortex and subcortex. For example, the differences in reliability of path-based metrics might reflect the fact that there are more within-community paths in cortex while between-community paths are more common in subcortex. Beyond this cortical-subcortical gradient, reliability of the nodal information flow also fit the left-right asymmetry and dorsal-ventral as well as posterior-anterior gradient, implying the potential validity of individual differences in information flow attributing to evolutionary, genetic and anatomical factors (74–77). To facilitate the utility of reliable network integration and segregation metrics in FNN, we integrated all the reliability resources into an online platform for reliability queries on specific metrics of information flow (`http://ibraindata.com/research/reliablenetworkneuroscience`).

Conclusion, limitations and future. Here, we adopt a big data approach to systematically explore the reliability of functional brain networks by richly sampling the parameters of various steps in the network construction and analysis pipeline. The results of this analysis provided robust experimental evidence supporting four key principles that will support reliable network neuroscience measurements and applications. These principles can serve as the base for building guidelines on the use of FNN to map individual differences. Standard guidelines are essential for improvements of reproducibility in the research practice, and our findings provide experimental resources for such standardization in future network neuroscience applications. We note, however, that while our approach was extensive, it was not exhaustive – the analytical sampling procedure could miss many other existing choices (e.g., consensus-based thresholding for the edge filtering stage). The processing decisions that yield reliable connectomes may yield the most reliable network statistics, but there may be another way to process data that yields overall a higher level of reliability in network measures. Future work can build on our study by exploring these and other choices using the online computation and evaluation platform that accompanies the present study. Of note, the measurement reliability is not the final goal but the validity, which must be considered although not easily ready for a direct examination (16). Validation (through various indirect validity assessments) on the use of the proposed principles represents a promising arena for future FNN studies (5).

Online Methods

Using the HCP test-retest dataset, our analytic procedure implemented four post-processing stages (Fig. 1a): node definition, edge construction, network measurement and reliability assessments. Specifically, the test-retest rfMRI dataset underwent the standardized preprocessing pipeline developed by the HCP team (34). The second step defines nodes (green box) using sets of brain areas based on 24 partitions, and then extracts the nodal time series. During the third step (yellow box), individual correlation matrices are first estimated based upon the six frequency bands derived from Buzsáki's theoretical framework on brain oscillations (35) along with the classical band widely used (0.01 - 0.08 Hz). These matrices are then converted into adjacency matrices using $4 \times 12 = 48$ strategies on edge filtering. In the fourth step, we performed graph analyses (blue box) by systematically calculating the brain graph metrics at global, modular and nodal scales. Finally, test-retest reliability was evaluated (red box) as ICCs with the linear mixed models.

Test-Retest Dataset. The WU-Minn Consortium in HCP shared a set of test-retest multimodal MRI datasets of 46 subjects from both the S1200 release and the Retest release. These subjects were retested using the full HCP 3T multimodal imaging and behavioral protocol. Each subject underwent the four scans on two days (two scans per day: Rest1 versus Rest2) during the first visit and returned several months later to finish the four scans on another two days during the second visit (Fig. 1b). The test-retest interval ranged from 18 to 328 days (mean: 4.74 months, standard

bioRxiv preprint doi: https://doi.org/10.1101/2021.05.06.442886; this version posted September 4, 2021. The copyright holder for this preprint (which was not certified by peer review) is the author/funder, who has granted bioRxiv a license to display the preprint in perpetuity. It is made available under aCC-BY-NC-ND 4.0 International license.

deviation: 2.12 months). Only 41 subjects (28 females, age range: 26-35 years; 13 males, age range: 22-33 years) had full length rfMRI data across all the eight scans, and were included in the subsequent analyses. As indicated in the literature (22, 34), rfMRI protocols used by HCP for scanning and preprocessing images have been optimized for reliability.

During the scanning, participants were instructed to keep their eyes open and to let their mind wander while fixating on a cross-hair projected on a dark background. Data were collected on the 3T Siemens Connectome Skyra MRI scanner with a 32-channel head coil. All functional images were acquired using a multiband gradient-echo EPI imaging sequence (2mm isotropic voxel, 72 axial slices, TR = 720ms, TE = 33.1ms, flip angle = 52°, field of view = 208×180 mm^2, matrix size = 104×90 and a multiband factor of 8). A total of 1200 images was acquired for a duration of 14 min and 24 s. Details on the imaging protocols can be found in (78).

The protocols of rfMRI image preprocessing and artifact-removal procedures are documented in detail elsewhere and generated the minimally preprocessed HCP rfMRI images. It is note that artifacts were removed using the Oxford Center for Functional MRI of the Brain's ICA-based X-noiseifier (ICA + FIX) procedure, followed by MS-MAll for inter-subject registration. The preprocessed rfMRI data were represented as a time series of grayordinates (4D), combining both cortical surface vertices and subcortical voxels (34).

Node Definition. A brain graph defines a node as a brain area, which is generally derived by an element of brain parcellation (parcel) according to borders or landmarks of brain anatomy, structure or function as well as an element of volume (voxel) in imaging signal acquisition or a cluster of voxels (79). Due to the high computational demand of voxel-based brain graph, in this study we defined nodes as parcels according to the following brain parcellation strategies (Fig. 2a). A surface-based approach has been demonstrated to outperform other approaches for fMRI analysis (26, 80) and thus the nodes are defined in the surface space (total 30 surface parcellation choices). We adopted a naming convention for brain parcellations as follows: '*ParcAbbr-NumberOfParcels*' (e.g., LGP-100 or its whole-brain version wbLGP-458).

HCP Multi-Modal Parcellation (MMP) A cortical parcellation generated from multi-modal images of 210 adults from the HCP database, using a semi-automated approach (81). Cortical regions are delineated with respect to their function, connectivity, cortical architecture, and topography, as well as, expert knowledge and meta-analysis results from the literature (81). The atlas contains 180 parcels for each hemisphere.

Local-Global Parcellation (LGP) A gradient-weighted Markov Random Field model integrating local gradient and global similarity approaches produces the novel parcellations (82). The final version of LGP comes with a multi-scale cortical atlas including 100, 200, 300, 400, 500, 600, 700, 800, 900, and 1000 parcels (equal numbers across the two hemispheres). One benefit of using LGP is to have nodes with almost the same size, and these nodes are also assigned to the common large-scale functional networks (40).

Brainnetome Parcellation (BNP) Both anatomical landmarks and connectivity-driven information are employed to develop this volumetric brain parcellation (83). Specifically, anatomical regions defined as in (84) are parcellated into subregions using functional and structural connectivity fingerprints from HCP datasets. Cortical parcels are obtained by projecting their volume space to surface space. It is noticed that the original BNP contains both cortical (105 areas per hemisphere) and subcortical (36 areas) regions but only the 210 cortical parcels are included for the subsequent analyses.

Whole-Brain Parcellation (wb) Inclusion of subcortical areas has been shown unignorable influences on brain graph analyses (23, 60), and we thus also constructed brain graphs with subcortical structures in volume space as nodes by adding these nodes to the cortical brain graphs. To get a high-resolution subcortical parcellation, we adopted the 358 subcortical parcels in (85). The authors employed data of 337 unrelated HCP healthy volunteers and extended the MMP cortical network partition into subcortex. This results a set of whole-brain parcellations by combining these subcortical parcels with the aforementioned cortical parcellations, namely **wbMMP**,**wbLGP** and **wbBNP**. We noticed that the wbMMP-718 has been named by the authors of (85) as the Cole-Anticevic Brain-wide Network Partition, and we thus renamed the wbMMP-718 as wbCABP-718 for consistency.

Edge Construction. After defining the node with each parcellation, in each parcel, regional mean time series were estimated by averaging the vertex time series at each time point. To construct an edge between a pair of nodes, their representative time series entered into the following steps in order: *band-pass filtering*, *inter-node connectivity transformation*, and *edge filtering*.

Band-Pass Filtering. Resting-state functional connectivity studies have typically focused on fluctuations below 0.08 Hz or 0.1 Hz (6, 86), and assumed that only these frequencies contribute significantly to inter-regional functional connectivity (FC) while other frequencies are artifacts (87). In contrast, however, other studies have found that specific frequency bands of the rfMRI oscillations make unique and neurobiologically meaningful contributions to resting-state functional connectivity (22, 88). More recently, with fast fMRI methods, some meaningful FC patterns were reported across much higher frequency bands (89). These observations motivate exploring a range of frequency bands beyond those typically studied in resting-state functional connectivity studies, including faster frequencies.

Buzsáki and Draguhn (35) proposed a hierarchical organization of frequency bands driven by the natural logarithm

bioRxiv preprint doi: https://doi.org/10.1101/2021.05.06.442886; this version posted September 4, 2021. The copyright holder for this preprint (which was not certified by peer review) is the author/funder, who has granted bioRxiv a license to display the preprint in perpetuity. It is made available under aCC-BY-NC-ND 4.0 International license.

linear law. This offers a theoretical template for partitioning rfMRI frequency content into multiple bands (Fig. 3a). The frequencies occupied by these bands have a relatively constant relationship to each other on a natural logarithmic scale and have a constant ratio between any given pair of neighboring frequencies (37). These different oscillations are linked to different neural activities, including cognition, emotion regulation, and memory (37, 64, 86). Advanced by the fast imaging protocols offered by the HCP scanner, the short scan interval (TR = 720ms) allows us to obtain more oscillation classes that the traditional rfMRI method. We incorporate the Buzsáki's framework (35, 38) with the HCP fast-TR datasets by using the DREAM toolbox (39) in the Connectome Computation System (29). It decomposed the time series into the six slow bands as illustrated in Fig. 3a.

Connectivity Transformation. For each scan, individual nodal representative time series were band-pass filtered with each of the six frequency bands, and another empirical frequency band, slow-emp (0.01-0.08Hz). The Pearson's correlation $r_{ij} \in [-1,1]$ between the filtered time series of each pair of nodes $i = 1,...,N, j = 1,...,N$ was calculated (N is the number of nodes). These correlation values provided an estimation on the edge strengths between the two nodes, and formed a $N \times N$ symmetric correlation matrix $R = (r_{ij})$ for each given subject, scan, parcellation, and frequency band.

Many network metrics are not well defined for negatively weighted connections. In order to ensure that the connection weights are positive only, we applied four types of transformations to the symmetric correlation matrix: the **positive** (Eq.pos), **absolute** (Eq.abs), **exponential** (Eq.exp) and **distance-inverse** (Eq.div) functions, respectively. This avoids the negative values in the inter-node connectivity matrix $W = (w_{ij})$ where $z_{ij} = \tanh^{-1}(r_{ij})$ is Fisher's $z-$transformation.

$$w_{ij} = \frac{z_{ij} + |z_{ij}|}{2} \in [0, \infty) \qquad \textbf{(pos)}$$

$$w_{ij} = |z_{ij}| \in [0, \infty) \qquad \textbf{(abs)}$$

$$w_{ij} = \mathbf{e}^{z_{ij}} \in [0, \infty) \qquad \textbf{(exp)}$$

$$w_{ij} = \frac{2}{\sqrt{2 \times (1 - r_{ij})}} \in (0, \infty) \qquad \textbf{(div)}$$

The connectivity matrix represents a set of the node parcels and relational quantities between each pair of the nodes, and will serve as the basis of following edge filtering procedure for generation of the final brain graphs.

Edge Filtering. In a graph, edges represent a set of relevant interactions of crucial importance to obtain parsimonious descriptions of complex networks. Filtering valid edges can be highly challenging due to the lack of 'ground truth' of the human brain connectome. To provide a reliable way of building candidate edges, we sampled the following 12 schemes on edge filtering and applied them to the connectivity matrices.

Absolute Weight Thresholding (ABS) This approach selects those edges that exceed a manually defined absolute threshold (e.g., correlations higher than 0.5), setting all correlations smaller than 0.5 to 0 (ABS_{05}). This is a simple approach to reconstruct networks (90).

Proportional Thresholding (PROP) It is a common step in the reconstruction of functional brain networks to ensure equal edge density across subjects (91–93). It keeps the number of connections fixed across all individuals to rule out the influence of network density on the computation and comparison of graph metrics across groups. This approach includes the selection of a fixed percentage of the strongest conncections as edges in each individual network or brain graph. Compared to ABS, PROP has been argued to reliably separate density from topological effects (30, 94) and to result in more stable network metrics (95). This makes it a commonly used approach for network construction and analysis in disease-related studies. Here, we focused on two threshholds that are commonly reported in the literature: 10% (PROP_{10}) and 20% (PROP_{20}).

Degree Thresholding (DEG) The structure of a graph can be biased by the number of existing edges. Accordingly, statistical measures derived from the graph should be compared against graphs that preserve the same average degree, K. A threshold of the degree can be chosen to produce graphs with a fixed mean degree (e.g., $K = 5$, DEG_5), which is the average nodal degrees of an individual graph from a single subject's scan. Many network neuroscience studies have taken this choice for $K = 5$ (96–99). We also include the DEG_{15} for denser graphs of the brain networks.

Global Cost Efficiency Optimization (GCE) Given a network with a cost ρ, its global efficiency is a function of the cost $E_g(\rho)$, and its GCE is $J(\rho) = E_g(\rho) - \rho$. Several studies suggested that brain networks, in particular those with small-world topology, maximize their global-cost efficiency (45), i.e., $J^{max} = \max_\rho J(\rho)$. Computationally, this scheme is implemented by looping all network costs (e.g., adding edges with weights in order) to find the J^{max} (see Fig. 2b) where the corresponding edge weight was determined as the threshold for edge filtering. In this sense, GCE is an individualised and optimised version of ABS, PROP and DEG while the latter three are commonly employed with a fixed threshold for all individuals.

Overall Efficiency Cost Optimization (ECO) Both global and local efficiency are important graph features to characterize the structure of complex systems in terms of integration and segregation of information (100). ECO was proposed to determine a network density threshold for filtering out the weakest links (101). It maximizes an extension of J^{max}, the ratio between the overall (both global and local) efficiency and its wiring cost $\max_\rho J^{ext}(\rho) = (E_g(\rho) + E_{loc}(\rho))/\rho$ where E_{loc}

bioRxiv preprint doi: https://doi.org/10.1101/2021.05.06.442886; this version posted September 4, 2021. The copyright holder for this preprint (which was not certified by peer review) is the author/funder, who has granted bioRxiv a license to display the preprint in perpetuity. It is made available under aCC-BY-NC-ND 4.0 International license.

denotes the network local efficiency. The study (100) also demonstrated that, to maximize J, these networks have to be sparse with an average node degree $K \simeq 3$.

Minimum Spanning Tree (MST) This is an increasingly popular method for identifying the smallest and most essential set of connections while ensuring that the network forms a fully connected graph (102–105). The tenet of using MST is to summarize information and index structure of the graph, and thus remove edges with redundant information (41). Specifically, an MST filtered graph will contain N nodes connected *via* $N-1$ connections with minimal cost and no loops. This addresses key issues in existing topology filtering schemes that rely on arbitrary and user-specified absolute thresholds or densities.

Orthogonal Minimum Spanning Tree (OMST) This topological filtering scheme was proposed recently (42) to maximize the information flow over the network *versus* the cost by selecting the connections via the OMSTs. It samples the full-weighted brain network over consecutive rounds of MST that are orthogonal to each other (see Fig. 2b). Practically, we extracted the 1st MST, and then we cleared their connections and we tracked the 2nd MST from the rest of the network connections, etc. Such an iterative procedure (stopped by the Mth MST) can get orthogonal MSTs and topologically filter brain network by optimizing the GCE under the constrains by the MST, leading to an integration of both GCE and MST

$$\max_{n\in[1,M]} J(\rho(n\text{MSTs})) = E_g(\rho(n\text{MSTs})) - \rho(n\text{MSTs})$$

Planar Maximally Filtered Graph (PMFG) The idea underneath PMFG (43) is to filter a dense matrix of weights by retaining the largest possible subgraph while imposing global constraints on the topology of the resulting network. In particular, edges with the strong connection weights are retained while constraining the subgraph to be a (spanning) tree globally. Similarly, during the PMFG construction, the largest weights are retained while constraining the subgraph to be a planar graph globally. The PMFG algorithm searches for the maximum weighted planar subgraph by adding edges one by one. The resulting matrix is sparse, with $3(N-2)$ edges. It starts by sorting all the edges of a dense matrix of weights in non-increasing order and tries to insert every edge in the PMFG. Edges that violate the planarity constraint are discarded.

Triangulated Maximally Filtered Graph (TMFG) The algorithm for implementing PMFG is computationally expensive, and is therefore impractical when applied to large brain networks (44). A more efficient algorithms, TMFG, was developed that exhibited greatly reduced computational complexity compared to PMFG. This method captures the most relevant information between nodes by approximating the network connectivity matrix with the endorsement association matrix and minimizing spurious associations. The TMFG derived network contains 3-node (triangle) and 4-node (tetrahedron) cliques, imposing a nested hierarchy and automatically generates a chordal network (44, 106). Although TMFG is not widely applied in network neuroscience studies, it as been applied elsewhere and proven to be a suitable choice for modeling interrelationships between psychological constructs like personality traits (107).

Orthogonal TMF Graph (OTMFG) To combine both the TMFG's efficiency and OMST's accuracy, we propose OTMFG to maximize the information flow over the network *versus* the cost by selecting the connections of the orthogonal TMFG. It samples the full-weighted brain network over consecutive rounds of TMFG that are orthogonal to each other.

In summary, as illustrated in Fig. 4a, the 12 edge filtering schemes transform a fully weighted matrix into a sparse matrix to represent the corresponding brain network. They can be categorized into two classes: threshold-based *versus* topology-based schemes. ABS_{05}, PROP_{10}, PROP_{20}, DEG_5, DEG_{15}, ECO and GCE rely on a threshold for filtering and retaining edges with higher weights than the threshold. These schemes normally ignore the topological structure of the entire network and can result in isolated nodes. In contrast, the topology-based methods including MST, OMST, PMFG, TMFG and OTMFG, all consider the global network topology in determining which edges to retain. As illustrated in Fig. 4b, all the schemes are plotted in the $\rho - J^{max}$ plane for their network economics.

Network Analysis. We performed graph-theory-driven network analysis by calculating several common graph-based metrics for the resulting graphs. These measures, broadly, can be interpreted based on whether the characterize the extent to which network structure allows for integrated or segregation information flow. Examples of integrative measures include average shortest path length (L_p), global efficiency (E_g), and pseudo diameter (D). Segregation measures include clustering coefficient (C_p), local efficiency (E_{local}), transitivity (Tr), modularity (Q), and a suite of nodal centrality measures (Appendix 1). All the metrics are calculated using functions included in the Brain Connectivity Toolbox (108). We employed **graph-tool** (`https://graph-tool.skewed.de`) and **NetworKit** (`https://networkit.github.io`) to achieve high performance comparable (both in memory usage and computation time) to that of a pure C/C++ library. We treated these metrics as the network measurements for subsequent reliability analysis.

Reliability Assessments. Measurement reliability is defined as the extent to which measurements can be replicated across multiple repeated measures. Test-retest reliability is the closeness of the agreement between the results of succes-

bioRxiv preprint doi: https://doi.org/10.1101/2021.05.06.442886; this version posted September 4, 2021. The copyright holder for this preprint (which was not certified by peer review) is the author/funder, who has granted bioRxiv a license to display the preprint in perpetuity. It is made available under aCC-BY-NC-ND 4.0 International license.

sive measurements of the same measure and carried out under the same conditions of measurement.

Linear mixed models. As a group-level statistic, reliability refers to the inter-individual or between-subject variability V_b relative to the intra-individual or within-subject variability V_w. Both the intra- and inter-individual variances can be estimated using linear mixed model (LMM). In this study, given a functional graph metric ϕ, we considered a random sample of P subjects with N repeated measurements of a continuous variable in M visits. ϕ_{ijk} (for $i = 1, \cdots, N$ and $j = 1, \cdots, M$, and $k = 1, \cdots, P$) denotes the metric from the kth subject's j^{th} visit and i^{th} measurement occasions. The three-level LMM models ϕ_{ijk} as the following equations:

$$\overbrace{\phi_{ijk}}^{\text{Graph metric}} = \underbrace{\gamma_{000}}_{\substack{\text{fixed}\\\text{intercept}}} + \underbrace{p_{0k}}_{\substack{\text{random intercepts}\\\text{level 3, subjects}}} + \underbrace{v_{0jk}}_{\substack{\text{random intercepts}\\\text{level 2, visits}}} + \underbrace{e_{ijk}}_{\substack{\text{random}\\\text{residuals}}}$$

Where γ_{000} is a fixed parameter (the group mean) and p_{0k}, v_{0jk} and e_{ijk} are independent random effects normally distributed with a mean of 0 and variances σ^2_{p0}, σ^2_{v0}, and σ^2_e. The term p_{0k} is the subject effect, v_{0jk} is the visit effect and e_{ijk} is the measurement residual. Age, gender and interval(Δt) between two visits are covariants.

ICC Estimation. These variances are used to calculate the test-retest reliability, which is measured by the dependability coefficient and reflects the absolute agreement of measurements. The dependability coefficient is a form of the intraclass correlation coefficient (ICC) commonly, which is the ratio of the variances due to the object of measurement versus sources of error. To avoid negative ICC values and obtain more accurate estimation of the sample ICC, the variance components in model are usually estimated with the restricted maximum likelihood (ReML) approach with the covariance structure of an unrestricted symmetrical matrix (26).

$$\text{Reliability}(\phi) = \frac{V_b}{V_b + V_w} = \frac{\sigma^2_{p0}}{\sigma^2_{p0} + \sigma^2_e} \qquad \textbf{(ICC)}$$

A metric with moderate to almost perfect test-retest reliability (ICC ≥ 0.4) is commonly expected in practice. The level of reliability should not be judged only based upon the point statistical estimation of ICC but its confidence intervals (CI) (109). We employed the nonparametric conditional bootstrap method for 1000 times to estimate their 95% CIs.

Statistics Evaluation. Our analyses can produce big data of reliability statistics including 419,328 ICCs for the global network metrics. These ICCs are grouped into four categories (parcellation, frequency band, connectivity transformation and edge filtering scheme), each of which has different choices. Given each choice of a category, we estimated its density distributions of ICCs and calculated two descriptive statistics: 1) mean ICC values, which measures the *general reliability* under the given choice; 2) number of almost perfect (noap) ICC values, which measures the *potential reliability* under the given choice.

We further perform Friedman rank sum test to evaluate whether the location parameters of the distribution of ICCs are the same in each choice. Once the Friedman test is significant, we employ the pairwise Wilcoxon signed rank test for post-hoc evaluations to compare ICCs between each pair of the distributions under different choices. The statistical significance levels are corrected with Bonferroni method for controlling the family wise error rate at a level of 0.05. We develop a method to visualize and evaluate the change of ICCs (i.e., reliability gradient) between different choices (Fig. 1c). Specifically, the reliability can be plotted as a function of V_b and V_w in its anatomy plane (15, 16). The gradient of reliability between two choices is modeled by the vector (i.e., the black arrow), and decomposed into changes of individual variability. The systematic evaluation on the reliability of the global network metrics determines the optimal network neuroscience by combining the most reliable pipeline choices. Finally, the optimized pipeline generates the nodal metrics as well as their reliability.

ACKNOWLEDGEMENTS

This work was supported in part by the Startup Funds for Leading Talents at Beijing Normal University, the National Basic Science Data Center 'Chinese Data-sharing Warehouse for In-vivo Imaging Brain' (NBSDC-DB-15), Beijing Municipal Science and Technology Commission (Z161100002616023, Z181100001518003), the Key-Area Research and Development Program of Guangdong Province (2019B030335001), Guangxi BaGui Scholarship (201621), and Indiana University Office of the Vice President for Research Emerging Area of Research Initiative, Learning: Brains, Machines and Children. The neuroimaging data were provided by the HCP WU-Minn Consortium, which is funded by the 16 NIH institutes and centers that support the NIH Blueprint for Neuroscience Research 1U54MH091657 (PIs: David Van Essen and Kamil Ugurbil), the McDonnell Center for Systems Neuroscience at Washington University.

bioRxiv preprint doi: https://doi.org/10.1101/2021.05.06.442886; this version posted September 4, 2021. The copyright holder for this preprint (which was not certified by peer review) is the author/funder, who has granted bioRxiv a license to display the preprint in perpetuity. It is made available under aCC-BY-NC-ND 4.0 International license.

Bibliography

1. D.S. Bassett, K.E. Cullen, S.B. Eickhoff, M.J. Farah, Y. Goda, P. Haggard, H. Hu, Y.L. Hurd, S.A. Josselyn, B.S. Khakh, J.A. Knoblich, P. Poirazi, R.A. Poldrack, M. Prinz, P.R. Roelfsema, T.L. Spires-Jones, M. Sur, and H.R. Ueda. Reflections on the past two decades of neuroscience. *Nature Reviews Neuroscience*, 21(10):524–534, 2020.
2. O. Sporns. Making sense of brain network data. *Nature Methods*, 10(6):491–493, 2013.
3. R.C. Craddock, S. Jbabdi, C.-G. Yan, J.T. Vogelstein, F.X. Castellanos, A. Di Martino, C. Kelly, K. Heberlein, S. Colcombe, and M.P. Milham. Imaging human connectomes at the macroscale. *Nature Methods*, 10(6):524–539, 2013.
4. D.S. Bassett and O. Sporns. Network neuroscience. *Nature Neuroscience*, 20(3):353–364, 2017.
5. D.S. Bassett, P. Zurn, and J.I. Gold. On the nature and use of models in network neuroscience. *Nature Reviews Neuroscience*, 19(9):566–578, 2018.
6. B. Biswal, F. Zerrin Yetkin, V.M. Haughton, and J.S. Hyde. Functional connectivity in the motor cortex of resting human brain using echo-planar MRI. *Magnetic Resonance in Medicine*, 34(4):537–541, 1995.
7. B.B. Biswal, M. Mennes, X.-N. Zuo, S. Gohel, C. Kelly, S.M. Smith, C.F. Beckmann, J.S. Adelstein, R.L. Buckner, S. Colcombe, A.-M. Dogonowski, M. Ernst, D. Fair, M. Hampson, M.J. Hoptman, J.S. Hyde, V.J. Kiviniemi, R. Kötter, S.-J. Li, C.-P. Lin, M.J. Lowe, C. Mackay, D.J. Madden, K.H. Madsen, D.S. Margulies, H.S. Mayberg, K. McMahon, C.S. Monk, S.H. Mostofsky, B.J. Nagel, J.J. Pekar, S.J. Peltier, S.E. Petersen, V. Riedl, S.A.R.B. Rombouts, B. Rypma, B.L. Schlaggar, S. Schmidt, R.D. Seidler, G.J. Siegle, C. Sorg, G.-J. Teng, J. Veijola, A. Villringer, M. Walter, L. Wang, X.-C. Weng, S. Whitfield-Gabrieli, P. Williamson, C. Windischberger, Y.-F. Zang, H.-Y. Zhang, F.X. Castellanos, and M.P. Milham. Toward discovery science of human brain function. *Proceedings of the National Academy of Sciences of the United States of America*, 107(10):4734–4739, 2010.
8. C. Kelly, B.B. Biswal, R.C. Craddock, F.X. Castellanos, and M.P. Milham. Characterizing variation in the functional connectome: Promise and pitfalls. *Trends in Cognitive Sciences*, 16(3):181–188, 2012.
9. S.M. Smith, D. Vidaurre, C.F. Beckmann, M.F. Glasser, M. Jenkinson, K.L. Miller, T.E. Nichols, E.C. Robinson, G. Salimi-Khorshidi, M.W. Woolrich, D.M. Barch, K. Uğurbil, and D.C. Van Essen. Functional connectomics from resting-state fMRI. *Trends in Cognitive Sciences*, 17(12):666–682, 2013.
10. K.R.A. Van Dijk, T. Hedden, A. Venkataraman, K.C. Evans, S.W. Lazar, and R.L. Buckner. Intrinsic functional connectivity as a tool for human connectomics: Theory, properties, and optimization. *Journal of Neurophysiology*, 103(1):297–321, 2010.
11. J. Dubois and R. Adolphs. Building a science of individual differences from fMRI. *Trends in Cognitive Sciences*, 20(6):425–443, 2016.
12. X.-N. Zuo, Y. He, R.F. Betzel, S. Colcombe, O. Sporns, and M.P. Milham. Human connectomics across the life span. *Trends in Cognitive Sciences*, 21(1):32–45, 2017.
13. L. Pessoa. Understanding emotion with brain networks. *Current Opinion in Behavioral Sciences*, 19:19–25, 2018.
14. A. Fornito, A. Zalesky, and M. Breakspear. The connectomics of brain disorders. *Nature Reviews Neuroscience*, 16(3):159–172, 2015.
15. X.-X. Xing and X.-N. Zuo. The anatomy of reliability: a must read for future human brain mapping. *Science Bulletin*, 63(24):1606–1607, 2018.
16. X.-N. Zuo, T. Xu, and M.P. Milham. Harnessing reliability for neuroscience research. *Nature Human Behaviour*, 3(8):768–771, 2019.
17. M.P. Milham, J. Vogelstein, and T. Xu. Removing the reliability bottleneck in functional magnetic resonance imaging research to achieve clinical utility. *JAMA Psychiatry*, 78(6): 587–588, 2021.
18. M.L. Elliott, A.R. Knodt, A. Caspi, T.E. Moffitt, and A.R. Hariri. Need for psychometric theory in neuroscience research and training: Reply to kragel et al. (2021). *Psychological Science*, 32(4):627–629, 2021.
19. H.C. Kraemer. The reliability of clinical diagnoses: State of the art. *Annual Review of Clinical Psychology*, 10:111–130, 2014.
20. M. Herting, P. Gautam, Z. Chen, A. Mezher, and N.C. Vetter. Test-retest reliability of longitudinal task-based fmri: Implications for developmental studies. *Developmental Cognitive Neuroscience*, 33:17–26, 2018.
21. P.M. Matthews and A. Hampshire. Clinical concepts emerging from fMRI functional connectomics. *Neuron*, 91(3):511–528, 2016.
22. X.-N. Zuo and X.-X. Xing. Test-retest reliabilities of resting-state FMRI measurements in human brain functional connectomics: A systems neuroscience perspective. *Neuroscience and Biobehavioral Reviews*, 45:100–118, 2014.
23. S. Noble, D. Scheinost, and R.T. Constable. A decade of test-retest reliability of functional connectivity: A systematic review and meta-analysis. *NeuroImage*, 203:116157, 2019.
24. Michael N. Hallquist and Frank G. Hillary. Graph theory approaches to functional network organization in brain disorders: A critique for a brave new small-world. *Network Neuroscience*, 3(1):1–26, 2019.
25. M.L. Elliott, A.R. Knodt, and A.R. Hariri. Striving toward translation: strategies for reliable fmri measurement. *Trends in Cognitive Sciences*, 25(9):776–787, 2021.
26. X.-N. Zuo, T. Xu, L. Jiang, Z. Yang, X.-Y. Cao, Y. He, Y.-F. Zang, F.X. Castellanos, and M.P. Milham. Toward reliable characterization of functional homogeneity in the human brain: Preprocessing, scan duration, imaging resolution and computational space. *NeuroImage*, 65:374–386, 2013.
27. J. Wang, L. Wang, Y. Zang, H. Yang, H. Tang, Q. Gong, Z. Chen, C. Zhu, and Y. He. Parcellation-dependent small-world brain functional networks: A resting-state fMRI study. *Human Brain Mapping*, 30(5):1511–1523, 2009.
28. X. Liang, J. Wang, C. Yan, N. Shu, K. Xu, G. Gong, and Y. He. Effects of different correlation metrics and preprocessing factors on small-world brain functional networks: A resting-state functional MRI study. *PLoS One*, 7(3):e32766, 2012.
29. T. Xu, Z. Yang, L. Jiang, X.-X. Xing, and X.-N. Zuo. A Connectome Computation System for discovery science of brain. *Science Bulletin*, 60(1):86–95, 2015.
30. U. Braun, M.M. Plichta, C. Esslinger, C. Sauer, L. Haddad, O. Grimm, D. Mier, S. Mohnke, A. Heinz, S. Erk, H. Walter, N. Seiferth, P. Kirsch, and A. Meyer-Lindenberg. Test-retest reliability of resting-state connectivity network characteristics using fMRI and graph theoretical measures. *NeuroImage*, 59(2):1404–1412, 2012.
31. M. Termenon, A. Jaillard, C. Delon-Martin, and S. Achard. Reliability of graph analysis of resting state fMRI using test-retest dataset from the Human Connectome Project. *NeuroImage*, 142:172–187, 2016.
32. N.K. Aurich, J.O.A. Filho, A.M.M. da Silva, and A.R. Franco. Evaluating the reliability of different preprocessing steps to estimate graph theoretical measures in resting state fMRI data. *Frontiers in Neuroscience*, 9:48, 2015.
33. D.C. Van Essen, S.M. Smith, D.M. Barch, T.E.J. Behrens, E. Yacoub, and K. Ugurbil. The WU-Minn Human Connectome Project: An overview. *NeuroImage*, 80:62–79, 2013.
34. M.F. Glasser, S.N. Sotiropoulos, J.A. Wilson, T.S. Coalson, B. Fischl, J.L. Andersson, J. Xu, S. Jbabdi, M. Webster, J.R. Polimeni, D.C. Van Essen, and M. Jenkinson. The minimal preprocessing pipelines for the Human Connectome Project. *NeuroImage*, 80:105–124, 2013.
35. G. Buzsaki and A. Draguhn. Neuronal oscillations in cortical networks. *Science*, 304 (5679):1926–1929, 2004.
36. J.R. Landis and G.G. Koch. The measurement of observer agreement for categorical data. *Biometrics*, 33(1):159–174, 1977.
37. G. Buzsáki. *Rhythms of the Brain.* Oxford University Press, 2009.
38. M. Penttonen and G. Buzsáki. Natural logarithmic relationship between brain oscillators. *Thalamus and Related Systems*, 2(2):145–152, 2003.
39. Z.-Q. Gong, P. Gao, C. Jiang, X.-X. Xing, H.-M. Dong, T. White, F.X. Castellanos, H.-F. Li, and X.-N. Zuo. DREAM: A toolbox to decode rhythms of the brain system. *Neuroinformatics*, 19(3):529–545, 2021.
40. B.T. Thomas Yeo, F.M. Krienen, J. Sepulcre, M.R. Sabuncu, D. Lashkari, M. Hollinshead, J.L. Roffman, J.W. Smoller, L. Zöllei, J.R. Polimeni, B. Fisch, H. Liu, and R.L. Buckner. The organization of the human cerebral cortex estimated by intrinsic functional connectivity. *Journal of Neurophysiology*, 106(3):1125–1165, 2011.
41. R.N. Mantegna. Hierarchical structure in financial markets. *European Physical Journal B*, 11(1):193–197, 1999.
42. S.I. Dimitriadis, M. Antonakakis, P. Simos, J.M. Fletcher, and A.C. Papanicolaou. Data-driven topological filtering based on orthogonal minimal spanning trees: Application to multigroup magnetoencephalography resting-state connectivity. *Brain Connectivity*, 7(10): 661–670, 2017.
43. M. Tumminello, T. Aste, T. Di Matteo, and R.N. Mantegna. A tool for filtering information in complex systems. *Proceedings of the National Academy of Sciences of the United States of America*, 102(30):10421–10426, 2005.
44. G.P. Massara, T. Di Matteo, and T. Aste. Network filtering for big data: Triangulated maximally filtered graph. *Journal of Complex Networks*, 5(2):161–178, 2016.
45. D S Bassett, E Bullmore, B A Verchinski, V S Mattay, D R Weinberger, and A Meyer-Lindenberg. Hierarchical organization of human cortical networks in health and schizophrenia. *The Journal of Neuroscience*, 28(37):9239–9248, 2008.
46. S.B. Eickhoff, B. Thirion, G. Varoquaux, and D. Bzdok. Connectivity-based parcellation: Critique and implications. *Human Brain Mapping*, 36(12):4771–4792, 2015.
47. A. Fornito, A. Zalesky, and M. Breakspear. Graph analysis of the human connectome: Promise, progress, and pitfalls. *NeuroImage*, 80:426–444, 2013.
48. A. Zalesky, A. Fornito, I.H. Harding, L. Cocchi, M. Yücel, C. Pantelis, and E.T. Bullmore. Whole-brain anatomical networks: Does the choice of nodes matter? *NeuroImage*, 50(3): 970–983, 2010.
49. X.-N. Zuo, B.B. Biswal, and R.A. Poldrack. Editorial: Reliability and reproducibility in functional connectomics. *Frontiers in Neuroscience*, 13:117, 2019.
50. G.E. Alexander, M.R. DeLong, and P.L. Strick. Parallel organization of functionally segregated circuits linking basal ganglia and cortex. *Annual Review of Neuroscience*, 9:357–381, 1986.
51. P.L. Strick. How do the basal ganglia and cerebellum gain access to the cortical motor areas? *Behavioural Brain Research*, 18(2):107–123, 1985.
52. A.C. Bostan and P.L. Strick. The basal ganglia and the cerebellum: Nodes in an integrated network. *Nature Reviews Neuroscience*, 19(6):338–350, 2018.
53. M.G. Packard and B.J. Knowlton. Learning and memory functions of the basal ganglia. *Annual Review of Neuroscience*, 25:563–593, 2002.
54. A. Di Martino, A. Scheres, D.S. Margulies, A.M.C. Kelly, L.Q. Uddin, Z. Shehzad, B. Biswal, J.R. Walters, F.X. Castellanos, and M.P. Milham. Functional connectivity of human striatum: A resting state fMRI study. *Cerebral Cortex*, 18(12):2735–2747, 2008.
55. E.Y. Choi, B.T. Thomas Yeo, and R.L. Buckner. The organization of the human striatum estimated by intrinsic functional connectivity. *Journal of Neurophysiology*, 108(8):2242–2263, 2012.
56. R.L. Buckner, F.M. Krienen, A. Castellanos, J.C. Diaz, and B.T. Thomas Yeo. The organization of the human cerebellum estimated by intrinsic functional connectivity. *Journal of Neurophysiology*, 106(5):2322–2345, 2011.
57. S. Marek, J.S. Siegel, E.M. Gordon, R.V. Raut, C. Gratton, D.J. Newbold, M. Ortega, T.O. Laumann, B. Adeyemo, D.B. Miller, A. Zheng, K.C. Lopez, J.J. Berg, R.S. Coalson, A.L. Nguyen, D. Dierker, A.N. Van, C.R. Hoyt, K.B. McDermott, S.A. Norris, J.S. Shimony, A.Z. Snyder, S.M. Nelson, D.M. Barch, B.L. Schlaggar, M.E. Raichle, S.E. Petersen, D.J. Greene, and N.U.F. Dosenbach. Spatial and temporal organization of the individual human cerebellum. *Neuron*, 100(4):977–993.e7, 2018.
58. K.A. Barnes, A.L. Cohen, J.D. Power, S.M. Nelson, Y.B.L. Dosenbach, F.M. Miezin, S.E. Petersen, and B.L. Schlaggar. Identifying basal ganglia divisions in individuals using resting-state functional connectivity MRI. *Frontiers in Systems Neuroscience*, 4:18, 2010.
59. M. Garcia-Garcia, A. Nikolaidis, P. Bellec, R.C. Craddock, B. Cheung, F.X. Castellanos, and M.P. Milham. Detecting stable individual differences in the functional organization of the human basal ganglia. *NeuroImage*, 170:68–82, 2018.
60. D.J. Greene, S. Marek, E.M. Gordon, J.S. Siegel, C. Gratton, T.O. Laumann, A.W. Gilmore, J.J. Berg, A.L. Nguyen, D. Dierker, A.N. Van, M. Ortega, D.J. Newbold, J.M. Hampton, A.N. Nielsen, K.B. McDermott, J.L. Roland, S.A. Norris, S.M. Nelson, A.Z. Snyder, B.L. Schlaggar, S.E. Petersen, and N.U.F. Dosenbach. Integrative and network-specific connectivity of the basal ganglia and thalamus defined in individuals. *Neuron*, 105(4):742–758.e6, 2020.

bioRxiv preprint doi: https://doi.org/10.1101/2021.05.06.442886; this version posted September 4, 2021. The copyright holder for this preprint (which was not certified by peer review) is the author/funder, who has granted bioRxiv a license to display the preprint in perpetuity. It is made available under aCC-BY-NC-ND 4.0 International license.

61. R. Sala-Llonch, S.M. Smith, M. Woolrich, and E.P. Duff. Spatial parcellations, spectral filtering, and connectivity measures in fMRI: Optimizing for discrimination. *Human Brain Mapping*, 40(2):407–419, 2019.
62. Usama Pervaiz, Diego Vidaurre, Mark W. Woolrich, and Stephen M. Smith. Optimising network modelling methods for fMRI. *NeuroImage*, 211:116604, 2020.
63. X.-N. Zuo, C. Kelly, J.S. Adelstein, D.F. Klein, F.X. Castellanos, and M.P. Milham. Reliable intrinsic connectivity networks: Test-retest evaluation using ICA and dual regression approach. *NeuroImage*, 49(3):2163–2177, 2010.
64. S. Achard, R. Salvador, B. Whitcher, J. Suckling, and E. Bullmore. A resilient, low-frequency, small-world human brain functional network with highly connected association cortical hubs. *The Journal of Neuroscience*, 26(1):63–72, 2006.
65. Y. Wang, Q. Zou, Y. Ao, Y. Liu, Y. Ouyang, X. Wang, B. Biswal, Q. Cui, and H. Chen. Frequency-dependent circuits anchored in the dorsal and ventral left anterior insula. *Scientific Reports*, 10(1):16394, 2020.
66. E. Bullmore and O. Sporns. The economy of brain network organization. *Nature Reviews Neuroscience*, 13(5):336–349, 2012.
67. D.S. Bassett, B.G. Nelson, B.A. Mueller, J. Camchong, and K.O. Lim. Altered resting state complexity in schizophrenia. *NeuroImage*, 59(3):2196–2207, 2012.
68. M.W. Cole, T. Yarkoni, G. Repovš, A. Anticevic, and T.S. Braver. Global connectivity of prefrontal cortex predicts cognitive control and intelligence. *The Journal of Neuroscience*, 32(26):8988–8999, 2012.
69. E. Santarnecchi, G. Galli, N.R. Polizzotto, A. Rossi, and S. Rossi. Efficiency of weak brain connections support general cognitive functioning. *Human Brain Mapping*, 35(9): 4566–4582, 2014.
70. J. Faskowitz, F.Z. Esfahlani, Y. Jo, O. Sporns, and R.F. Betzel. Edge-centric functional network representations of human cerebral cortex reveal overlapping system-level architecture. *Nature Neuroscience*, 23(12):1644–1654, 2020.
71. T.S. Jackson and N. Read. Theory of minimum spanning trees. i. mean-field theory and strongly disordered spin-glass model. *Physical Review E - Statistical, Nonlinear, and Soft Matter Physics*, 81(2):021130, 2010.
72. X.-N. Zuo, R. Ehmke, M. Mennes, D. Imperati, F.X. Castellanos, O. Sporns, and M.P. Milham. Network centrality in the human functional connectome. *Cerebral Cortex*, 22(8): 1862–1875, 2012.
73. Mehraveh Salehi, Amin Karbasi, Daniel S Barron, Dustin Scheinost, and R Todd Constable. Individualized functional networks reconfigure with cognitive state. *NeuroImage*, 206: 116233, 2020.
74. P. Rakic. Evolution of the neocortex: A perspective from developmental biology. *Nature Reviews Neuroscience*, 10(10):724–735, 2009.
75. C.-H. Chen, E.D. Gutierrez, W. Thompson, M.S. Panizzon, T.L. Jernigan, L.T. Eyler, C. Fennema-Notestine, A.J. Jak, M.C. Neale, C.E. Franz, M.J. Lyons, M.D. Grant, B. Fischl, L.J. Seidman, M.T. Tsuang, W.S. Kremen, and A.M. Dale. Hierarchical genetic organization of human cortical surface area. *Science*, 335(6076):1634–1636, 2012.
76. C.-H. Chen, M. Fiecas, E.D. Gutiérrez, M.S. Panizzon, L.T. Eyler, E. Vuoksimaa, W.K. Thompson, C. Fennema-Notestine, D.J. Hagler Jr., T.L. Jernigan, M.C. Neale, C.E. Franz, M.J. Lyons, B. Fischl, M.T. Tsuang, A.M. Dale, and W.S. Kremen. Genetic topography of brain morphology. *Proceedings of the National Academy of Sciences of the United States of America*, 110(42):17089–17094, 2013.
77. J.A. Miller, S.-L. Ding, S.M. Sunkin, K.A. Smith, L. Ng, A. Szafer, A. Ebbert, Z.L. Riley, J.J. Royall, K. Aiona, J.M. Arnold, C. Bennet, D. Bertagnolli, K. Brouner, S. Butler, S. Caldejon, A. Carey, C. Cuhaciyan, R.A. Dalley, N. Dee, T.A. Dolbeare, B.A.C. Facer, D. Feng, T.P. Fliss, G. Gee, J. Goldy, L. Gourley, B.W. Gregor, G. Gu, R.E. Howard, J.M. Jochim, C.L. Kuan, C. Lau, C.-K. Lee, F. Lee, T.A. Lemon, P. Lesnar, B. McMurray, N. Mastan, N. Mosqueda, T. Naluai-Cecchini, N.-K. Ngo, J. Nyhus, A. Oldre, E. Olson, J. Parente, P.D. Parker, S.E. Parry, A. Stevens, M. Pletikos, M. Reding, K. Roll, D. Sandman, M. Sarreal, S. Shapouri, N.V. Shapovalova, E.H. Shen, N. Sjoquist, C.R. Slaughterbeck, M. Smith, A.J. Sodt, D. Williams, L. Zöllei, B. Fischl, M.B. Gerstein, D.H. Geschwind, I.A. Glass, M.J. Hawrylycz, R.F. Hevner, H. Huang, A.R. Jones, J.A. Knowles, P. Levitt, J.W. Phillips, N. Šestan, P. Wohnoutka, C. Dang, A. Bernard, J.G. Hohmann, and E.S. Lein. Transcriptional landscape of the prenatal human brain. *Nature*, 508(7495):199–206, 2014.
78. S.M. Smith, C.F. Beckmann, J. Andersson, E.J. Auerbach, J. Bijsterbosch, G. Douaud, E. Duff, D.A. Feinberg, L. Griffanti, M.P. Harms, M. Kelly, T. Laumann, K.L. Miller, S. Moeller, S. Petersen, J. Power, G. Salimi-Khorshidi, A.Z. Snyder, A.T. Vu, M.W. Woolrich, J. Xu, E. Yacoub, K. Uğurbil, D.C. Van Essen, and M.F. Glasser. Resting-state fMRI in the Human Connectome Project. *NeuroImage*, 80:144–168, 2013.
79. O. Sporns. Network attributes for segregation and integration in the human brain. *Current Opinion in Neurobiology*, 23(2):162–171, 2013.
80. T.S. Coalson, D.C. Van Essen, and M.F. Glasser. The impact of traditional neuroimaging methods on the spatial localization of cortical areas. *Proceedings of the National Academy of Sciences of the United States of America*, 115(27):E6356–E6365, 2018.
81. M.F. Glasser, T.S. Coalson, E.C. Robinson, C.D. Hacker, J. Harwell, E. Yacoub, K. Ugurbil, J. Andersson, C.F. Beckmann, M. Jenkinson, S.M. Smith, and D.C. Van Essen. A multimodal parcellation of human cerebral cortex. *Nature*, 536(7615):171–178, 2016.
82. A. Schaefer, R. Kong, E.M. Gordon, T.O. Laumann, X.-N. Zuo, A.J. Holmes, S.B. Eickhoff, and B.T.T. Yeo. Local-global parcellation of the human cerebral cortex from intrinsic functional connectivity MRI. *Cerebral Cortex*, 28(9):3095–3114, 2018.
83. L. Fan, H. Li, J. Zhuo, Y. Zhang, J. Wang, L. Chen, Z. Yang, C. Chu, S. Xie, A.R. Laird, P.T. Fox, S.B. Eickhoff, C. Yu, and T. Jiang. The Human Brainnetome Atlas: A new brain atlas based on connectional architecture. *Cerebral Cortex*, 26(8):3508–3526, 2016.
84. R.S. Desikan, F. Ségonne, B. Fischl, B.T. Quinn, B.C. Dickerson, D. Blacker, R.L. Buckner, A.M. Dale, R.P. Maguire, B.T. Hyman, M.S. Albert, and R.J. Killiany. An automated labeling system for subdividing the human cerebral cortex on mri scans into gyral based regions of interest. *NeuroImage*, 31(3):968–980, 2006.
85. J.L. Ji, M. Spronk, K. Kulkarni, G. Repovš, A. Anticevic, and M.W. Cole. Mapping the human brain's cortical-subcortical functional network organization. *NeuroImage*, 185:35–57, 2019.
86. M.D. Fox and M.E. Raichle. Spontaneous fluctuations in brain activity observed with functional magnetic resonance imaging. *Nature Reviews Neuroscience*, 8(9):700–711, 2007.
87. D. Cordes, V.M. Haughton, K. Arfanakis, J.D. Carew, P.A. Turski, C.H. Moritz, M.A. Quigley, and M.E. Meyerand. Frequencies contributing to functional connectivity in the cerebral cortex in "resting-state" data. *American Journal of Neuroradiology*, 22(7):1326–1333, 2001.
88. R. Salvador, J. Suckling, M.R. Coleman, J.D. Pickard, D. Menon, and E. Bullmore. Neurophysiological architecture of functional magnetic resonance images of human brain. *Cerebral Cortex*, 15(9):1332–2342, 2005.
89. R.N. Boubela, K. Kalcher, W. Huf, C. Kronnerwetter, P. Filzmoser, and E. Moser. Beyond noise: Using temporal ICA to extract meaningful information from high-frequency fMRI signal fluctuations during rest. *Frontiers in Human Neuroscience*, 7:168, 2013.
90. P. Hagmann, M. Kurant, X. Gigandet, P. Thiran, V.J. Wedeen, R. Meuli, and J.-P. Thiran. Mapping human whole-brain structural networks with diffusion MRI. *PLoS One*, 2(7):e597, 2007.
91. Martijn P van den Heuvel, Siemon C de Lange, Andrew Zalesky, Caio Seguin, BT Thomas Yeo, and Ruben Schmidt. Proportional thresholding in resting-state fMRI functional connectivity networks and consequences for patient-control connectome studies: Issues and recommendations. *NeuroImage*, 152:437–449, 2017.
92. DS Bassett, ET Bullmore, A Meyer-Lindenberg, JA Apud, DR Weinberger, and R Coppola. Cognitive fitness of cost-efficient brain functional networks. *Proceedings of the National Academy of Sciences of the United States of America*, 106(28):11747–11752, 2009.
93. M. Rubinov, O. Sporns, C. van Leeuwen, and M. Breakspear. Symbiotic relationship between brain structure and dynamics. *BMC Neuroscience*, 10:55, 2009.
94. Cedric E Ginestet, Thomas E Nichols, Ed T Bullmore, and Andrew Simmons. Brain network analysis: separating cost from topology using cost-integration. *PLoS One*, 6(7): e21570, 2011.
95. K A Garrison, D Scheinost, E S Finn, X Shen, and R T Constable. The (in)stability of functional brain network measures across thresholds. *NeuroImage*, 118:651–661, 2015.
96. R Milo, S Shen-Orr, S Itzkovitz, N Kashtan, D Chklovskii, and U Alon. Network motifs: simple building blocks of complex networks. *Science*, 298(5594):824–827, 2002.
97. C Stam, B Jones, G Nolte, M Breakspear, and P Scheltens. Small-world networks and functional connectivity in Alzheimer's disease. *Cerebral Cortex*, 17(1):92–99, 2006.
98. Stavros I Dimitriadis, Nikolaos A Laskaris, Yolanda Del Rio-Portilla, and George Ch Koudounis. Characterizing dynamic functional connectivity across sleep stages from EEG. *Brain Topography*, 22(2):119–133, 2009.
99. S Micheloyannis, E Pachou, C J Stam, M Breakspear, P Bitsios, M Vourkas, S Erimaki, and M Zervakis. Small-world networks and disturbed functional connectivity in schizophrenia. *Schizophrenia Research*, 87(1-3):60–66, 2006.
100. Vito Latora and Massimo Marchiori. Efficient behavior of small-world networks. *Physical Review Letters*, 87(19):198701, 2001.
101. F. De Vico Fallani, V. Latora, and M. Chavez. A topological criterion for filtering information in complex brain networks. *PLoS Computational Biology*, 13(1):e1005305, 2017.
102. J. Meier, P. Tewarie, and P. Van Mieghem. The union of shortest path trees of functional brain networks. *Brain Connectivity*, 5(9):575–581, 2015.
103. D. van Nieuwenhuizen, L. Douw, M. Klein, S.M. Peerdeman, J.J. Heimans, J.C. Reijneveld, C.J. Stam, and A. Hillebrand. Cognitive functioning and functional brain networks in postoperative WHO grade I meningioma patients. *Journal of Neuro-Oncology*, 140(3): 605–613, 2018.
104. W.M. Otte, E. van Diessen, S. Paul, R. Ramaswamy, V.P. Subramanyam Rallabandi, C.J. Stam, and P.K. Roy. Aging alterations in whole-brain networks during adulthood mapped with the minimum spanning tree indices: The interplay of density, connectivity cost and life-time trajectory. *NeuroImage*, 109:171–189, 2015.
105. H. Guo, M. Qin, J. Chen, Y. Xu, and J. Xiang. Machine-learning classifier for patients with major depressive disorder: Multifeature approach based on a high-order minimum spanning tree functional brain network. *Computational and Mathematical Methods in Medicine*, 2017:4820935, 2017.
106. W.-M. Song, T. Di Matteo, and T. Aste. Hierarchical information clustering by means of topologically embedded graphs. *PLoS One*, 7(3):e31929, 2012.
107. A.P. Christensen, Y.N. Kenett, T. Aste, P.J. Silvia, and T.R. Kwapil. Network structure of the wisconsin schizotypy scales–short forms: Examining psychometric network filtering approaches. *Behavior Research Methods*, 50(6):2531–2550, 2018.
108. M. Rubinov and O. Sporns. Complex network measures of brain connectivity: Uses and interpretations. *NeuroImage*, 52(3):1059–1069, 2010.
109. T.K. Koo and M.Y. Li. A guideline of selecting and reporting intraclass correlation coefficients for reliability research. *Journal of Chiropractic Medicine*, 15(2):155–163, 2016.

bioRxiv preprint doi: https://doi.org/10.1101/2021.05.06.442886; this version posted September 4, 2021. The copyright holder for this preprint (which was not certified by peer review) is the author/funder, who has granted bioRxiv a license to display the preprint in perpetuity. It is made available under aCC-BY-NC-ND 4.0 International license.

Supplementary Information

Toward Reliable Network Neuroscience for Mapping Individual Differences

Contents

List of Figures 2

List of Tables 3

1 Parcellations - Node Definition 4
- 1.1 ICC Density distribution . . . 4
- 1.2 ICC Almost Perfect (ICCs > 0.8) . . . 5
- 1.3 Substantial or Above (ICCs > 0.6) . . . 6
- 1.4 Descriptive statistics Mean . . . 8
- 1.5 Descriptive statistics Median . . . 9
- 1.6 Friedman Test . . . 9
- 1.7 Friedman Test Effect size . . . 9
- 1.8 Paired Wilcoxon signed rank test . . . 10
- 1.9 Significance Map . . . 17
- 1.10 Effect size . . . 17
- 1.11 Variability Changes . . . 24

2 Frequency Bands - Edge Construction 26
- 2.1 ICC Density distribution . . . 26
- 2.2 Almost Perfect (ICCs > 0.8) . . . 26
- 2.3 Substantial or Above (ICCs > 0.6) . . . 27
- 2.4 Variability Changes . . . 28
- 2.5 Descriptive statistics Mean . . . 29
- 2.6 Descriptive statistics Median . . . 29
- 2.7 Friedman Test . . . 30
- 2.8 Friedman Test Effect size . . . 30
- 2.9 Paired Wilcoxon signed rank test . . . 30
- 2.10 Significance Map . . . 31
- 2.11 Effect size . . . 31

3 R Tranforms - Edge Construction 32
- 3.1 ICC Density distribution . . . 33
- 3.2 Almost Perfect (ICCs > 0.8) . . . 33
- 3.3 Substantial or Above (ICCs > 0.6) . . . 34
- 3.4 Descriptive statistics Mean . . . 35
- 3.5 Descriptive statistics Median . . . 35
- 3.6 Friedman Test . . . 35
- 3.7 Friedman Test Effect size . . . 35
- 3.8 Paired Wilcoxon signed rank test . . . 35
- 3.9 Significance map . . . 36
- 3.10 Effect size . . . 36

4 Schemes - Edge Construction 37

bioRxiv preprint doi: https://doi.org/10.1101/2021.05.06.442886; this version posted September 4, 2021. The copyright holder for this preprint (which was not certified by peer review) is the author/funder, who has granted bioRxiv a license to display the preprint in perpetuity. It is made available under aCC-BY-NC-ND 4.0 International license.

4.1 ICC Density distribution . . . 37
4.2 Almost Perfect (ICCs > 0.8) . . . 38
4.3 Substantial or Above (ICCs > 0.6) . . . 39
4.4 Varibility Changes . . . 39
4.5 Descriptive statistics Mean . . . 41
4.6 Descriptive statistics Median . . . 42
4.7 Friedman Test . . . 42
4.8 Friedman Test Effect size . . . 42
4.9 Paired Wilcoxon signed rank test . . . 42
4.10 Significance map . . . 44
4.11 Effect size . . . 44

5 Metrics - Network Analysis **47**
5.1 Metrics . . . 47
5.2 ICC Density distribution . . . 48
5.3 Almost Perfect (ICCs > 0.8) . . . 48
5.4 Substantial or Above (ICCs > 0.6) . . . 49
5.5 Descriptive statistics Mean . . . 50
5.6 Descriptive statistics Median . . . 50
5.7 Paired Wilcoxon signed rank test . . . 50
5.8 Significance map . . . 51
5.9 Effect size . . . 52

6 More Metrics - Network Analysis **54**
6.1 ICC Density distribution . . . 54
6.2 Almost Perfect (ICCs > 0.8) . . . 55
6.3 Substantial or Above (ICCs > 0.6) . . . 56
6.4 Descriptive statistics Mean . . . 58
6.5 Descriptive statistics Median . . . 60
6.6 Significance map . . . 62

List of Figures

S1 Parcellation - Density distribution . . . 4
S2 Parcellation - Number of ICCs > 0.8 . . . 5
S3 Parcellation - Number of ICCs > 0.6 . . . 7
S4 Parcellation - Significance Map . . . 17
S5 Parcellation - Effect size . . . 24
S6 Parcellation - Variability Changes . . . 25
S7 Frequency - ICC Density distribution . . . 26
S8 Frequency - Number of ICC >0.8 . . . 26
S9 Frequency - Number of ICC >0.6 . . . 27
S10 Frequency - Variability Changes . . . 28
S11 Frequency - ICC Mean Bar plot . . . 29
S12 Frequency - Significance Map . . . 31
S13 Frequency - Effect size . . . 32
S14 Transform r to weight . . . 33
S15 Transforms - ICC Density distribution . . . 33
S16 Transforms - Number of ICC > 0.8 . . . 34
S17 Transforms - Number of ICC > 0.8 . . . 34
S18 Transforms - Significance Map . . . 36
S19 Transforms - Effect size . . . 37
S20 Schemes - ICC Density distribution . . . 37
S21 Schemes - Number of ICC > 0.8 . . . 38

bioRxiv preprint doi: https://doi.org/10.1101/2021.05.06.442886; this version posted September 4, 2021. The copyright holder for this preprint (which was not certified by peer review) is the author/funder, who has granted bioRxiv a license to display the preprint in perpetuity. It is made available under aCC-BY-NC-ND 4.0 International license.

S22 Schemes - Number of ICC > 0.6 . . . 39
S23 Schemes - Variability Changes . . . 40
S24 Schemes - ICC mean and se . . . 41
S25 Schemes - Significance Map . . . 44
S26 Schemes - Effect size . . . 46
S27 Metrics - Density distribution . . . 48
S28 Metrics - Number of ICC > 0.8 . . . 49
S29 Metrics - Number of ICC > 0.6 . . . 50
S30 Metrics - Significance Map . . . 51
S31 Metrics - Effect size . . . 53
S32 Metrics - Density distribution . . . 54
S33 Metrics - Number of ICC > 0.8 . . . 56
S34 Metrics - Number of ICC > 0.6 . . . 58
S35 Metrics - Significance Map . . . 62

List of Tables

S1 Parcellation - Number of ICCs > 0.8 . . . 5
S2 Parcellation - Number of ICCs > 0.6 . . . 6
S3 Parcellation - ICC Mean . . . 8
S4 Parcellation - ICC Median . . . 9
S5 Parcellation - Friedman Test . . . 9
S6 Parcellation - Friedman Test Effect size . . . 9
S7 Parcellation - Paired Wilcoxon signed rank test . . . 10
S8 Parcellation - Effect size . . . 17
S9 Frequency - ICC Mean . . . 29
S10 Frequency - ICC Median . . . 29
S11 Frequency - Friedman Test . . . 30
S12 Frequency - Friedman Test Effect size . . . 30
S13 Frequency - ICC group1 vs. group2 . . . 30
S14 Frequency - Effect size . . . 31
S15 Transforms - Number of ICCs > 0.8 . . . 33
S16 Transforms - Number of ICCs > 0.6 . . . 34
S17 Transforms - ICC Mean . . . 35
S18 Transforms - ICC Median . . . 35
S19 Transforms - Friedman Test . . . 35
S20 Transforms - Friedman Test Effect size . . . 35
S21 Transforms - ICC group1 vs. group2 . . . 35
S22 Transforms - Effect size . . . 36
S23 Schemes - Number of ICCs > 0.8 . . . 38
S24 Schemes - Number of ICCs > 0.8 . . . 39
S25 Schemes - ICC Mean . . . 41
S26 Schemes - ICC Median . . . 42
S27 Schemes - Friedman Test . . . 42
S28 Schemes - Friedman Test Effect size . . . 42
S29 Schemes - ICC group1 vs. group2 . . . 42
S30 Schemes - Effect size . . . 44
S31 Brief descriptions of the network metrics examined . . . 47
S32 Metrics - Number of ICCs > 0.8 . . . 48
S33 Metrics - Number of ICCs > 0.6 . . . 49
S34 Metrics - ICC Mean . . . 50
S35 Metrics - ICC Median . . . 50
S36 Metrics - ICC group1 vs. group2 . . . 51

bioRxiv preprint doi: https://doi.org/10.1101/2021.05.06.442886; this version posted September 4, 2021. The copyright holder for this preprint (which was not certified by peer review) is the author/funder, who has granted bioRxiv a license to display the preprint in perpetuity. It is made available under aCC-BY-NC-ND 4.0 International license.

S37 Metrics - Effect size 52
S38 Metrics - Number of ICCs > 0.8 55
S39 Metrics - Number of ICCs > 0.6 56
S40 Metrics - ICC Mean 59
S41 Metrics - ICC Median 60

1 Parcellations - Node Definition

1.1 ICC Density distribution

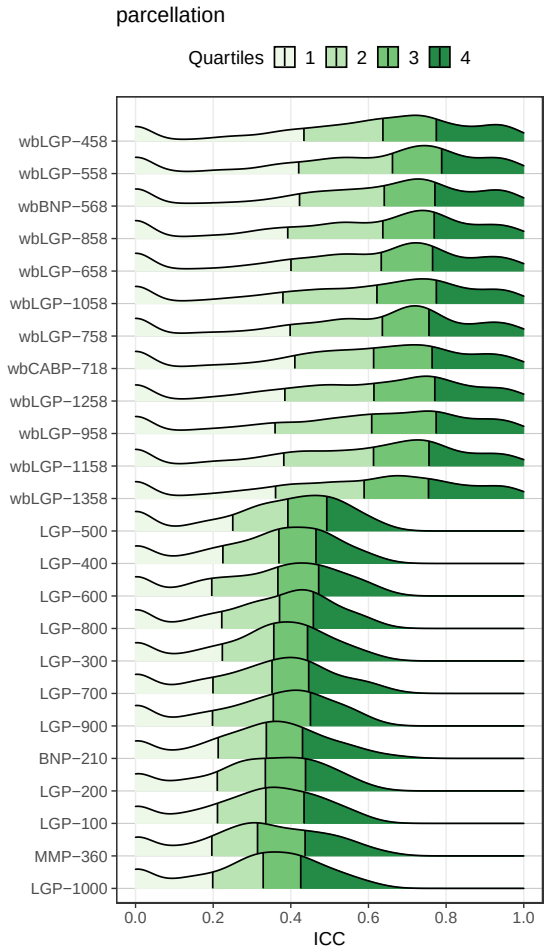

Fig. S1. Parcellation - Density distribution

bioRxiv preprint doi: https://doi.org/10.1101/2021.05.06.442886; this version posted September 4, 2021. The copyright holder for this preprint (which was not certified by peer review) is the author/funder, who has granted bioRxiv a license to display the preprint in perpetuity. It is made available under aCC-BY-NC-ND 4.0 International license.

1.2 ICC Almost Perfect (ICCs > 0.8)

Table S1. Parcellation - Number of ICCs > 0.8

parcellation	n	ratio
wbLGP-558	540	0.2295918
wbLGP-458	519	0.2206633
wbBNP-568	511	0.2172619
wbLGP-958	486	0.2066327
wbLGP-1058	484	0.2057823
wbLGP-1258	482	0.2049320
wbLGP-858	478	0.2032313
wbCABP-718	463	0.1968537
wbLGP-658	444	0.1887755
wbLGP-1358	440	0.1870748
wbLGP-1158	416	0.1768707
wbLGP-758	413	0.1755952

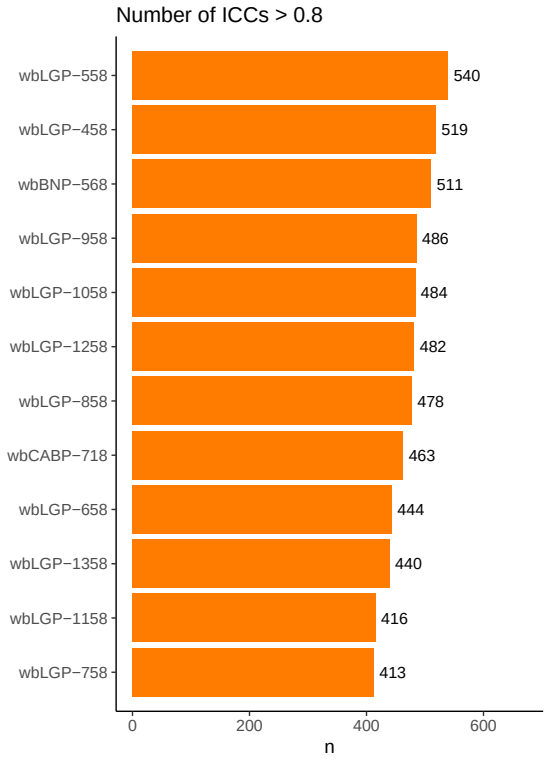

Fig. S2. Parcellation - Number of ICCs > 0.8

bioRxiv preprint doi: https://doi.org/10.1101/2021.05.06.442886; this version posted September 4, 2021. The copyright holder for this preprint (which was not certified by peer review) is the author/funder, who has granted bioRxiv a license to display the preprint in perpetuity. It is made available under aCC-BY-NC-ND 4.0 International license.

1.3 Substantial or Above (ICCs > 0.6)

Table S2. Parcellation - Number of ICCs > 0.6

parcellation	n	ratio
wbLGP-458	1328	0.5646259
wbLGP-558	1320	0.5612245
wbBNP-568	1298	0.5518707
wbLGP-858	1263	0.5369898
wbLGP-758	1248	0.5306122
wbLGP-658	1245	0.5293367
wbLGP-1058	1239	0.5267857
wbCABP-718	1224	0.5204082
wbLGP-1258	1216	0.5170068
wbLGP-1158	1211	0.5148810
wbLGP-958	1209	0.5140306
wbLGP-1358	1141	0.4851190
LGP-500	97	0.0412415
LGP-700	92	0.0391156
LGP-600	85	0.0361395
BNP-210	71	0.0301871
MMP-360	66	0.0280612
LGP-400	51	0.0216837
LGP-300	47	0.0199830
LGP-800	46	0.0195578
LGP-900	38	0.0161565
LGP-1000	37	0.0157313
LGP-200	24	0.0102041
LGP-100	21	0.0089286

bioRxiv preprint doi: https://doi.org/10.1101/2021.05.06.442886; this version posted September 4, 2021. The copyright holder for this preprint (which was not certified by peer review) is the author/funder, who has granted bioRxiv a license to display the preprint in perpetuity. It is made available under aCC-BY-NC-ND 4.0 International license.

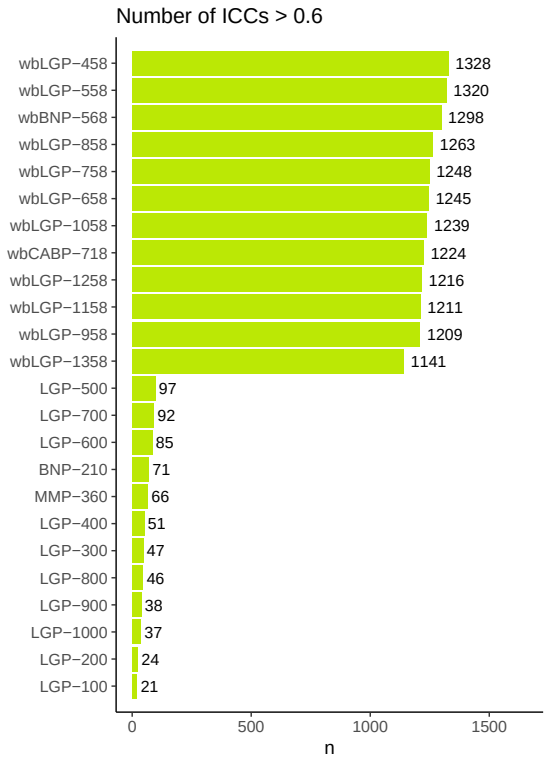

Fig. S3. Parcellation - Number of ICCs > 0.6

bioRxiv preprint doi: https://doi.org/10.1101/2021.05.06.442886; this version posted September 4, 2021. The copyright holder for this preprint (which was not certified by peer review) is the author/funder, who has granted bioRxiv a license to display the preprint in perpetuity. It is made available under aCC-BY-NC-ND 4.0 International license.

1.4 Descriptive statistics Mean

Table S3. Parcellation - ICC Mean

parcellation	variable	n	mean	mean_z2r
wbLGP-458	ICC.z	2352	0.813	0.6712419
wbLGP-558	ICC.z	2352	0.812	0.6706921
wbBNP-568	ICC.z	2352	0.800	0.6640368
wbLGP-858	ICC.z	2352	0.777	0.6509814
wbLGP-658	ICC.z	2352	0.775	0.6498275
wbLGP-1058	ICC.z	2352	0.770	0.6469295
wbCABP-718	ICC.z	2352	0.765	0.6440126
wbLGP-758	ICC.z	2352	0.765	0.6440126
wbLGP-1258	ICC.z	2352	0.764	0.6434270
wbLGP-958	ICC.z	2352	0.760	0.6410770
wbLGP-1158	ICC.z	2352	0.746	0.6327565
wbLGP-1358	ICC.z	2352	0.731	0.6236768
LGP-500	ICC.z	2352	0.379	0.3618387
LGP-400	ICC.z	2352	0.356	0.3416859
LGP-600	ICC.z	2352	0.354	0.3399182
LGP-800	ICC.z	2352	0.354	0.3399182
LGP-300	ICC.z	2352	0.347	0.3337123
LGP-700	ICC.z	2352	0.344	0.3310437
LGP-900	ICC.z	2352	0.340	0.3274774
BNP-210	ICC.z	2352	0.335	0.3230063
LGP-200	ICC.z	2352	0.330	0.3185208
LGP-100	ICC.z	2352	0.329	0.3176219
MMP-360	ICC.z	2352	0.326	0.3149220
LGP-1000	ICC.z	2352	0.324	0.3131193

bioRxiv preprint doi: https://doi.org/10.1101/2021.05.06.442886; this version posted September 4, 2021. The copyright holder for this preprint (which was not certified by peer review) is the author/funder, who has granted bioRxiv a license to display the preprint in perpetuity. It is made available under aCC-BY-NC-ND 4.0 International license.

1.5 Descriptive statistics Median

Table S4. Parcellation - ICC Median

parcellation	variable	n	median
wbLGP-558	ICC	2352	0.662
wbBNP-568	ICC	2352	0.641
wbLGP-458	ICC	2352	0.637
wbLGP-858	ICC	2352	0.637
wbLGP-758	ICC	2352	0.636
wbLGP-658	ICC	2352	0.633
wbLGP-1058	ICC	2352	0.622
wbLGP-1258	ICC	2352	0.614
wbCABP-718	ICC	2352	0.613
wbLGP-1158	ICC	2352	0.613
wbLGP-958	ICC	2352	0.608
wbLGP-1358	ICC	2352	0.589
LGP-500	ICC	2352	0.392
LGP-800	ICC	2352	0.371
LGP-400	ICC	2352	0.369
LGP-600	ICC	2352	0.367
LGP-300	ICC	2352	0.356
LGP-900	ICC	2352	0.355
LGP-700	ICC	2352	0.352
BNP-210	ICC	2352	0.337
LGP-100	ICC	2352	0.335
LGP-200	ICC	2352	0.334
LGP-1000	ICC	2352	0.329
MMP-360	ICC	2352	0.314

1.6 Friedman Test

Table S5. Parcellation - Friedman Test

.y.	n	statistic	df	p	method
ICC.z	2352	20379.07	23	0	Friedman test

1.7 Friedman Test Effect size

Table S6. Parcellation - Friedman Test Effect size

.y.	n	effsize	method	magnitude
ICC.z	2352	0.3767205	Kendall W	moderate

bioRxiv preprint doi: https://doi.org/10.1101/2021.05.06.442886; this version posted September 4, 2021. The copyright holder for this preprint (which was not certified by peer review) is the author/funder, who has granted bioRxiv a license to display the preprint in perpetuity. It is made available under aCC-BY-NC-ND 4.0 International license.

1.8 Paired Wilcoxon signed rank test

Table S7. Parcellation - Paired Wilcoxon signed rank test

group1	group2	n1	statistic	alternative	p	p.adj	p.adj.signif
BNP-210	LGP-100	2352	1302001	two.sided	1.60e-02	1.0000000	ns
BNP-210	LGP-1000	2352	1379617	two.sided	0.00e+00	0.0000030	****
BNP-210	LGP-200	2352	1330962	two.sided	2.00e-03	0.5520000	ns
BNP-210	LGP-300	2352	1047149	two.sided	0.00e+00	0.0000037	****
BNP-210	LGP-400	2352	928029	two.sided	0.00e+00	0.0000000	****
BNP-210	LGP-500	2352	686156	two.sided	0.00e+00	0.0000000	****
BNP-210	LGP-600	2352	1004541	two.sided	0.00e+00	0.0000000	****
BNP-210	LGP-700	2352	1105948	two.sided	1.76e-04	0.0485760	*
BNP-210	LGP-800	2352	945406	two.sided	0.00e+00	0.0000000	****
BNP-210	LGP-900	2352	1144573	two.sided	8.00e-03	1.0000000	ns
BNP-210	MMP-360	2352	1340035	two.sided	2.40e-04	0.0662400	ns
BNP-210	wbBNP-568	2352	160500	two.sided	0.00e+00	0.0000000	****
BNP-210	wbCABP-718	2352	162989	two.sided	0.00e+00	0.0000000	****
BNP-210	wbLGP-1058	2352	176518	two.sided	0.00e+00	0.0000000	****
BNP-210	wbLGP-1158	2352	199995	two.sided	0.00e+00	0.0000000	****
BNP-210	wbLGP-1258	2352	180282	two.sided	0.00e+00	0.0000000	****
BNP-210	wbLGP-1358	2352	232751	two.sided	0.00e+00	0.0000000	****
BNP-210	wbLGP-458	2352	145336	two.sided	0.00e+00	0.0000000	****
BNP-210	wbLGP-558	2352	148873	two.sided	0.00e+00	0.0000000	****
BNP-210	wbLGP-658	2352	175789	two.sided	0.00e+00	0.0000000	****
BNP-210	wbLGP-758	2352	180496	two.sided	0.00e+00	0.0000000	****
BNP-210	wbLGP-858	2352	170819	two.sided	0.00e+00	0.0000000	****
BNP-210	wbLGP-958	2352	189206	two.sided	0.00e+00	0.0000000	****
LGP-100	LGP-1000	2352	1315278	two.sided	6.00e-03	1.0000000	ns
LGP-100	LGP-200	2352	1255194	two.sided	5.26e-01	1.0000000	ns
LGP-100	LGP-300	2352	1010235	two.sided	0.00e+00	0.0000000	****
LGP-100	LGP-400	2352	912286	two.sided	0.00e+00	0.0000000	****
LGP-100	LGP-500	2352	659721	two.sided	0.00e+00	0.0000000	****
LGP-100	LGP-600	2352	981916	two.sided	0.00e+00	0.0000000	****
LGP-100	LGP-700	2352	1129951	two.sided	4.59e-04	0.1266840	ns
LGP-100	LGP-800	2352	994724	two.sided	0.00e+00	0.0000000	****
LGP-100	LGP-900	2352	1156218	two.sided	1.40e-02	1.0000000	ns
LGP-100	MMP-360	2352	1275769	two.sided	1.06e-01	1.0000000	ns
LGP-100	wbBNP-568	2352	159540	two.sided	0.00e+00	0.0000000	****
LGP-100	wbCABP-718	2352	161073	two.sided	0.00e+00	0.0000000	****
LGP-100	wbLGP-1058	2352	170565	two.sided	0.00e+00	0.0000000	****
LGP-100	wbLGP-1158	2352	187780	two.sided	0.00e+00	0.0000000	****
LGP-100	wbLGP-1258	2352	168428	two.sided	0.00e+00	0.0000000	****
LGP-100	wbLGP-1358	2352	215782	two.sided	0.00e+00	0.0000000	****
LGP-100	wbLGP-458	2352	130296	two.sided	0.00e+00	0.0000000	****

bioRxiv preprint doi: https://doi.org/10.1101/2021.05.06.442886; this version posted September 4, 2021. The copyright holder for this preprint (which was not certified by peer review) is the author/funder, who has granted bioRxiv a license to display the preprint in perpetuity. It is made available under aCC-BY-NC-ND 4.0 International license.

Table S7. Parcellation - Paired Wilcoxon signed rank test *(continued)*

group1	group2	n1	statistic	alternative	p	p.adj	p.adj.signif
LGP-100	wbLGP-558	2352	136606	two.sided	0.00e+00	0.0000000	****
LGP-100	wbLGP-658	2352	172094	two.sided	0.00e+00	0.0000000	****
LGP-100	wbLGP-758	2352	179105	two.sided	0.00e+00	0.0000000	****
LGP-100	wbLGP-858	2352	167470	two.sided	0.00e+00	0.0000000	****
LGP-100	wbLGP-958	2352	185024	two.sided	0.00e+00	0.0000000	****
LGP-1000	LGP-200	2352	1144843	two.sided	5.00e-03	1.0000000	ns
LGP-1000	LGP-300	2352	907429	two.sided	0.00e+00	0.0000000	****
LGP-1000	LGP-400	2352	756937	two.sided	0.00e+00	0.0000000	****
LGP-1000	LGP-500	2352	564982	two.sided	0.00e+00	0.0000000	****
LGP-1000	LGP-600	2352	766240	two.sided	0.00e+00	0.0000000	****
LGP-1000	LGP-700	2352	813046	two.sided	0.00e+00	0.0000000	****
LGP-1000	LGP-800	2352	724898	two.sided	0.00e+00	0.0000000	****
LGP-1000	LGP-900	2352	862540	two.sided	0.00e+00	0.0000000	****
LGP-1000	MMP-360	2352	1194004	two.sided	6.30e-01	1.0000000	ns
LGP-1000	wbBNP-568	2352	146449	two.sided	0.00e+00	0.0000000	****
LGP-1000	wbCABP-718	2352	133629	two.sided	0.00e+00	0.0000000	****
LGP-1000	wbLGP-1058	2352	143488	two.sided	0.00e+00	0.0000000	****
LGP-1000	wbLGP-1158	2352	152381	two.sided	0.00e+00	0.0000000	****
LGP-1000	wbLGP-1258	2352	140457	two.sided	0.00e+00	0.0000000	****
LGP-1000	wbLGP-1358	2352	180243	two.sided	0.00e+00	0.0000000	****
LGP-1000	wbLGP-458	2352	126403	two.sided	0.00e+00	0.0000000	****
LGP-1000	wbLGP-558	2352	130477	two.sided	0.00e+00	0.0000000	****
LGP-1000	wbLGP-658	2352	146959	two.sided	0.00e+00	0.0000000	****
LGP-1000	wbLGP-758	2352	146560	two.sided	0.00e+00	0.0000000	****
LGP-1000	wbLGP-858	2352	144497	two.sided	0.00e+00	0.0000000	****
LGP-1000	wbLGP-958	2352	151257	two.sided	0.00e+00	0.0000000	****
LGP-200	LGP-300	2352	925471	two.sided	0.00e+00	0.0000000	****
LGP-200	LGP-400	2352	832641	two.sided	0.00e+00	0.0000000	****
LGP-200	LGP-500	2352	576900	two.sided	0.00e+00	0.0000000	****
LGP-200	LGP-600	2352	932917	two.sided	0.00e+00	0.0000000	****
LGP-200	LGP-700	2352	1091274	two.sided	3.40e-06	0.0009301	***
LGP-200	LGP-800	2352	917094	two.sided	0.00e+00	0.0000000	****
LGP-200	LGP-900	2352	1112972	two.sided	1.30e-04	0.0358800	*
LGP-200	MMP-360	2352	1268709	two.sided	2.33e-01	1.0000000	ns
LGP-200	wbBNP-568	2352	144847	two.sided	0.00e+00	0.0000000	****
LGP-200	wbCABP-718	2352	149133	two.sided	0.00e+00	0.0000000	****
LGP-200	wbLGP-1058	2352	160610	two.sided	0.00e+00	0.0000000	****
LGP-200	wbLGP-1158	2352	180943	two.sided	0.00e+00	0.0000000	****
LGP-200	wbLGP-1258	2352	164714	two.sided	0.00e+00	0.0000000	****
LGP-200	wbLGP-1358	2352	207338	two.sided	0.00e+00	0.0000000	****
LGP-200	wbLGP-458	2352	130665	two.sided	0.00e+00	0.0000000	****

bioRxiv preprint doi: https://doi.org/10.1101/2021.05.06.442886; this version posted September 4, 2021. The copyright holder for this preprint (which was not certified by peer review) is the author/funder, who has granted bioRxiv a license to display the preprint in perpetuity. It is made available under aCC-BY-NC-ND 4.0 International license.

Table S7. Parcellation - Paired Wilcoxon signed rank test *(continued)*

group1	group2	n1	statistic	alternative	p	p.adj	p.adj.signif
LGP-200	wbLGP-558	2352	131597	two.sided	0.00e+00	0.0000000	****
LGP-200	wbLGP-658	2352	154264	two.sided	0.00e+00	0.0000000	****
LGP-200	wbLGP-758	2352	164041	two.sided	0.00e+00	0.0000000	****
LGP-200	wbLGP-858	2352	159660	two.sided	0.00e+00	0.0000000	****
LGP-200	wbLGP-958	2352	176411	two.sided	0.00e+00	0.0000000	****
LGP-300	LGP-400	2352	999180	two.sided	0.00e+00	0.0000000	****
LGP-300	LGP-500	2352	629869	two.sided	0.00e+00	0.0000000	****
LGP-300	LGP-600	2352	1060070	two.sided	2.00e-07	0.0000602	****
LGP-300	LGP-700	2352	1259128	two.sided	1.03e-01	1.0000000	ns
LGP-300	LGP-800	2352	1069448	two.sided	2.00e-07	0.0000538	****
LGP-300	LGP-900	2352	1299549	two.sided	6.00e-03	1.0000000	ns
LGP-300	MMP-360	2352	1483967	two.sided	0.00e+00	0.0000000	****
LGP-300	wbBNP-568	2352	164589	two.sided	0.00e+00	0.0000000	****
LGP-300	wbCABP-718	2352	158079	two.sided	0.00e+00	0.0000000	****
LGP-300	wbLGP-1058	2352	172650	two.sided	0.00e+00	0.0000000	****
LGP-300	wbLGP-1158	2352	196899	two.sided	0.00e+00	0.0000000	****
LGP-300	wbLGP-1258	2352	176738	two.sided	0.00e+00	0.0000000	****
LGP-300	wbLGP-1358	2352	227257	two.sided	0.00e+00	0.0000000	****
LGP-300	wbLGP-458	2352	143518	two.sided	0.00e+00	0.0000000	****
LGP-300	wbLGP-558	2352	144041	two.sided	0.00e+00	0.0000000	****
LGP-300	wbLGP-658	2352	173281	two.sided	0.00e+00	0.0000000	****
LGP-300	wbLGP-758	2352	170528	two.sided	0.00e+00	0.0000000	****
LGP-300	wbLGP-858	2352	163732	two.sided	0.00e+00	0.0000000	****
LGP-300	wbLGP-958	2352	186563	two.sided	0.00e+00	0.0000000	****
LGP-400	LGP-500	2352	767221	two.sided	0.00e+00	0.0000000	****
LGP-400	LGP-600	2352	1251633	two.sided	2.34e-01	1.0000000	ns
LGP-400	LGP-700	2352	1517947	two.sided	0.00e+00	0.0000000	****
LGP-400	LGP-800	2352	1303871	two.sided	1.20e-02	1.0000000	ns
LGP-400	LGP-900	2352	1477786	two.sided	0.00e+00	0.0000000	****
LGP-400	MMP-360	2352	1583190	two.sided	0.00e+00	0.0000000	****
LGP-400	wbBNP-568	2352	178030	two.sided	0.00e+00	0.0000000	****
LGP-400	wbCABP-718	2352	168997	two.sided	0.00e+00	0.0000000	****
LGP-400	wbLGP-1058	2352	190089	two.sided	0.00e+00	0.0000000	****
LGP-400	wbLGP-1158	2352	212433	two.sided	0.00e+00	0.0000000	****
LGP-400	wbLGP-1258	2352	188919	two.sided	0.00e+00	0.0000000	****
LGP-400	wbLGP-1358	2352	246801	two.sided	0.00e+00	0.0000000	****
LGP-400	wbLGP-458	2352	151198	two.sided	0.00e+00	0.0000000	****
LGP-400	wbLGP-558	2352	159132	two.sided	0.00e+00	0.0000000	****
LGP-400	wbLGP-658	2352	190283	two.sided	0.00e+00	0.0000000	****
LGP-400	wbLGP-758	2352	185190	two.sided	0.00e+00	0.0000000	****
LGP-400	wbLGP-858	2352	182103	two.sided	0.00e+00	0.0000000	****
LGP-400	wbLGP-958	2352	201977	two.sided	0.00e+00	0.0000000	****

bioRxiv preprint doi: https://doi.org/10.1101/2021.05.06.442886; this version posted September 4, 2021. The copyright holder for this preprint (which was not certified by peer review) is the author/funder, who has granted bioRxiv a license to display the preprint in perpetuity. It is made available under aCC-BY-NC-ND 4.0 International license.

Table S7. Parcellation - Paired Wilcoxon signed rank test *(continued)*

group1	group2	n1	statistic	alternative	p	p.adj	p.adj.signif
LGP-500	LGP-600	2352	1636990	two.sided	0.00e+00	0.0000000	****
LGP-500	LGP-700	2352	1775407	two.sided	0.00e+00	0.0000000	****
LGP-500	LGP-800	2352	1732442	two.sided	0.00e+00	0.0000000	****
LGP-500	LGP-900	2352	1731306	two.sided	0.00e+00	0.0000000	****
LGP-500	MMP-360	2352	1758329	two.sided	0.00e+00	0.0000000	****
LGP-500	wbBNP-568	2352	195928	two.sided	0.00e+00	0.0000000	****
LGP-500	wbCABP-718	2352	187217	two.sided	0.00e+00	0.0000000	****
LGP-500	wbLGP-1058	2352	202651	two.sided	0.00e+00	0.0000000	****
LGP-500	wbLGP-1158	2352	224307	two.sided	0.00e+00	0.0000000	****
LGP-500	wbLGP-1258	2352	206925	two.sided	0.00e+00	0.0000000	****
LGP-500	wbLGP-1358	2352	273700	two.sided	0.00e+00	0.0000000	****
LGP-500	wbLGP-458	2352	179170	two.sided	0.00e+00	0.0000000	****
LGP-500	wbLGP-558	2352	167854	two.sided	0.00e+00	0.0000000	****
LGP-500	wbLGP-658	2352	207577	two.sided	0.00e+00	0.0000000	****
LGP-500	wbLGP-758	2352	205183	two.sided	0.00e+00	0.0000000	****
LGP-500	wbLGP-858	2352	190097	two.sided	0.00e+00	0.0000000	****
LGP-500	wbLGP-958	2352	223872	two.sided	0.00e+00	0.0000000	****
LGP-600	LGP-700	2352	1517047	two.sided	0.00e+00	0.0000000	****
LGP-600	LGP-800	2352	1268374	two.sided	2.70e-02	1.0000000	ns
LGP-600	LGP-900	2352	1454702	two.sided	0.00e+00	0.0000000	****
LGP-600	MMP-360	2352	1486050	two.sided	0.00e+00	0.0000000	****
LGP-600	wbBNP-568	2352	151395	two.sided	0.00e+00	0.0000000	****
LGP-600	wbCABP-718	2352	146032	two.sided	0.00e+00	0.0000000	****
LGP-600	wbLGP-1058	2352	151532	two.sided	0.00e+00	0.0000000	****
LGP-600	wbLGP-1158	2352	174886	two.sided	0.00e+00	0.0000000	****
LGP-600	wbLGP-1258	2352	164221	two.sided	0.00e+00	0.0000000	****
LGP-600	wbLGP-1358	2352	210481	two.sided	0.00e+00	0.0000000	****
LGP-600	wbLGP-458	2352	142445	two.sided	0.00e+00	0.0000000	****
LGP-600	wbLGP-558	2352	138450	two.sided	0.00e+00	0.0000000	****
LGP-600	wbLGP-658	2352	156775	two.sided	0.00e+00	0.0000000	****
LGP-600	wbLGP-758	2352	158441	two.sided	0.00e+00	0.0000000	****
LGP-600	wbLGP-858	2352	148288	two.sided	0.00e+00	0.0000000	****
LGP-600	wbLGP-958	2352	145886	two.sided	0.00e+00	0.0000000	****
LGP-700	LGP-800	2352	994539	two.sided	0.00e+00	0.0000000	****
LGP-700	LGP-900	2352	1232646	two.sided	3.15e-01	1.0000000	ns
LGP-700	MMP-360	2352	1426998	two.sided	0.00e+00	0.0000000	****
LGP-700	wbBNP-568	2352	161398	two.sided	0.00e+00	0.0000000	****
LGP-700	wbCABP-718	2352	152205	two.sided	0.00e+00	0.0000000	****
LGP-700	wbLGP-1058	2352	163976	two.sided	0.00e+00	0.0000000	****
LGP-700	wbLGP-1158	2352	185951	two.sided	0.00e+00	0.0000000	****
LGP-700	wbLGP-1258	2352	167287	two.sided	0.00e+00	0.0000000	****
LGP-700	wbLGP-1358	2352	219346	two.sided	0.00e+00	0.0000000	****

bioRxiv preprint doi: https://doi.org/10.1101/2021.05.06.442886; this version posted September 4, 2021. The copyright holder for this preprint (which was not certified by peer review) is the author/funder, who has granted bioRxiv a license to display the preprint in perpetuity. It is made available under aCC-BY-NC-ND 4.0 International license.

Table S7. Parcellation - Paired Wilcoxon signed rank test *(continued)*

group1	group2	n1	statistic	alternative	p	p.adj	p.adj.signif
LGP-700	wbLGP-458	2352	142001	two.sided	0.00e+00	0.0000000	****
LGP-700	wbLGP-558	2352	145607	two.sided	0.00e+00	0.0000000	****
LGP-700	wbLGP-658	2352	169299	two.sided	0.00e+00	0.0000000	****
LGP-700	wbLGP-758	2352	169104	two.sided	0.00e+00	0.0000000	****
LGP-700	wbLGP-858	2352	164010	two.sided	0.00e+00	0.0000000	****
LGP-700	wbLGP-958	2352	173569	two.sided	0.00e+00	0.0000000	****
LGP-800	LGP-900	2352	1418708	two.sided	0.00e+00	0.0000000	****
LGP-800	MMP-360	2352	1553788	two.sided	0.00e+00	0.0000000	****
LGP-800	wbBNP-568	2352	181300	two.sided	0.00e+00	0.0000000	****
LGP-800	wbCABP-718	2352	172356	two.sided	0.00e+00	0.0000000	****
LGP-800	wbLGP-1058	2352	188254	two.sided	0.00e+00	0.0000000	****
LGP-800	wbLGP-1158	2352	193741	two.sided	0.00e+00	0.0000000	****
LGP-800	wbLGP-1258	2352	188270	two.sided	0.00e+00	0.0000000	****
LGP-800	wbLGP-1358	2352	242146	two.sided	0.00e+00	0.0000000	****
LGP-800	wbLGP-458	2352	162709	two.sided	0.00e+00	0.0000000	****
LGP-800	wbLGP-558	2352	160927	two.sided	0.00e+00	0.0000000	****
LGP-800	wbLGP-658	2352	189416	two.sided	0.00e+00	0.0000000	****
LGP-800	wbLGP-758	2352	190433	two.sided	0.00e+00	0.0000000	****
LGP-800	wbLGP-858	2352	183382	two.sided	0.00e+00	0.0000000	****
LGP-800	wbLGP-958	2352	201777	two.sided	0.00e+00	0.0000000	****
LGP-900	MMP-360	2352	1411598	two.sided	0.00e+00	0.0000000	****
LGP-900	wbBNP-568	2352	161762	two.sided	0.00e+00	0.0000000	****
LGP-900	wbCABP-718	2352	150635	two.sided	0.00e+00	0.0000000	****
LGP-900	wbLGP-1058	2352	167674	two.sided	0.00e+00	0.0000000	****
LGP-900	wbLGP-1158	2352	175152	two.sided	0.00e+00	0.0000000	****
LGP-900	wbLGP-1258	2352	162633	two.sided	0.00e+00	0.0000000	****
LGP-900	wbLGP-1358	2352	210734	two.sided	0.00e+00	0.0000000	****
LGP-900	wbLGP-458	2352	143322	two.sided	0.00e+00	0.0000000	****
LGP-900	wbLGP-558	2352	145640	two.sided	0.00e+00	0.0000000	****
LGP-900	wbLGP-658	2352	166904	two.sided	0.00e+00	0.0000000	****
LGP-900	wbLGP-758	2352	172439	two.sided	0.00e+00	0.0000000	****
LGP-900	wbLGP-858	2352	161857	two.sided	0.00e+00	0.0000000	****
LGP-900	wbLGP-958	2352	177763	two.sided	0.00e+00	0.0000000	****
MMP-360	wbBNP-568	2352	153083	two.sided	0.00e+00	0.0000000	****
MMP-360	wbCABP-718	2352	137815	two.sided	0.00e+00	0.0000000	****
MMP-360	wbLGP-1058	2352	158332	two.sided	0.00e+00	0.0000000	****
MMP-360	wbLGP-1158	2352	185386	two.sided	0.00e+00	0.0000000	****
MMP-360	wbLGP-1258	2352	166968	two.sided	0.00e+00	0.0000000	****
MMP-360	wbLGP-1358	2352	219183	two.sided	0.00e+00	0.0000000	****
MMP-360	wbLGP-458	2352	137964	two.sided	0.00e+00	0.0000000	****
MMP-360	wbLGP-558	2352	138865	two.sided	0.00e+00	0.0000000	****

bioRxiv preprint doi: https://doi.org/10.1101/2021.05.06.442886; this version posted September 4, 2021. The copyright holder for this preprint (which was not certified by peer review) is the author/funder, who has granted bioRxiv a license to display the preprint in perpetuity. It is made available under aCC-BY-NC-ND 4.0 International license.

Table S7. Parcellation - Paired Wilcoxon signed rank test *(continued)*

group1	group2	n1	statistic	alternative	p	p.adj	p.adj.signif
MMP-360	wbLGP-658	2352	156009	two.sided	0.00e+00	0.0000000	****
MMP-360	wbLGP-758	2352	164978	two.sided	0.00e+00	0.0000000	****
MMP-360	wbLGP-858	2352	157870	two.sided	0.00e+00	0.0000000	****
MMP-360	wbLGP-958	2352	182605	two.sided	0.00e+00	0.0000000	****
wbBNP-568	wbCABP-718	2352	1639241	two.sided	0.00e+00	0.0000000	****
wbBNP-568	wbLGP-1058	2352	1547859	two.sided	0.00e+00	0.0000000	****
wbBNP-568	wbLGP-1158	2352	1533796	two.sided	0.00e+00	0.0000000	****
wbBNP-568	wbLGP-1258	2352	1447228	two.sided	0.00e+00	0.0000000	****
wbBNP-568	wbLGP-1358	2352	1650972	two.sided	0.00e+00	0.0000000	****
wbBNP-568	wbLGP-458	2352	1125170	two.sided	1.22e-05	0.0033672	**
wbBNP-568	wbLGP-558	2352	1098196	two.sided	2.40e-06	0.0006486	***
wbBNP-568	wbLGP-658	2352	1550059	two.sided	0.00e+00	0.0000000	****
wbBNP-568	wbLGP-758	2352	1595774	two.sided	0.00e+00	0.0000000	****
wbBNP-568	wbLGP-858	2352	1458694	two.sided	0.00e+00	0.0000000	****
wbBNP-568	wbLGP-958	2352	1661566	two.sided	0.00e+00	0.0000000	****
wbCABP-718	wbLGP-1058	2352	1166229	two.sided	8.90e-02	1.0000000	ns
wbCABP-718	wbLGP-1158	2352	1266087	two.sided	3.20e-01	1.0000000	ns
wbCABP-718	wbLGP-1258	2352	1176085	two.sided	5.60e-02	1.0000000	ns
wbCABP-718	wbLGP-1358	2352	1400531	two.sided	1.00e-07	0.0000293	****
wbCABP-718	wbLGP-458	2352	831718	two.sided	0.00e+00	0.0000000	****
wbCABP-718	wbLGP-558	2352	757451	two.sided	0.00e+00	0.0000000	****
wbCABP-718	wbLGP-658	2352	1045849	two.sided	0.00e+00	0.0000006	****
wbCABP-718	wbLGP-758	2352	1166760	two.sided	5.80e-02	1.0000000	ns
wbCABP-718	wbLGP-858	2352	1068928	two.sided	4.00e-07	0.0001190	***
wbCABP-718	wbLGP-958	2352	1278722	two.sided	8.60e-02	1.0000000	ns
wbLGP-1058	wbLGP-1158	2352	1310431	two.sided	1.00e-02	1.0000000	ns
wbLGP-1058	wbLGP-1258	2352	1068697	two.sided	1.00e-07	0.0000157	****
wbLGP-1058	wbLGP-1358	2352	1503855	two.sided	0.00e+00	0.0000000	****
wbLGP-1058	wbLGP-458	2352	921542	two.sided	0.00e+00	0.0000000	****
wbLGP-1058	wbLGP-558	2352	830108	two.sided	0.00e+00	0.0000000	****
wbLGP-1058	wbLGP-658	2352	1070610	two.sided	3.00e-07	0.0000944	****
wbLGP-1058	wbLGP-758	2352	1177300	two.sided	2.97e-01	1.0000000	ns
wbLGP-1058	wbLGP-858	2352	975194	two.sided	0.00e+00	0.0000000	****
wbLGP-1058	wbLGP-958	2352	1341281	two.sided	5.59e-05	0.0154284	*
wbLGP-1158	wbLGP-1258	2352	1053122	two.sided	0.00e+00	0.0000005	****
wbLGP-1158	wbLGP-1358	2352	1451123	two.sided	0.00e+00	0.0000000	****
wbLGP-1158	wbLGP-458	2352	908290	two.sided	0.00e+00	0.0000000	****
wbLGP-1158	wbLGP-558	2352	892111	two.sided	0.00e+00	0.0000000	****
wbLGP-1158	wbLGP-658	2352	1078962	two.sided	3.00e-07	0.0000836	****
wbLGP-1158	wbLGP-758	2352	1178685	two.sided	1.16e-01	1.0000000	ns
wbLGP-1158	wbLGP-858	2352	1008073	two.sided	0.00e+00	0.0000000	****
wbLGP-1158	wbLGP-958	2352	1295606	two.sided	3.40e-02	1.0000000	ns

bioRxiv preprint doi: https://doi.org/10.1101/2021.05.06.442886; this version posted September 4, 2021. The copyright holder for this preprint (which was not certified by peer review) is the author/funder, who has granted bioRxiv a license to display the preprint in perpetuity. It is made available under aCC-BY-NC-ND 4.0 International license.

Table S7. Parcellation - Paired Wilcoxon signed rank test *(continued)*

group1	group2	n1	statistic	alternative	p	p.adj	p.adj.signif
wbLGP-1258	wbLGP-1358	2352	1612256	two.sided	0.00e+00	0.0000000	****
wbLGP-1258	wbLGP-458	2352	994969	two.sided	0.00e+00	0.0000000	****
wbLGP-1258	wbLGP-558	2352	957447	two.sided	0.00e+00	0.0000000	****
wbLGP-1258	wbLGP-658	2352	1172824	two.sided	4.40e-02	1.0000000	ns
wbLGP-1258	wbLGP-758	2352	1273752	two.sided	1.74e-01	1.0000000	ns
wbLGP-1258	wbLGP-858	2352	1150313	two.sided	8.00e-03	1.0000000	ns
wbLGP-1258	wbLGP-958	2352	1390511	two.sided	1.00e-07	0.0000197	****
wbLGP-1358	wbLGP-458	2352	824258	two.sided	0.00e+00	0.0000000	****
wbLGP-1358	wbLGP-558	2352	808992	two.sided	0.00e+00	0.0000000	****
wbLGP-1358	wbLGP-658	2352	968209	two.sided	0.00e+00	0.0000000	****
wbLGP-1358	wbLGP-758	2352	1031212	two.sided	0.00e+00	0.0000000	****
wbLGP-1358	wbLGP-858	2352	936260	two.sided	0.00e+00	0.0000000	****
wbLGP-1358	wbLGP-958	2352	1134304	two.sided	6.89e-04	0.1901640	ns
wbLGP-458	wbLGP-558	2352	1264741	two.sided	5.63e-01	1.0000000	ns
wbLGP-458	wbLGP-658	2352	1598752	two.sided	0.00e+00	0.0000000	****
wbLGP-458	wbLGP-758	2352	1629670	two.sided	0.00e+00	0.0000000	****
wbLGP-458	wbLGP-858	2352	1517308	two.sided	0.00e+00	0.0000000	****
wbLGP-458	wbLGP-958	2352	1684990	two.sided	0.00e+00	0.0000000	****
wbLGP-558	wbLGP-658	2352	1702013	two.sided	0.00e+00	0.0000000	****
wbLGP-558	wbLGP-758	2352	1693929	two.sided	0.00e+00	0.0000000	****
wbLGP-558	wbLGP-858	2352	1557712	two.sided	0.00e+00	0.0000000	****
wbLGP-558	wbLGP-958	2352	1716972	two.sided	0.00e+00	0.0000000	****
wbLGP-658	wbLGP-758	2352	1388101	two.sided	0.00e+00	0.0000049	****
wbLGP-658	wbLGP-858	2352	1241424	two.sided	5.82e-01	1.0000000	ns
wbLGP-658	wbLGP-958	2352	1515613	two.sided	0.00e+00	0.0000000	****
wbLGP-758	wbLGP-858	2352	970045	two.sided	0.00e+00	0.0000000	****
wbLGP-758	wbLGP-958	2352	1351987	two.sided	3.70e-06	0.0010295	**
wbLGP-858	wbLGP-958	2352	1494529	two.sided	0.00e+00	0.0000000	****

bioRxiv preprint doi: https://doi.org/10.1101/2021.05.06.442886; this version posted September 4, 2021. The copyright holder for this preprint (which was not certified by peer review) is the author/funder, who has granted bioRxiv a license to display the preprint in perpetuity. It is made available under aCC-BY-NC-ND 4.0 International license.

1.9 Significance Map

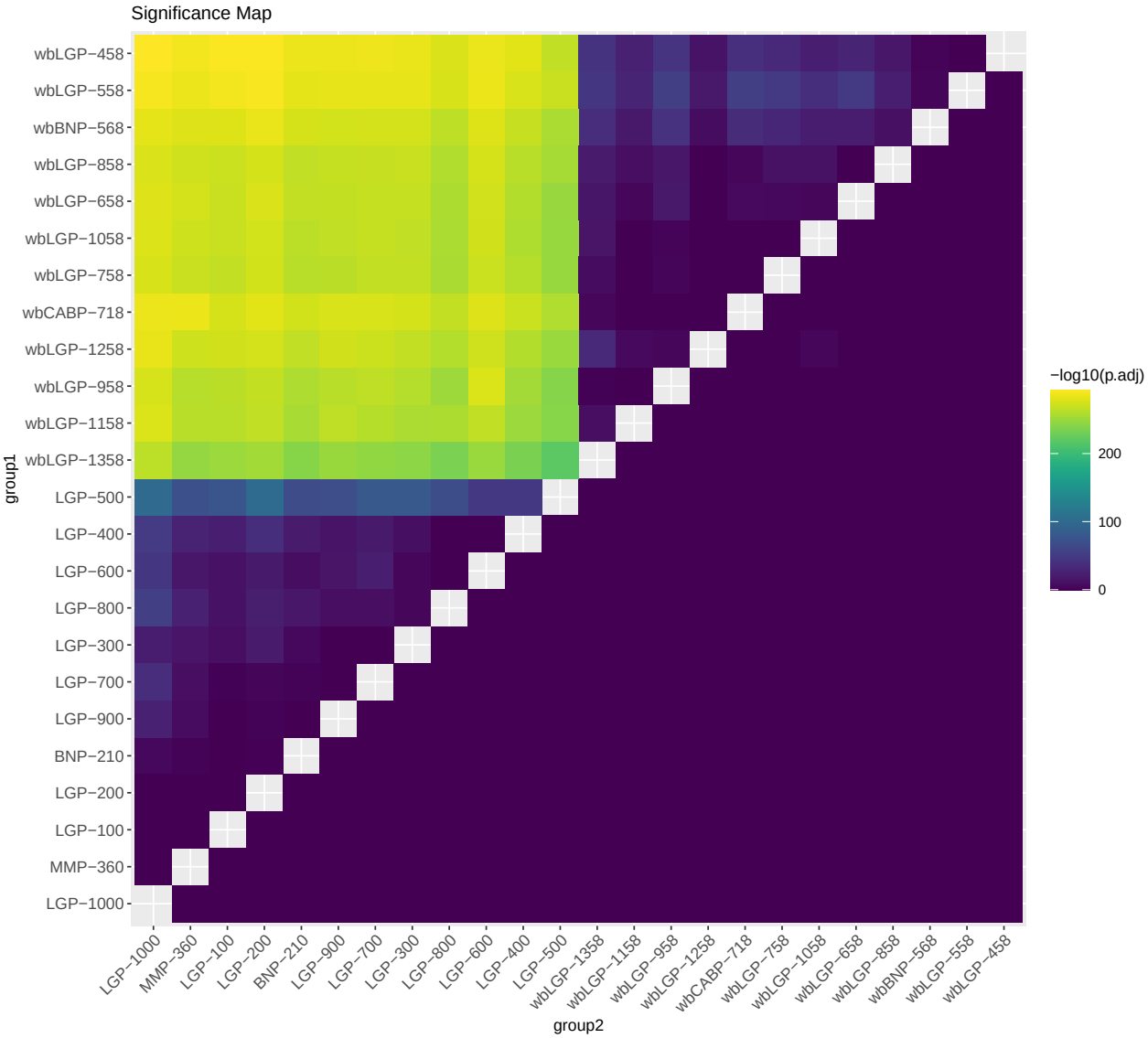

Fig. S4. Parcellation - Significance Map

1.10 Effect size

Table S8. Parcellation - Effect size

group1	group2	effsize	n1	n2	magnitude
BNP-210	LGP-100	0.0512884	2352	2352	small
BNP-210	LGP-1000	0.1207652	2352	2352	small
BNP-210	LGP-200	0.0626895	2352	2352	small
BNP-210	LGP-300	0.1141191	2352	2352	small
BNP-210	LGP-400	0.2082967	2352	2352	small
BNP-210	LGP-500	0.3653563	2352	2352	moderate
BNP-210	LGP-600	0.1408717	2352	2352	small

bioRxiv preprint doi: https://doi.org/10.1101/2021.05.06.442886; this version posted September 4, 2021. The copyright holder for this preprint (which was not certified by peer review) is the author/funder, who has granted bioRxiv a license to display the preprint in perpetuity. It is made available under aCC-BY-NC-ND 4.0 International license.

Table S8. Parcellation - Effect size *(continued)*

group1	group2	effsize	n1	n2	magnitude
BNP-210	LGP-700	0.0779897	2352	2352	small
BNP-210	LGP-800	0.1893357	2352	2352	small
BNP-210	LGP-900	0.0543280	2352	2352	small
BNP-210	MMP-360	0.0731563	2352	2352	small
BNP-210	wbBNP-568	0.7389896	2352	2352	large
BNP-210	wbCABP-718	0.7379236	2352	2352	large
BNP-210	wbLGP-1058	0.7216681	2352	2352	large
BNP-210	wbLGP-1158	0.7104950	2352	2352	large
BNP-210	wbLGP-1258	0.7231289	2352	2352	large
BNP-210	wbLGP-1358	0.6888160	2352	2352	large
BNP-210	wbLGP-458	0.7536559	2352	2352	large
BNP-210	wbLGP-558	0.7475750	2352	2352	large
BNP-210	wbLGP-658	0.7266246	2352	2352	large
BNP-210	wbLGP-758	0.7214303	2352	2352	large
BNP-210	wbLGP-858	0.7258208	2352	2352	large
BNP-210	wbLGP-958	0.7141604	2352	2352	large
LGP-100	LGP-1000	0.0539583	2352	2352	small
LGP-100	LGP-200	0.0129528	2352	2352	small
LGP-100	LGP-300	0.1500861	2352	2352	small
LGP-100	LGP-400	0.2208211	2352	2352	small
LGP-100	LGP-500	0.3913895	2352	2352	moderate
LGP-100	LGP-600	0.1695900	2352	2352	small
LGP-100	LGP-700	0.0698175	2352	2352	small
LGP-100	LGP-800	0.1689070	2352	2352	small
LGP-100	LGP-900	0.0495689	2352	2352	small
LGP-100	MMP-360	0.0317933	2352	2352	small
LGP-100	wbBNP-568	0.7436624	2352	2352	large
LGP-100	wbCABP-718	0.7394118	2352	2352	large
LGP-100	wbLGP-1058	0.7296547	2352	2352	large
LGP-100	wbLGP-1158	0.7220587	2352	2352	large
LGP-100	wbLGP-1258	0.7355677	2352	2352	large
LGP-100	wbLGP-1358	0.7044764	2352	2352	large
LGP-100	wbLGP-458	0.7640762	2352	2352	large
LGP-100	wbLGP-558	0.7569985	2352	2352	large
LGP-100	wbLGP-658	0.7310191	2352	2352	large
LGP-100	wbLGP-758	0.7275245	2352	2352	large
LGP-100	wbLGP-858	0.7326421	2352	2352	large
LGP-100	wbLGP-958	0.7209303	2352	2352	large
LGP-1000	LGP-200	0.0578365	2352	2352	small
LGP-1000	LGP-300	0.2105271	2352	2352	small
LGP-1000	LGP-400	0.3192842	2352	2352	moderate
LGP-1000	LGP-500	0.4487333	2352	2352	moderate
LGP-1000	LGP-600	0.3020832	2352	2352	moderate
LGP-1000	LGP-700	0.2719757	2352	2352	small
LGP-1000	LGP-800	0.3321805	2352	2352	moderate
LGP-1000	LGP-900	0.2340567	2352	2352	small
LGP-1000	MMP-360	0.0081145	2352	2352	small

bioRxiv preprint doi: https://doi.org/10.1101/2021.05.06.442886; this version posted September 4, 2021. The copyright holder for this preprint (which was not certified by peer review) is the author/funder, who has granted bioRxiv a license to display the preprint in perpetuity. It is made available under aCC-BY-NC-ND 4.0 International license.

Table S8. Parcellation - Effect size *(continued)*

group1	group2	effsize	n1	n2	magnitude
LGP-1000	wbBNP-568	0.7500285	2352	2352	large
LGP-1000	wbCABP-718	0.7568211	2352	2352	large
LGP-1000	wbLGP-1058	0.7435657	2352	2352	large
LGP-1000	wbLGP-1158	0.7443931	2352	2352	large
LGP-1000	wbLGP-1258	0.7509503	2352	2352	large
LGP-1000	wbLGP-1358	0.7255476	2352	2352	large
LGP-1000	wbLGP-458	0.7662544	2352	2352	large
LGP-1000	wbLGP-558	0.7623347	2352	2352	large
LGP-1000	wbLGP-658	0.7456084	2352	2352	large
LGP-1000	wbLGP-758	0.7432770	2352	2352	large
LGP-1000	wbLGP-858	0.7434569	2352	2352	large
LGP-1000	wbLGP-958	0.7395782	2352	2352	large
LGP-200	LGP-300	0.2081011	2352	2352	small
LGP-200	LGP-400	0.2759045	2352	2352	small
LGP-200	LGP-500	0.4511007	2352	2352	moderate
LGP-200	LGP-600	0.1986975	2352	2352	small
LGP-200	LGP-700	0.0956037	2352	2352	small
LGP-200	LGP-800	0.2215336	2352	2352	small
LGP-200	LGP-900	0.0807512	2352	2352	small
LGP-200	MMP-360	0.0232331	2352	2352	small
LGP-200	wbBNP-568	0.7524502	2352	2352	large
LGP-200	wbCABP-718	0.7494454	2352	2352	large
LGP-200	wbLGP-1058	0.7351284	2352	2352	large
LGP-200	wbLGP-1158	0.7272050	2352	2352	large
LGP-200	wbLGP-1258	0.7374204	2352	2352	large
LGP-200	wbLGP-1358	0.7088809	2352	2352	large
LGP-200	wbLGP-458	0.7639591	2352	2352	large
LGP-200	wbLGP-558	0.7610277	2352	2352	large
LGP-200	wbLGP-658	0.7432334	2352	2352	large
LGP-200	wbLGP-758	0.7366071	2352	2352	large
LGP-200	wbLGP-858	0.7386798	2352	2352	large
LGP-200	wbLGP-958	0.7282388	2352	2352	large
LGP-300	LGP-400	0.1569344	2352	2352	small
LGP-300	LGP-500	0.4014572	2352	2352	moderate
LGP-300	LGP-600	0.1086461	2352	2352	small
LGP-300	LGP-700	0.0305094	2352	2352	small
LGP-300	LGP-800	0.1105415	2352	2352	small
LGP-300	LGP-900	0.0588944	2352	2352	small
LGP-300	MMP-360	0.1802777	2352	2352	small
LGP-300	wbBNP-568	0.7393016	2352	2352	large
LGP-300	wbCABP-718	0.7409097	2352	2352	large
LGP-300	wbLGP-1058	0.7254031	2352	2352	large
LGP-300	wbLGP-1158	0.7146360	2352	2352	large
LGP-300	wbLGP-1258	0.7276375	2352	2352	large
LGP-300	wbLGP-1358	0.6950338	2352	2352	large
LGP-300	wbLGP-458	0.7545390	2352	2352	large

bioRxiv preprint doi: https://doi.org/10.1101/2021.05.06.442886; this version posted September 4, 2021. The copyright holder for this preprint (which was not certified by peer review) is the author/funder, who has granted bioRxiv a license to display the preprint in perpetuity. It is made available under aCC-BY-NC-ND 4.0 International license.

Table S8. Parcellation - Effect size *(continued)*

group1	group2	effsize	n1	n2	magnitude
LGP-300	wbLGP-558	0.7518696	2352	2352	large
LGP-300	wbLGP-658	0.7305186	2352	2352	large
LGP-300	wbLGP-758	0.7288353	2352	2352	large
LGP-300	wbLGP-858	0.7315947	2352	2352	large
LGP-300	wbLGP-958	0.7184744	2352	2352	large
LGP-400	LGP-500	0.3106815	2352	2352	moderate
LGP-400	LGP-600	0.0239758	2352	2352	small
LGP-400	LGP-700	0.2024827	2352	2352	small
LGP-400	LGP-800	0.0547714	2352	2352	small
LGP-400	LGP-900	0.1808123	2352	2352	small
LGP-400	MMP-360	0.2340978	2352	2352	small
LGP-400	wbBNP-568	0.7295883	2352	2352	large
LGP-400	wbCABP-718	0.7324939	2352	2352	large
LGP-400	wbLGP-1058	0.7127931	2352	2352	large
LGP-400	wbLGP-1158	0.7034513	2352	2352	large
LGP-400	wbLGP-1258	0.7163478	2352	2352	large
LGP-400	wbLGP-1358	0.6809360	2352	2352	large
LGP-400	wbLGP-458	0.7489080	2352	2352	large
LGP-400	wbLGP-558	0.7418199	2352	2352	large
LGP-400	wbLGP-658	0.7177687	2352	2352	large
LGP-400	wbLGP-758	0.7184835	2352	2352	large
LGP-400	wbLGP-858	0.7209195	2352	2352	large
LGP-400	wbLGP-958	0.7072074	2352	2352	large
LGP-500	LGP-600	0.3060236	2352	2352	moderate
LGP-500	LGP-700	0.4001344	2352	2352	moderate
LGP-500	LGP-800	0.3747741	2352	2352	moderate
LGP-500	LGP-900	0.3739231	2352	2352	moderate
LGP-500	MMP-360	0.3762905	2352	2352	moderate
LGP-500	wbBNP-568	0.7165713	2352	2352	large
LGP-500	wbCABP-718	0.7182115	2352	2352	large
LGP-500	wbLGP-1058	0.7002399	2352	2352	large
LGP-500	wbLGP-1158	0.6914885	2352	2352	large
LGP-500	wbLGP-1258	0.7026320	2352	2352	large
LGP-500	wbLGP-1358	0.6590763	2352	2352	large
LGP-500	wbLGP-458	0.7298496	2352	2352	large
LGP-500	wbLGP-558	0.7343705	2352	2352	large
LGP-500	wbLGP-658	0.7035363	2352	2352	large
LGP-500	wbLGP-758	0.7031792	2352	2352	large
LGP-500	wbLGP-858	0.7123423	2352	2352	large
LGP-500	wbLGP-958	0.6868862	2352	2352	large
LGP-600	LGP-700	0.2268428	2352	2352	small
LGP-600	LGP-800	0.0462445	2352	2352	small
LGP-600	LGP-900	0.1816469	2352	2352	small
LGP-600	MMP-360	0.1886473	2352	2352	small
LGP-600	wbBNP-568	0.7481082	2352	2352	large
LGP-600	wbCABP-718	0.7481815	2352	2352	large

bioRxiv preprint doi: https://doi.org/10.1101/2021.05.06.442886; this version posted September 4, 2021. The copyright holder for this preprint (which was not certified by peer review) is the author/funder, who has granted bioRxiv a license to display the preprint in perpetuity. It is made available under aCC-BY-NC-ND 4.0 International license.

Table S8. Parcellation - Effect size *(continued)*

group1	group2	effsize	n1	n2	magnitude
LGP-600	wbLGP-1058	0.7383695	2352	2352	large
LGP-600	wbLGP-1158	0.7294442	2352	2352	large
LGP-600	wbLGP-1258	0.7369489	2352	2352	large
LGP-600	wbLGP-1358	0.7042384	2352	2352	large
LGP-600	wbLGP-458	0.7557913	2352	2352	large
LGP-600	wbLGP-558	0.7562789	2352	2352	large
LGP-600	wbLGP-658	0.7398462	2352	2352	large
LGP-600	wbLGP-758	0.7355434	2352	2352	large
LGP-600	wbLGP-858	0.7421715	2352	2352	large
LGP-600	wbLGP-958	0.7452103	2352	2352	large
LGP-700	LGP-800	0.1482687	2352	2352	small
LGP-700	LGP-900	0.0223819	2352	2352	small
LGP-700	MMP-360	0.1459144	2352	2352	small
LGP-700	wbBNP-568	0.7385190	2352	2352	large
LGP-700	wbCABP-718	0.7428081	2352	2352	large
LGP-700	wbLGP-1058	0.7280828	2352	2352	large
LGP-700	wbLGP-1158	0.7198417	2352	2352	large
LGP-700	wbLGP-1258	0.7322622	2352	2352	large
LGP-700	wbLGP-1358	0.6979349	2352	2352	large
LGP-700	wbLGP-458	0.7555548	2352	2352	large
LGP-700	wbLGP-558	0.7506720	2352	2352	large
LGP-700	wbLGP-658	0.7296047	2352	2352	large
LGP-700	wbLGP-758	0.7284709	2352	2352	large
LGP-700	wbLGP-858	0.7297612	2352	2352	large
LGP-700	wbLGP-958	0.7241542	2352	2352	large
LGP-800	LGP-900	0.1523587	2352	2352	small
LGP-800	MMP-360	0.2294773	2352	2352	small
LGP-800	wbBNP-568	0.7247815	2352	2352	large
LGP-800	wbCABP-718	0.7278916	2352	2352	large
LGP-800	wbLGP-1058	0.7110976	2352	2352	large
LGP-800	wbLGP-1158	0.7148132	2352	2352	large
LGP-800	wbLGP-1258	0.7177082	2352	2352	large
LGP-800	wbLGP-1358	0.6815238	2352	2352	large
LGP-800	wbLGP-458	0.7424878	2352	2352	large
LGP-800	wbLGP-558	0.7403174	2352	2352	large
LGP-800	wbLGP-658	0.7160305	2352	2352	large
LGP-800	wbLGP-758	0.7131063	2352	2352	large
LGP-800	wbLGP-858	0.7184349	2352	2352	large
LGP-800	wbLGP-958	0.7032708	2352	2352	large
LGP-900	MMP-360	0.1404051	2352	2352	small
LGP-900	wbBNP-568	0.7387104	2352	2352	large
LGP-900	wbCABP-718	0.7433471	2352	2352	large
LGP-900	wbLGP-1058	0.7243857	2352	2352	large
LGP-900	wbLGP-1158	0.7255897	2352	2352	large
LGP-900	wbLGP-1258	0.7343608	2352	2352	large
LGP-900	wbLGP-1358	0.7026858	2352	2352	large
LGP-900	wbLGP-458	0.7545988	2352	2352	large

bioRxiv preprint doi: https://doi.org/10.1101/2021.05.06.442886; this version posted September 4, 2021. The copyright holder for this preprint (which was not certified by peer review) is the author/funder, who has granted bioRxiv a license to display the preprint in perpetuity. It is made available under aCC-BY-NC-ND 4.0 International license.

Table S8. Parcellation - Effect size *(continued)*

group1	group2	effsize	n1	n2	magnitude
LGP-900	wbLGP-558	0.7503933	2352	2352	large
LGP-900	wbLGP-658	0.7302955	2352	2352	large
LGP-900	wbLGP-758	0.7241196	2352	2352	large
LGP-900	wbLGP-858	0.7301608	2352	2352	large
LGP-900	wbLGP-958	0.7201412	2352	2352	large
MMP-360	wbBNP-568	0.7444282	2352	2352	large
MMP-360	wbCABP-718	0.7535082	2352	2352	large
MMP-360	wbLGP-1058	0.7311101	2352	2352	large
MMP-360	wbLGP-1158	0.7201675	2352	2352	large
MMP-360	wbLGP-1258	0.7319867	2352	2352	large
MMP-360	wbLGP-1358	0.6975871	2352	2352	large
MMP-360	wbLGP-458	0.7584484	2352	2352	large
MMP-360	wbLGP-558	0.7548697	2352	2352	large
MMP-360	wbLGP-658	0.7382470	2352	2352	large
MMP-360	wbLGP-758	0.7320983	2352	2352	large
MMP-360	wbLGP-858	0.7345617	2352	2352	large
MMP-360	wbLGP-958	0.7174438	2352	2352	large
wbBNP-568	wbCABP-718	0.2728574	2352	2352	small
wbBNP-568	wbLGP-1058	0.2162613	2352	2352	small
wbBNP-568	wbLGP-1158	0.1995484	2352	2352	small
wbBNP-568	wbLGP-1258	0.1386707	2352	2352	small
wbBNP-568	wbLGP-1358	0.2717290	2352	2352	small
wbBNP-568	wbLGP-458	0.0877119	2352	2352	small
wbBNP-568	wbLGP-558	0.0947171	2352	2352	small
wbBNP-568	wbLGP-658	0.2160494	2352	2352	small
wbBNP-568	wbLGP-758	0.2540569	2352	2352	small
wbBNP-568	wbLGP-858	0.1592633	2352	2352	small
wbBNP-568	wbLGP-958	0.2937065	2352	2352	small
wbCABP-718	wbLGP-1058	0.0359091	2352	2352	small
wbCABP-718	wbLGP-1158	0.0233259	2352	2352	small
wbCABP-718	wbLGP-1258	0.0388589	2352	2352	small
wbCABP-718	wbLGP-1358	0.1106258	2352	2352	small
wbCABP-718	wbLGP-458	0.2848362	2352	2352	small
wbCABP-718	wbLGP-558	0.3284945	2352	2352	moderate
wbCABP-718	wbLGP-658	0.1230697	2352	2352	small
wbCABP-718	wbLGP-758	0.0370190	2352	2352	small
wbCABP-718	wbLGP-858	0.0991309	2352	2352	small
wbCABP-718	wbLGP-958	0.0362152	2352	2352	small
wbLGP-1058	wbLGP-1158	0.0561301	2352	2352	small
wbLGP-1058	wbLGP-1258	0.1116554	2352	2352	small
wbLGP-1058	wbLGP-1358	0.1822538	2352	2352	small
wbLGP-1058	wbLGP-458	0.2180510	2352	2352	small
wbLGP-1058	wbLGP-558	0.2778507	2352	2352	small
wbLGP-1058	wbLGP-658	0.1051919	2352	2352	small
wbLGP-1058	wbLGP-758	0.0228152	2352	2352	small
wbLGP-1058	wbLGP-858	0.1661968	2352	2352	small
wbLGP-1058	wbLGP-958	0.0818575	2352	2352	small

bioRxiv preprint doi: https://doi.org/10.1101/2021.05.06.442886; this version posted September 4, 2021. The copyright holder for this preprint (which was not certified by peer review) is the author/funder, who has granted bioRxiv a license to display the preprint in perpetuity. It is made available under aCC-BY-NC-ND 4.0 International license.

Table S8. Parcellation - Effect size *(continued)*

group1	group2	effsize	n1	n2	magnitude
wbLGP-1158	wbLGP-1258	0.1252645	2352	2352	small
wbLGP-1158	wbLGP-1358	0.1480026	2352	2352	small
wbLGP-1158	wbLGP-458	0.2274392	2352	2352	small
wbLGP-1158	wbLGP-558	0.2439547	2352	2352	small
wbLGP-1158	wbLGP-658	0.1045024	2352	2352	small
wbLGP-1158	wbLGP-758	0.0322159	2352	2352	small
wbLGP-1158	wbLGP-858	0.1551948	2352	2352	small
wbLGP-1158	wbLGP-958	0.0414800	2352	2352	small
wbLGP-1258	wbLGP-1358	0.2590570	2352	2352	small
wbLGP-1258	wbLGP-458	0.1735670	2352	2352	small
wbLGP-1258	wbLGP-558	0.1977710	2352	2352	small
wbLGP-1258	wbLGP-658	0.0419666	2352	2352	small
wbLGP-1258	wbLGP-758	0.0287042	2352	2352	small
wbLGP-1258	wbLGP-858	0.0559503	2352	2352	small
wbLGP-1258	wbLGP-958	0.1063742	2352	2352	small
wbLGP-1358	wbLGP-458	0.2918365	2352	2352	small
wbLGP-1358	wbLGP-558	0.3015406	2352	2352	moderate
wbLGP-1358	wbLGP-658	0.1847120	2352	2352	small
wbLGP-1358	wbLGP-758	0.1378691	2352	2352	small
wbLGP-1358	wbLGP-858	0.2044047	2352	2352	small
wbLGP-1358	wbLGP-958	0.0714880	2352	2352	small
wbLGP-458	wbLGP-558	0.0115092	2352	2352	small
wbLGP-458	wbLGP-658	0.2420159	2352	2352	small
wbLGP-458	wbLGP-758	0.2603953	2352	2352	small
wbLGP-458	wbLGP-858	0.1864424	2352	2352	small
wbLGP-458	wbLGP-958	0.2951134	2352	2352	small
wbLGP-558	wbLGP-658	0.3159288	2352	2352	moderate
wbLGP-558	wbLGP-758	0.3114833	2352	2352	moderate
wbLGP-558	wbLGP-858	0.2210771	2352	2352	small
wbLGP-558	wbLGP-958	0.3280744	2352	2352	moderate
wbLGP-658	wbLGP-758	0.1151963	2352	2352	small
wbLGP-658	wbLGP-858	0.0129152	2352	2352	small
wbLGP-658	wbLGP-958	0.1975321	2352	2352	small
wbLGP-758	wbLGP-858	0.1643324	2352	2352	small
wbLGP-758	wbLGP-958	0.0960455	2352	2352	small
wbLGP-858	wbLGP-958	0.1928274	2352	2352	small

bioRxiv preprint doi: https://doi.org/10.1101/2021.05.06.442886; this version posted September 4, 2021. The copyright holder for this preprint (which was not certified by peer review) is the author/funder, who has granted bioRxiv a license to display the preprint in perpetuity. It is made available under aCC-BY-NC-ND 4.0 International license.

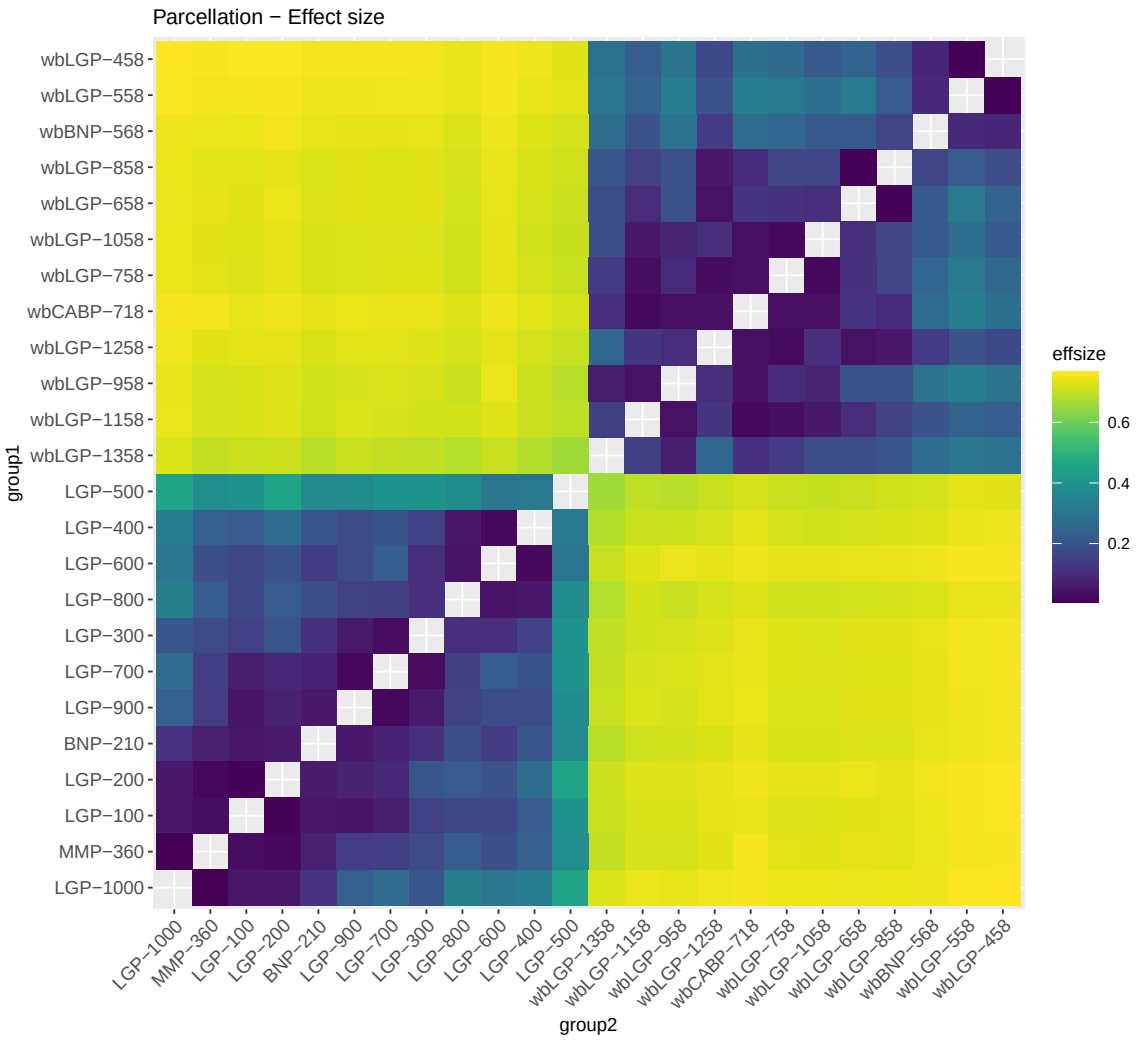

Fig. S5. Parcellation - Effect size

1.11 Variability Changes

Whole Brain vs. Cortex

- Quadrant 1: $V_w \uparrow, V_b \uparrow$: 0.0093684
- Quadrant 2: $V_w \downarrow, V_b \uparrow$: 0.5999534
- Quadrant 3: $V_w \downarrow, V_b \downarrow$: 0.3906782
- Quadrant 4: $V_w \uparrow, V_b \downarrow$: 0

bioRxiv preprint doi: https://doi.org/10.1101/2021.05.06.442886; this version posted September 4, 2021. The copyright holder for this preprint (which was not certified by peer review) is the author/funder, who has granted bioRxiv a license to display the preprint in perpetuity. It is made available under aCC-BY-NC-ND 4.0 International license.

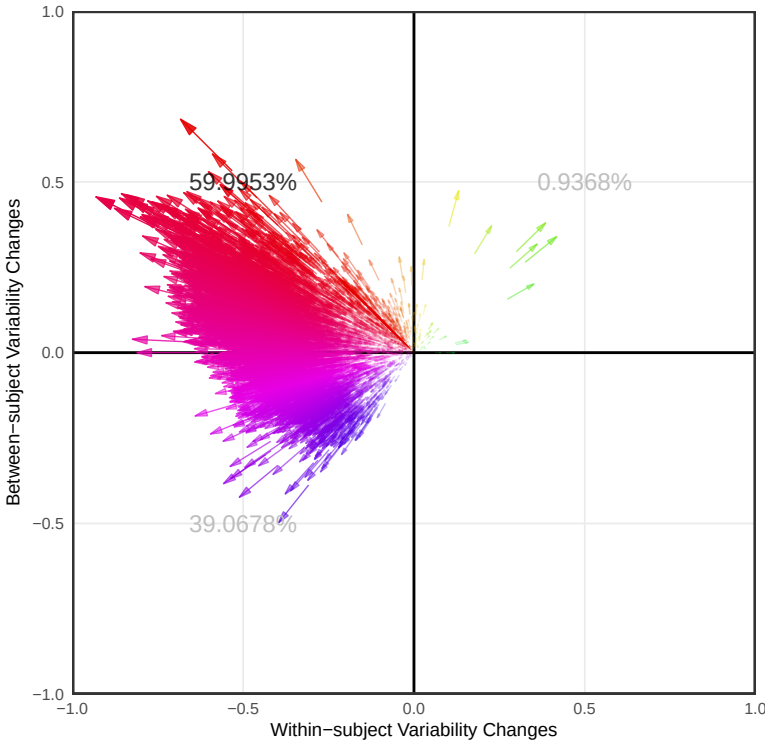

Fig. S6. Parcellation - Variability Changes

bioRxiv preprint doi: https://doi.org/10.1101/2021.05.06.442886; this version posted September 4, 2021. The copyright holder for this preprint (which was not certified by peer review) is the author/funder, who has granted bioRxiv a license to display the preprint in perpetuity. It is made available under aCC-BY-NC-ND 4.0 International license.

2 Frequency Bands - Edge Construction

2.1 ICC Density distribution

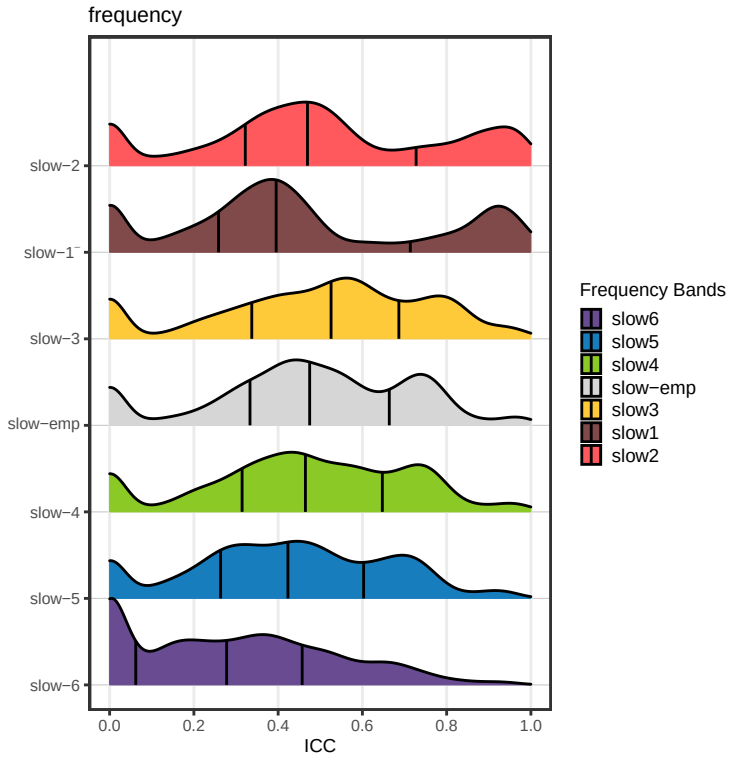

Fig. S7. Frequency - ICC Density distribution

2.2 Almost Perfect (ICCs > 0.8)

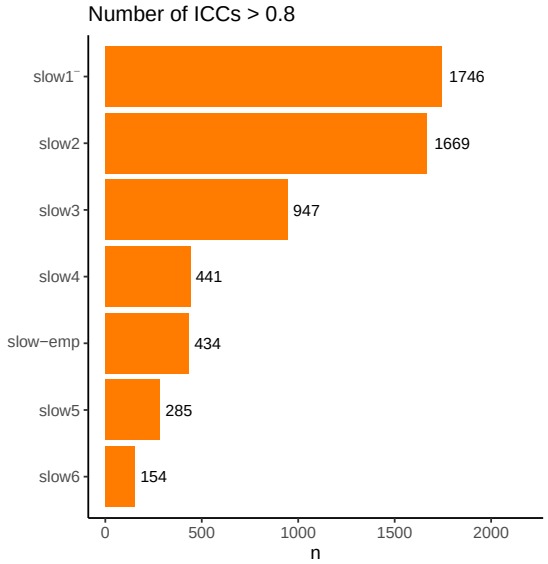

Fig. S8. Frequency - Number of ICC >0.8

bioRxiv preprint doi: https://doi.org/10.1101/2021.05.06.442886; this version posted September 4, 2021. The copyright holder for this preprint (which was not certified by peer review) is the author/funder, who has granted bioRxiv a license to display the preprint in perpetuity. It is made available under aCC-BY-NC-ND 4.0 International license.

2.3 Substantial or Above (ICCs > 0.6)

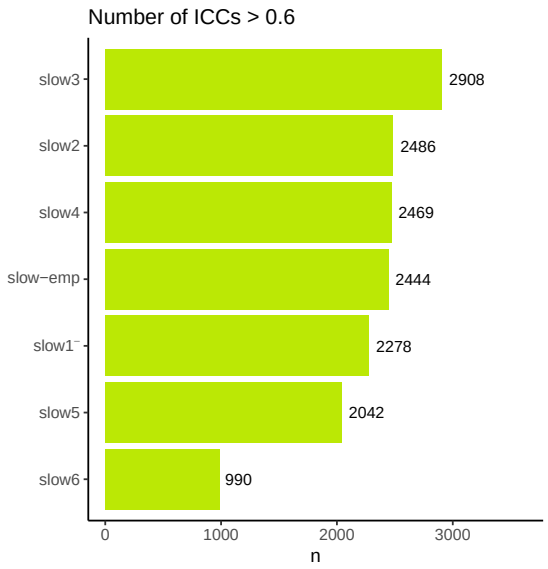

Fig. S9. Frequency - Number of ICC >0.6

bioRxiv preprint doi: https://doi.org/10.1101/2021.05.06.442886; this version posted September 4, 2021. The copyright holder for this preprint (which was not certified by peer review) is the author/funder, who has granted bioRxiv a license to display the preprint in perpetuity. It is made available under aCC-BY-NC-ND 4.0 International license.

2.4 Variability Changes

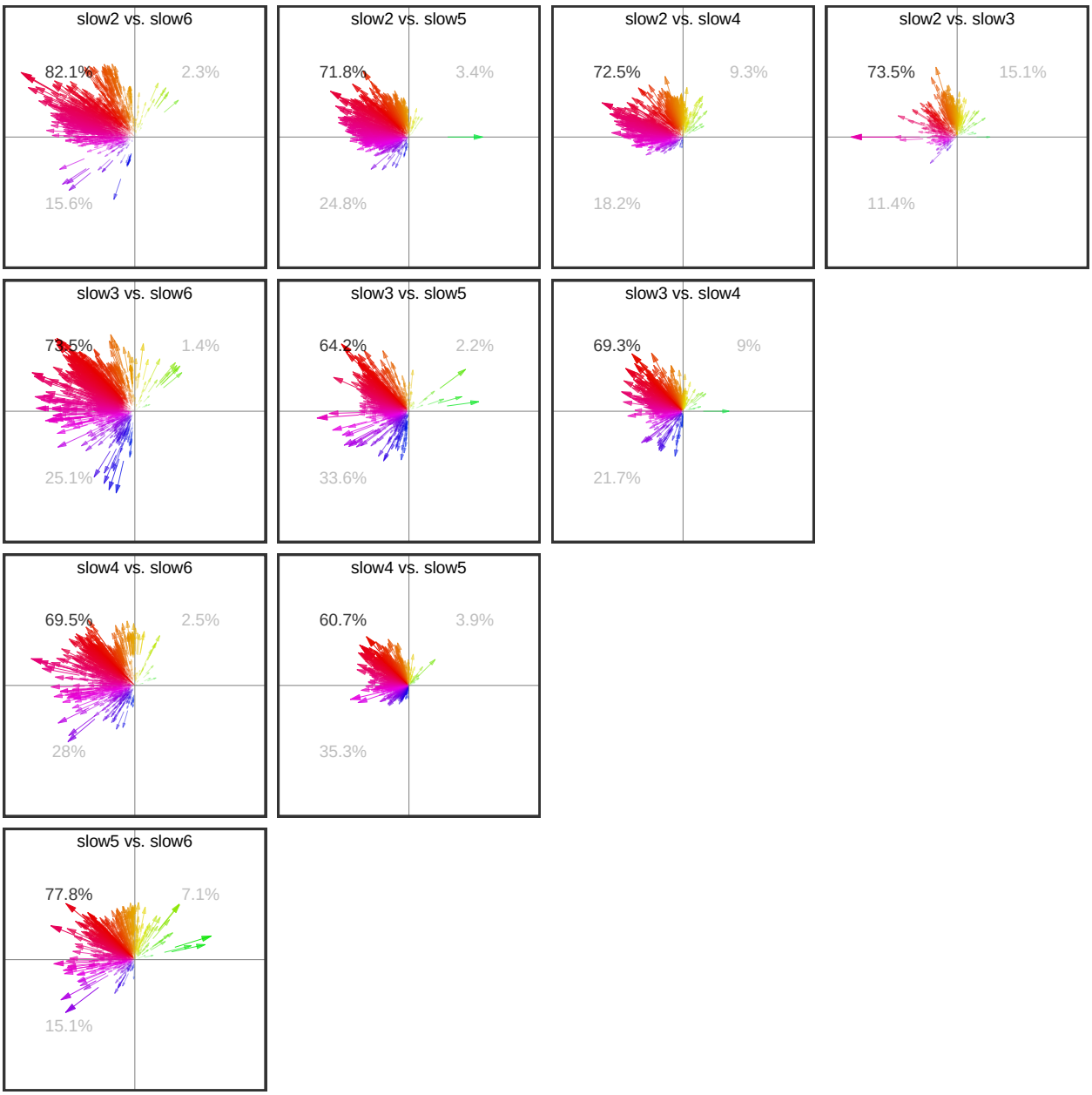

Fig. S10. Frequency - Variability Changes

bioRxiv preprint doi: https://doi.org/10.1101/2021.05.06.442886; this version posted September 4, 2021. The copyright holder for this preprint (which was not certified by peer review) is the author/funder, who has granted bioRxiv a license to display the preprint in perpetuity. It is made available under aCC-BY-NC-ND 4.0 International license.

2.5 Descriptive statistics Mean

Table S9. Frequency - ICC Mean

freq	variable	n	mean	mean_z2r
slow2	ICC.z	8064	0.689	0.5973392
slow1	ICC.z	8064	0.638	0.5635362
slow3	ICC.z	8064	0.621	0.5518239
slow-emp	ICC.z	8064	0.575	0.5190218
slow4	ICC.z	8064	0.560	0.5079774
slow5	ICC.z	8064	0.494	0.4573854
slow6	ICC.z	8064	0.331	0.3194190

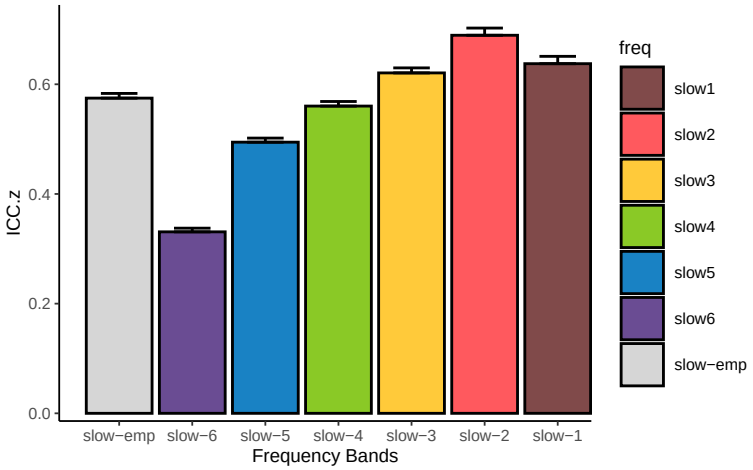

Fig. S11. Frequency - ICC Mean Bar plot

2.6 Descriptive statistics Median

Table S10. Frequency - ICC Median

freq	variable	n	median
slow3	ICC	8064	0.526
slow-emp	ICC	8064	0.475
slow2	ICC	8064	0.470
slow4	ICC	8064	0.465
slow5	ICC	8064	0.423
slow1	ICC	8064	0.395
slow6	ICC	8064	0.278

bioRxiv preprint doi: https://doi.org/10.1101/2021.05.06.442886; this version posted September 4, 2021. The copyright holder for this preprint (which was not certified by peer review) is the author/funder, who has granted bioRxiv a license to display the preprint in perpetuity. It is made available under aCC-BY-NC-ND 4.0 International license.

2.7 Friedman Test

Table S11. Frequency - Friedman Test

.y.	n	statistic	df	p	method
ICC.z	8064	9283.536	6	0	Friedman test

2.8 Friedman Test Effect size

Table S12. Frequency - Friedman Test Effect size

.y.	n	effsize	method	magnitude
ICC.z	8064	0.191872	Kendall W	small

2.9 Paired Wilcoxon signed rank test

Table S13. Frequency - ICC group1 vs. group2

group1	group2	n1	estimate	statistic	alternative	p	p.adj	p.adj.signif
slow-emp	slow1	8064	-0.0162227	14054394	two.sided	9.68e-04	0.0203280	*
slow-emp	slow2	8064	-0.0864131	10505882	two.sided	0.00e+00	0.0000000	****
slow-emp	slow3	8064	-0.0539695	10625450	two.sided	0.00e+00	0.0000000	****
slow-emp	slow4	8064	0.0150546	17102898	two.sided	0.00e+00	0.0000000	****
slow-emp	slow5	8064	0.0841908	23531772	two.sided	0.00e+00	0.0000000	****
slow-emp	slow6	8064	0.2231625	26254891	two.sided	0.00e+00	0.0000000	****
slow1	slow2	8064	-0.0624239	9900068	two.sided	0.00e+00	0.0000000	****
slow1	slow3	8064	-0.0200081	13838087	two.sided	8.77e-05	0.0018417	**
slow1	slow4	8064	0.0325830	15946425	two.sided	0.00e+00	0.0000000	****
slow1	slow5	8064	0.1039074	18945816	two.sided	0.00e+00	0.0000000	****
slow1	slow6	8064	0.2451552	23735075	two.sided	0.00e+00	0.0000000	****
slow2	slow3	8064	0.0367993	16494499	two.sided	0.00e+00	0.0000000	****
slow2	slow4	8064	0.1038401	19454026	two.sided	0.00e+00	0.0000000	****
slow2	slow5	8064	0.1643515	22530367	two.sided	0.00e+00	0.0000000	****
slow2	slow6	8064	0.2906672	25875758	two.sided	0.00e+00	0.0000000	****
slow3	slow4	8064	0.0703217	20070190	two.sided	0.00e+00	0.0000000	****
slow3	slow5	8064	0.1355815	23423580	two.sided	0.00e+00	0.0000000	****
slow3	slow6	8064	0.2698008	26652991	two.sided	0.00e+00	0.0000000	****
slow4	slow5	8064	0.0707338	21276606	two.sided	0.00e+00	0.0000000	****
slow4	slow6	8064	0.2083264	25815007	two.sided	0.00e+00	0.0000000	****
slow5	slow6	8064	0.1410985	24873960	two.sided	0.00e+00	0.0000000	****

bioRxiv preprint doi: https://doi.org/10.1101/2021.05.06.442886; this version posted September 4, 2021. The copyright holder for this preprint (which was not certified by peer review) is the author/funder, who has granted bioRxiv a license to display the preprint in perpetuity. It is made available under aCC-BY-NC-ND 4.0 International license.

2.10 Significance Map

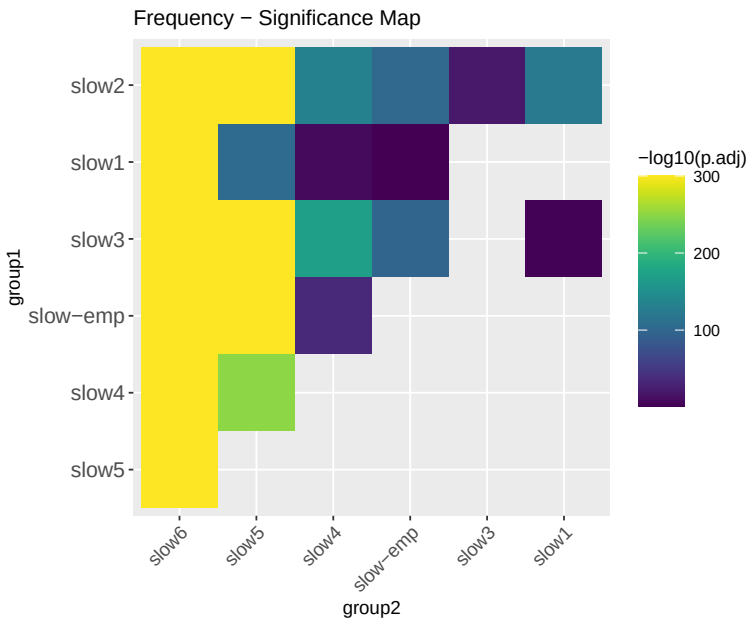

Fig. S12. Frequency - Significance Map

2.11 Effect size

Table S14. Frequency - Effect size

group1	group2	effsize	n1	n2	magnitude
slow-emp	slow1	0.0296722	8064	8064	small
slow-emp	slow2	0.2374189	8064	8064	small
slow-emp	slow3	0.2357191	8064	8064	small
slow-emp	slow4	0.1417849	8064	8064	small
slow-emp	slow5	0.5094890	8064	8064	large
slow-emp	slow6	0.6519342	8064	8064	large
slow1	slow2	0.2699083	8064	8064	small
slow1	slow3	0.0520287	8064	8064	small
slow1	slow4	0.0646878	8064	8064	small
slow1	slow5	0.2408327	8064	8064	small
slow1	slow6	0.5023808	8064	8064	large
slow2	slow3	0.1000050	8064	8064	small
slow2	slow4	0.2699834	8064	8064	small
slow2	slow5	0.4490800	8064	8064	moderate
slow2	slow6	0.6292308	8064	8064	large
slow3	slow4	0.3096116	8064	8064	moderate
slow3	slow5	0.5028784	8064	8064	large
slow3	slow6	0.6802808	8064	8064	large
slow4	slow5	0.3770518	8064	8064	moderate
slow4	slow6	0.6310338	8064	8064	large

bioRxiv preprint doi: https://doi.org/10.1101/2021.05.06.442886; this version posted September 4, 2021. The copyright holder for this preprint (which was not certified by peer review) is the author/funder, who has granted bioRxiv a license to display the preprint in perpetuity. It is made available under aCC-BY-NC-ND 4.0 International license.

Table S14. Frequency - Effect size *(continued)*

group1	group2	effsize	n1	n2	magnitude
slow5	slow6	0.5700624	8064	8064	large

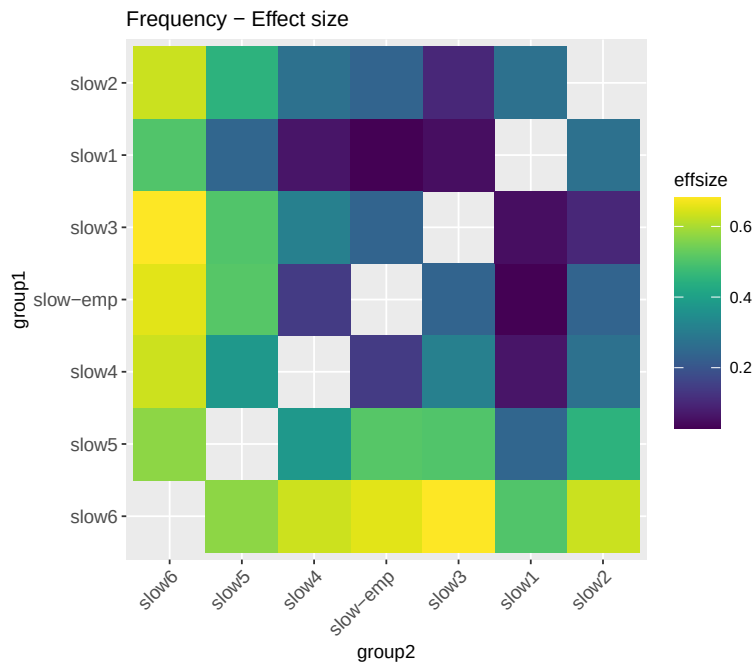

Fig. S13. Frequency - Effect size

3 R Tranforms - Edge Construction

Many network metrics are not well defined for negatively weighted connections. In order to ensure that the connection weights are positive only, we applied four types of transformations to the symmetric correlation matrix: the **positive** (Eq.pos), **absolute** (Eq.abs), **exponential** (Eq.exp) and **distance-inverse** (Eq.div) functions, respectively. This avoids the negative values in the inter-node connectivity matrix $W = (w_{ij})$ where $z_{ij} = \tanh^{-1}(r_{ij})$ is Fisher's $z-$transformation.

$$w_{ij} = \frac{z_{ij} + |z_{ij}|}{2} \in [0, \infty) \tag{pos}$$

$$w_{ij} = |z_{ij}| \in [0, \infty) \tag{abs}$$

$$w_{ij} = \mathrm{e}^{z_{ij}} \in [0, \infty) \tag{exp}$$

$$w_{ij} = \frac{2}{\sqrt{2 \times (1 - r_{ij})}} \in (0, \infty) \tag{div}$$

bioRxiv preprint doi: https://doi.org/10.1101/2021.05.06.442886; this version posted September 4, 2021. The copyright holder for this preprint (which was not certified by peer review) is the author/funder, who has granted bioRxiv a license to display the preprint in perpetuity. It is made available under aCC-BY-NC-ND 4.0 International license.

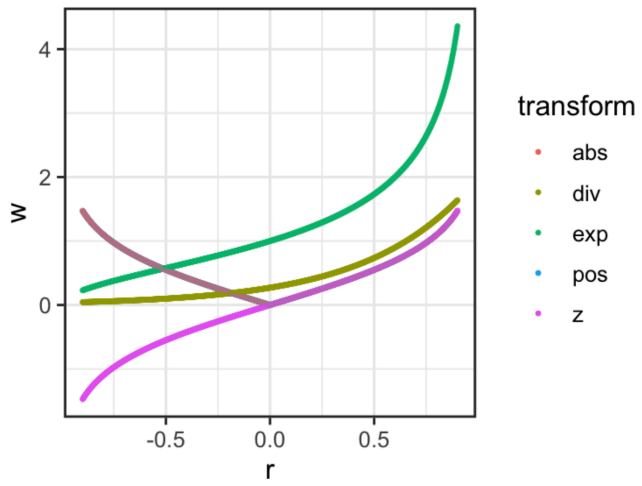

Fig. S14. Transform r to weight

3.1 ICC Density distribution

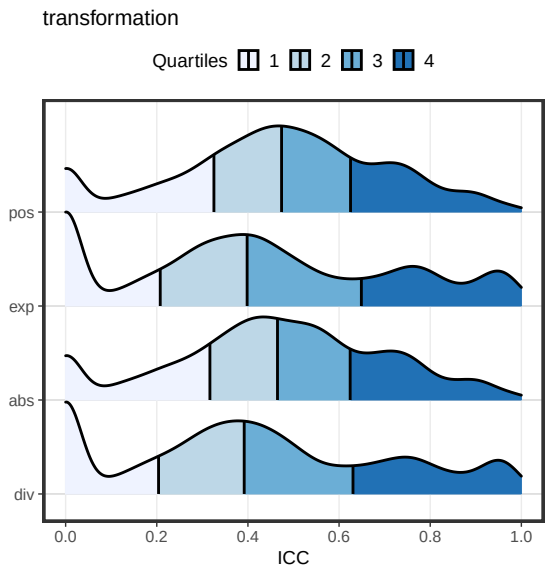

Fig. S15. Transforms - ICC Density distribution

3.2 Almost Perfect (ICCs > 0.8)

Table S15. Transforms - Number of ICCs > 0.8

transform	n
exp	1855
div	1740
abs	1050
pos	1031

bioRxiv preprint doi: https://doi.org/10.1101/2021.05.06.442886; this version posted September 4, 2021. The copyright holder for this preprint (which was not certified by peer review) is the author/funder, who has granted bioRxiv a license to display the preprint in perpetuity. It is made available under aCC-BY-NC-ND 4.0 International license.

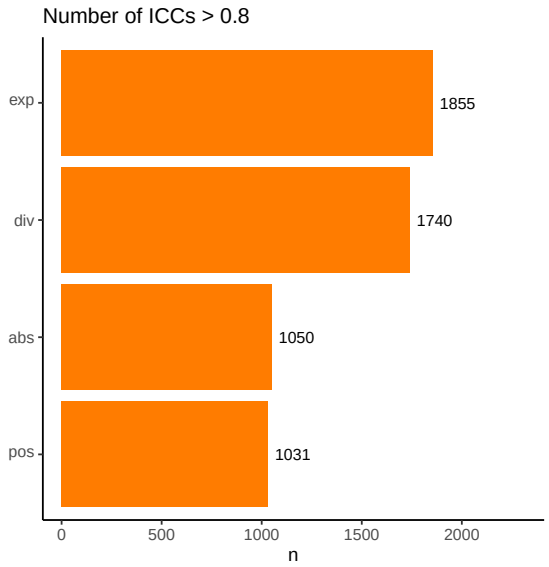

Fig. S16. Transforms - Number of ICC > 0.8

3.3 Substantial or Above (ICCs > 0.6)

Table S16. Transforms - Number of ICCs > 0.6

transform	n
pos	3977
exp	3930
abs	3912
div	3798

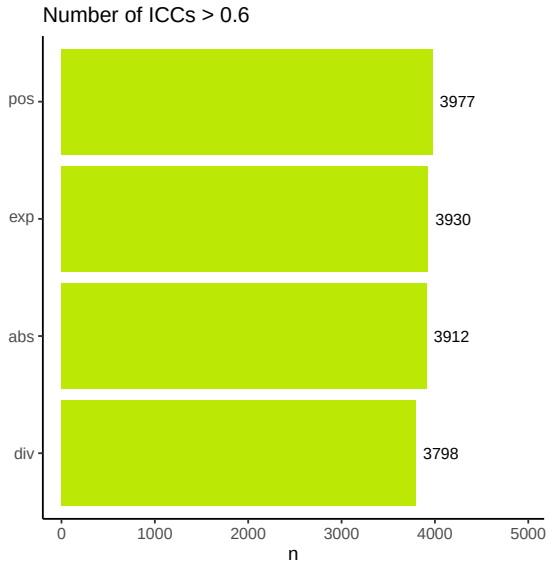

Fig. S17. Transforms - Number of ICC > 0.8

bioRxiv preprint doi: https://doi.org/10.1101/2021.05.06.442886; this version posted September 4, 2021. The copyright holder for this preprint (which was not certified by peer review) is the author/funder, who has granted bioRxiv a license to display the preprint in perpetuity. It is made available under aCC-BY-NC-ND 4.0 International license.

3.4 Descriptive statistics Mean

Table S17. Transforms - ICC Mean

transform	variable	n	mean	mean_z2r
pos	ICC.z	14112	0.564	0.5109392
exp	ICC.z	14112	0.561	0.5087190
abs	ICC.z	14112	0.560	0.5079774
div	ICC.z	14112	0.548	0.4990198

3.5 Descriptive statistics Median

Table S18. Transforms - ICC Median

transform	variable	n	median
pos	ICC	14112	0.474
abs	ICC	14112	0.465
exp	ICC	14112	0.398
div	ICC	14112	0.392

3.6 Friedman Test

Table S19. Transforms - Friedman Test

.y.	n	statistic	df	p	method
ICC.z	14112	480.0639	3	0	Friedman test

3.7 Friedman Test Effect size

Table S20. Transforms - Friedman Test Effect size

.y.	n	effsize	method	magnitude
ICC.z	14112	0.0113394	Kendall W	small

3.8 Paired Wilcoxon signed rank test

Table S21. Transforms - ICC group1 vs. group2

group1	group2	n1	statistic	alternative	p	p.adj	p.adj.signif
abs	div	14112	50949564	two.sided	0e+00	0.0e+00	****
abs	exp	14112	47946915	two.sided	8e-07	4.8e-06	****
abs	pos	14112	44430310	two.sided	3e-03	1.8e-02	*
div	exp	14112	35746898	two.sided	0e+00	0.0e+00	****
div	pos	14112	39669204	two.sided	0e+00	0.0e+00	****
exp	pos	14112	42638630	two.sided	0e+00	0.0e+00	****

bioRxiv preprint doi: https://doi.org/10.1101/2021.05.06.442886; this version posted September 4, 2021. The copyright holder for this preprint (which was not certified by peer review) is the author/funder, who has granted bioRxiv a license to display the preprint in perpetuity. It is made available under aCC-BY-NC-ND 4.0 International license.

Table S21. Transforms - ICC group1 vs. group2 *(continued)*

group1	group2	n1	statistic	alternative	p	p.adj	p.adj.signif

3.9 Significance map

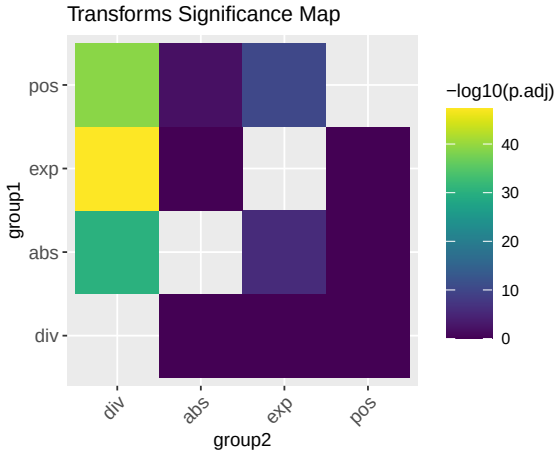

Fig. S18. Transforms - Significance Map

3.10 Effect size

Table S22. Transforms - Effect size

group1	group2	effsize	n1	n2	magnitude
abs	div	0.1009229	14112	14112	small
abs	exp	0.0439603	14112	14112	small
abs	pos	0.0232195	14112	14112	small
div	exp	0.1257376	14112	14112	small
div	pos	0.1139965	14112	14112	small
exp	pos	0.0582916	14112	14112	small

bioRxiv preprint doi: https://doi.org/10.1101/2021.05.06.442886; this version posted September 4, 2021. The copyright holder for this preprint (which was not certified by peer review) is the author/funder, who has granted bioRxiv a license to display the preprint in perpetuity. It is made available under aCC-BY-NC-ND 4.0 International license.

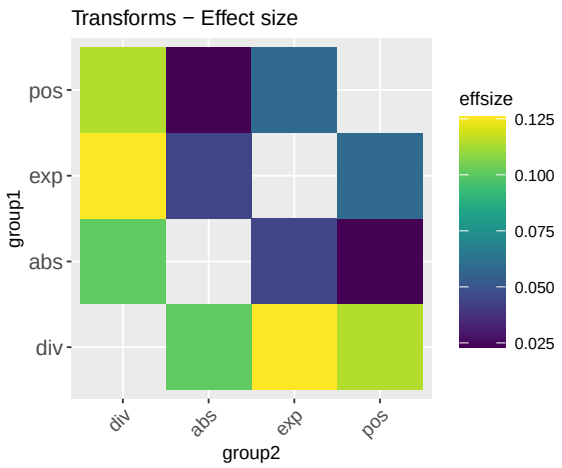

Fig. S19. Transforms - Effect size

4 Schemes - Edge Construction

4.1 ICC Density distribution

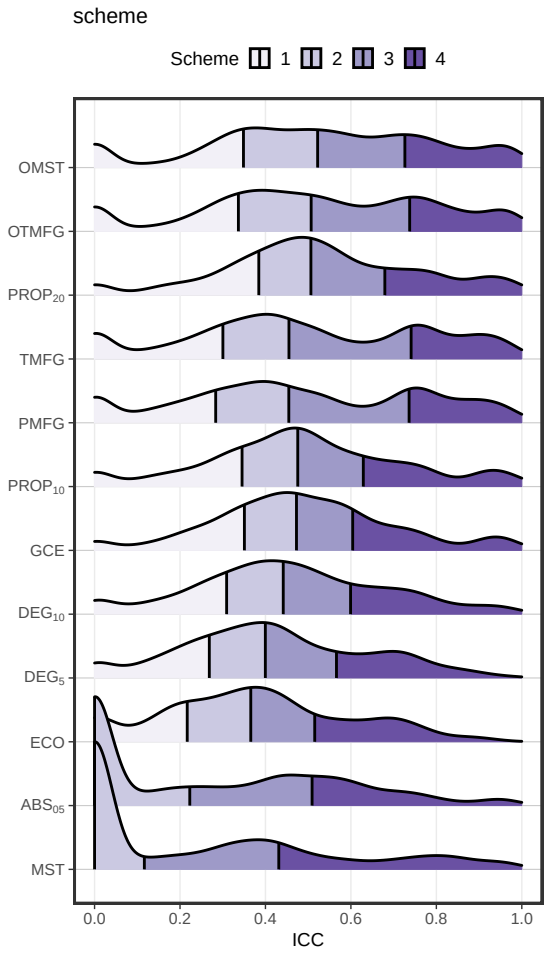

Fig. S20. Schemes - ICC Density distribution

bioRxiv preprint doi: https://doi.org/10.1101/2021.05.06.442886; this version posted September 4, 2021. The copyright holder for this preprint (which was not certified by peer review) is the author/funder, who has granted bioRxiv a license to display the preprint in perpetuity. It is made available under aCC-BY-NC-ND 4.0 International license.

4.2 Almost Perfect (ICCs > 0.8)

Table S23. Schemes - Number of ICCs > 0.8

scheme	n
OTMFG	781
TMFG	767
OMST	765
PMFG	737
$PROP_{20}$	632
$PROP_{10}$	445
MST	362
GCE	352
DEG_{15}	306
DEG_{5}	213
ABS_{05}	189
ECO	127

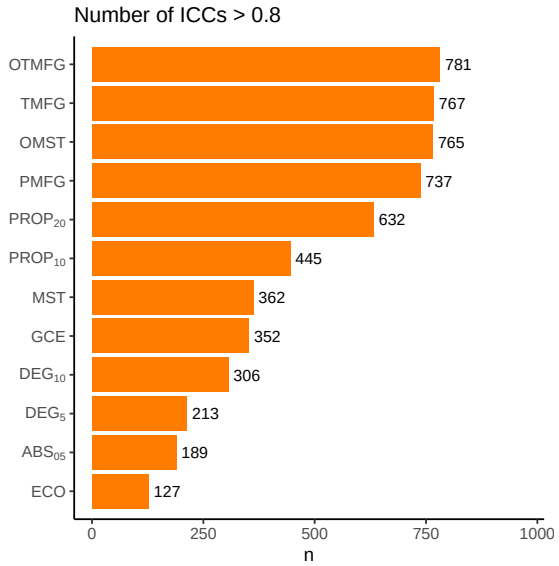

Fig. S21. Schemes - Number of ICC > 0.8

bioRxiv preprint doi: https://doi.org/10.1101/2021.05.06.442886; this version posted September 4, 2021. The copyright holder for this preprint (which was not certified by peer review) is the author/funder, who has granted bioRxiv a license to display the preprint in perpetuity. It is made available under aCC-BY-NC-ND 4.0 International license.

4.3 Substantial or Above (ICCs > 0.6)

Table S24. Schemes - Number of ICCs > 0.8

scheme	n
OMST	1860
OTMFG	1832
TMFG	1670
PMFG	1659
$PROP_{20}$	1564
$PROP_{10}$	1345
GCE	1210
DEG_{15}	1175
DEG_5	1035
ECO	837
MST	719
ABS_{05}	711

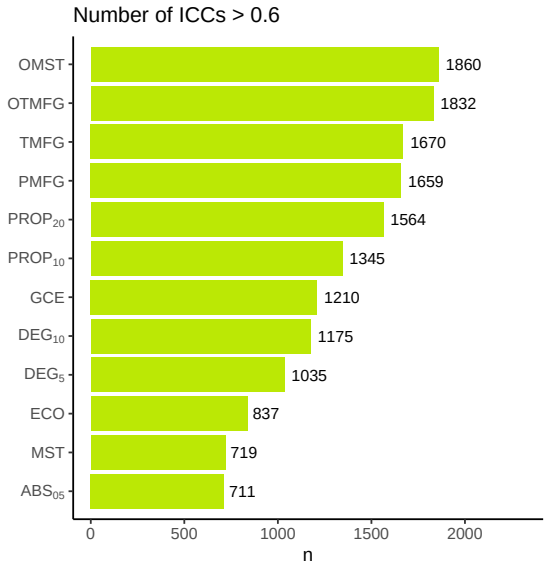

Fig. S22. Schemes - Number of ICC > 0.6

4.4 Varibility Changes

OMST, OTMFG, $PROP_{20}$, TMFG, PMFG, $PROP_{10}$

bioRxiv preprint doi: https://doi.org/10.1101/2021.05.06.442886; this version posted September 4, 2021. The copyright holder for this preprint (which was not certified by peer review) is the author/funder, who has granted bioRxiv a license to display the preprint in perpetuity. It is made available under aCC-BY-NC-ND 4.0 International license.

Fig. S23. Schemes - Variability Changes

bioRxiv preprint doi: https://doi.org/10.1101/2021.05.06.442886; this version posted September 4, 2021. The copyright holder for this preprint (which was not certified by peer review) is the author/funder, who has granted bioRxiv a license to display the preprint in perpetuity. It is made available under aCC-BY-NC-ND 4.0 International license.

4.5 Descriptive statistics Mean

Table S25. Schemes - ICC Mean

scheme	variable	n	mean	meanz2r
OMST	ICC.z	4704	0.706	0.6081624
OTMFG	ICC.z	4704	0.697	0.6024601
$PROP_{20}$	ICC.z	4704	0.683	0.5934662
TMFG	ICC.z	4704	0.647	0.5696469
PMFG	ICC.z	4704	0.635	0.5614855
$PROP_{10}$	ICC.z	4704	0.617	0.5490358
GCE	ICC.z	4704	0.595	0.5334821
DEG_{15}	ICC.z	4704	0.547	0.4982684
DEG_{5}	ICC.z	4704	0.486	0.4510359
ECO	ICC.z	4704	0.431	0.4061567
ABS_{05}	ICC.z	4704	0.337	0.3247965
MST	ICC.z	4704	0.319	0.3086024

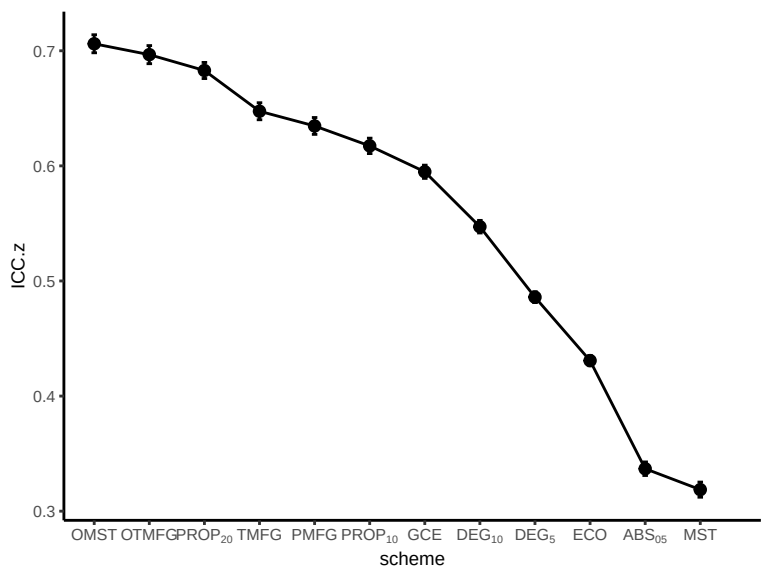

Fig. S24. Schemes - ICC mean and se

bioRxiv preprint doi: https://doi.org/10.1101/2021.05.06.442886; this version posted September 4, 2021. The copyright holder for this preprint (which was not certified by peer review) is the author/funder, who has granted bioRxiv a license to display the preprint in perpetuity. It is made available under aCC-BY-NC-ND 4.0 International license.

4.6 Descriptive statistics Median

Table S26. Schemes - ICC Median

scheme	variable	n	median
OMST	ICC	4704	0.522
OTMFG	ICC	4704	0.507
$PROP_{20}$	ICC	4704	0.506
$PROP_{10}$	ICC	4704	0.476
GCE	ICC	4704	0.473
PMFG	ICC	4704	0.455
TMFG	ICC	4704	0.455
DEG_{15}	ICC	4704	0.442
DEG_5	ICC	4704	0.400
ECO	ICC	4704	0.366
ABS_{05}	ICC	4704	0.223
MST	ICC	4704	0.117

4.7 Friedman Test

Table S27. Schemes - Friedman Test

.y.	n	statistic	df	p	method
ICC.z	4704	9784.317	11	0	Friedman test

4.8 Friedman Test Effect size

Table S28. Schemes - Friedman Test Effect size

.y.	n	effsize	method	magnitude
ICC.z	4704	0.1890909	Kendall W	small

4.9 Paired Wilcoxon signed rank test

Table S29. Schemes - ICC group1 vs. group2

group1	group2	n1	statistic	alternative	p	p.adj	p.adj.signif
ABS_{05}	DEG_{15}	4704	2694254	two.sided	0.00e+00	0.0000000	****
ABS_{05}	DEG_5	4704	3270500	two.sided	0.00e+00	0.0000000	****
ABS_{05}	ECO	4704	3943115	two.sided	0.00e+00	0.0000000	****
ABS_{05}	GCE	4704	2271646	two.sided	0.00e+00	0.0000000	****
ABS_{05}	MST	4704	4965999	two.sided	0.00e+00	0.0000003	****
ABS_{05}	OMST	4704	1467195	two.sided	0.00e+00	0.0000000	****
ABS_{05}	OTMFG	4704	1591487	two.sided	0.00e+00	0.0000000	****
ABS_{05}	PMFG	4704	2360874	two.sided	0.00e+00	0.0000000	****

bioRxiv preprint doi: https://doi.org/10.1101/2021.05.06.442886; this version posted September 4, 2021. The copyright holder for this preprint (which was not certified by peer review) is the author/funder, who has granted bioRxiv a license to display the preprint in perpetuity. It is made available under aCC-BY-NC-ND 4.0 International license.

Table S29. Schemes - ICC group1 vs. group2 *(continued)*

group1	group2	n1	statistic	alternative	p	p.adj	p.adj.signif
ABS_{05}	$PROP_{10}$	4704	2285372	two.sided	0.00e+00	0.0000000	****
ABS_{05}	$PROP_{20}$	4704	1672112	two.sided	0.00e+00	0.0000000	****
ABS_{05}	TMFG	4704	2232779	two.sided	0.00e+00	0.0000000	****
DEG_{15}	DEG_{5}	4704	7803402	two.sided	0.00e+00	0.0000000	****
DEG_{15}	ECO	4704	8444214	two.sided	0.00e+00	0.0000000	****
DEG_{15}	GCE	4704	4108796	two.sided	0.00e+00	0.0000000	****
DEG_{15}	MST	4704	8200729	two.sided	0.00e+00	0.0000000	****
DEG_{15}	OMST	4704	2665961	two.sided	0.00e+00	0.0000000	****
DEG_{15}	OTMFG	4704	2810801	two.sided	0.00e+00	0.0000000	****
DEG_{15}	PMFG	4704	4054470	two.sided	0.00e+00	0.0000000	****
DEG_{15}	$PROP_{10}$	4704	3445204	two.sided	0.00e+00	0.0000000	****
DEG_{15}	$PROP_{20}$	4704	2504887	two.sided	0.00e+00	0.0000000	****
DEG_{15}	TMFG	4704	3834624	two.sided	0.00e+00	0.0000000	****
DEG_{5}	ECO	4704	8040590	two.sided	0.00e+00	0.0000000	****
DEG_{5}	GCE	4704	3328222	two.sided	0.00e+00	0.0000000	****
DEG_{5}	MST	4704	7483490	two.sided	0.00e+00	0.0000000	****
DEG_{5}	OMST	4704	2135420	two.sided	0.00e+00	0.0000000	****
DEG_{5}	OTMFG	4704	2269997	two.sided	0.00e+00	0.0000000	****
DEG_{5}	PMFG	4704	2996624	two.sided	0.00e+00	0.0000000	****
DEG_{5}	$PROP_{10}$	4704	2832475	two.sided	0.00e+00	0.0000000	****
DEG_{5}	$PROP_{20}$	4704	1965712	two.sided	0.00e+00	0.0000000	****
DEG_{5}	TMFG	4704	2747205	two.sided	0.00e+00	0.0000000	****
ECO	GCE	4704	2438845	two.sided	0.00e+00	0.0000000	****
ECO	MST	4704	6602202	two.sided	0.00e+00	0.0000000	****
ECO	OMST	4704	1445475	two.sided	0.00e+00	0.0000000	****
ECO	OTMFG	4704	1561756	two.sided	0.00e+00	0.0000000	****
ECO	PMFG	4704	2072641	two.sided	0.00e+00	0.0000000	****
ECO	$PROP_{10}$	4704	2273516	two.sided	0.00e+00	0.0000000	****
ECO	$PROP_{20}$	4704	1494010	two.sided	0.00e+00	0.0000000	****
ECO	TMFG	4704	1864579	two.sided	0.00e+00	0.0000000	****
GCE	MST	4704	8955851	two.sided	0.00e+00	0.0000000	****
GCE	OMST	4704	3276387	two.sided	0.00e+00	0.0000000	****
GCE	OTMFG	4704	3459105	two.sided	0.00e+00	0.0000000	****
GCE	PMFG	4704	5127650	two.sided	2.85e-05	0.0018810	**
GCE	$PROP_{10}$	4704	5081947	two.sided	3.30e-06	0.0002158	***
GCE	$PROP_{20}$	4704	3034877	two.sided	0.00e+00	0.0000000	****
GCE	TMFG	4704	4875617	two.sided	0.00e+00	0.0000000	****
MST	OMST	4704	712172	two.sided	0.00e+00	0.0000000	****
MST	OTMFG	4704	795758	two.sided	0.00e+00	0.0000000	****
MST	PMFG	4704	1340430	two.sided	0.00e+00	0.0000000	****
MST	$PROP_{10}$	4704	1771350	two.sided	0.00e+00	0.0000000	****
MST	$PROP_{20}$	4704	1149079	two.sided	0.00e+00	0.0000000	****
MST	TMFG	4704	1164787	two.sided	0.00e+00	0.0000000	****
OMST	OTMFG	4704	5863222	two.sided	0.00e+00	0.0000000	****
OMST	PMFG	4704	7183474	two.sided	0.00e+00	0.0000000	****
OMST	$PROP_{10}$	4704	7386941	two.sided	0.00e+00	0.0000000	****
OMST	$PROP_{20}$	4704	6196410	two.sided	0.00e+00	0.0000000	****

bioRxiv preprint doi: https://doi.org/10.1101/2021.05.06.442886; this version posted September 4, 2021. The copyright holder for this preprint (which was not certified by peer review) is the author/funder, who has granted bioRxiv a license to display the preprint in perpetuity. It is made available under aCC-BY-NC-ND 4.0 International license.

Table S29. Schemes - ICC group1 vs. group2 *(continued)*

group1	group2	n1	statistic	alternative	p	p.adj	p.adj.signif
OMST	TMFG	4704	6887505	two.sided	0.00e+00	0.0000000	****
OTMFG	PMFG	4704	7021466	two.sided	0.00e+00	0.0000000	****
OTMFG	$PROP_{10}$	4704	7154543	two.sided	0.00e+00	0.0000000	****
OTMFG	$PROP_{20}$	4704	5995825	two.sided	0.00e+00	0.0000028	****
OTMFG	TMFG	4704	6682826	two.sided	0.00e+00	0.0000000	****
PMFG	$PROP_{10}$	4704	5618652	two.sided	1.45e-01	1.0000000	ns
PMFG	$PROP_{20}$	4704	4515273	two.sided	0.00e+00	0.0000000	****
PMFG	TMFG	4704	4119850	two.sided	0.00e+00	0.0000000	****
$PROP_{10}$	$PROP_{20}$	4704	2886243	two.sided	0.00e+00	0.0000000	****
$PROP_{10}$	TMFG	4704	5169273	two.sided	4.31e-04	0.0284460	*
$PROP_{20}$	TMFG	4704	6289407	two.sided	0.00e+00	0.0000000	****

4.10 Significance map

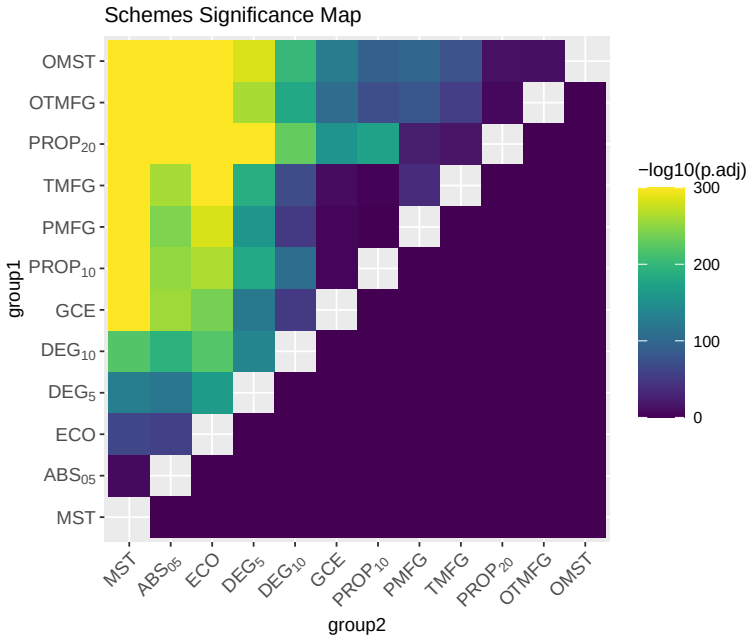

Fig. S25. Schemes - Significance Map

4.11 Effect size

Table S30. Schemes - Effect size

group1	group2	effsize	n1	n2	magnitude
ABS_{05}	DEG_{15}	0.4336085	4704	4704	moderate
ABS_{05}	DEG_5	0.3385623	4704	4704	moderate
ABS_{05}	ECO	0.2339104	4704	4704	small
ABS_{05}	GCE	0.5006219	4704	4704	large
ABS_{05}	MST	0.1010940	4704	4704	small

bioRxiv preprint doi: https://doi.org/10.1101/2021.05.06.442886; this version posted September 4, 2021. The copyright holder for this preprint (which was not certified by peer review) is the author/funder, who has granted bioRxiv a license to display the preprint in perpetuity. It is made available under aCC-BY-NC-ND 4.0 International license.

Table S30. Schemes - Effect size *(continued)*

group1	group2	effsize	n1	n2	magnitude
ABS_{05}	OMST	0.6272196	4704	4704	large
ABS_{05}	OTMFG	0.6064118	4704	4704	large
ABS_{05}	PMFG	0.4861088	4704	4704	moderate
ABS_{05}	$PROP_{10}$	0.4962328	4704	4704	moderate
ABS_{05}	$PROP_{20}$	0.5953801	4704	4704	large
ABS_{05}	TMFG	0.5043800	4704	4704	large
DEG_{15}	DEG_{5}	0.3656085	4704	4704	moderate
DEG_{15}	ECO	0.4643143	4704	4704	moderate
DEG_{15}	GCE	0.2213037	4704	4704	small
DEG_{15}	MST	0.4629302	4704	4704	moderate
DEG_{15}	OMST	0.4439416	4704	4704	moderate
DEG_{15}	OTMFG	0.4196640	4704	4704	moderate
DEG_{15}	PMFG	0.2243101	4704	4704	small
DEG_{15}	$PROP_{10}$	0.3230340	4704	4704	moderate
DEG_{15}	$PROP_{20}$	0.4729914	4704	4704	moderate
DEG_{15}	TMFG	0.2592393	4704	4704	small
DEG_{5}	ECO	0.4011082	4704	4704	moderate
DEG_{5}	GCE	0.3443975	4704	4704	moderate
DEG_{5}	MST	0.3530459	4704	4704	moderate
DEG_{5}	OMST	0.5266713	4704	4704	large
DEG_{5}	OTMFG	0.5058619	4704	4704	large
DEG_{5}	PMFG	0.3921309	4704	4704	moderate
DEG_{5}	$PROP_{10}$	0.4209417	4704	4704	moderate
DEG_{5}	$PROP_{20}$	0.5574678	4704	4704	large
DEG_{5}	TMFG	0.4294553	4704	4704	moderate
ECO	GCE	0.4829184	4704	4704	moderate
ECO	MST	0.2472343	4704	4704	small
ECO	OMST	0.6246376	4704	4704	large
ECO	OTMFG	0.6073007	4704	4704	large
ECO	PMFG	0.5251605	4704	4704	large
ECO	$PROP_{10}$	0.5082960	4704	4704	large
ECO	$PROP_{20}$	0.6300488	4704	4704	large
ECO	TMFG	0.5579538	4704	4704	large
GCE	MST	0.5682424	4704	4704	large
GCE	OMST	0.3497301	4704	4704	moderate
GCE	OTMFG	0.3209678	4704	4704	moderate
GCE	PMFG	0.0609041	4704	4704	small
GCE	$PROP_{10}$	0.0677587	4704	4704	small
GCE	$PROP_{20}$	0.3900709	4704	4704	moderate
GCE	TMFG	0.0968897	4704	4704	small
MST	OMST	0.7314210	4704	4704	large

bioRxiv preprint doi: https://doi.org/10.1101/2021.05.06.442886; this version posted September 4, 2021. The copyright holder for this preprint (which was not certified by peer review) is the author/funder, who has granted bioRxiv a license to display the preprint in perpetuity. It is made available under aCC-BY-NC-ND 4.0 International license.

Table S30. Schemes - Effect size *(continued)*

group1	group2	effsize	n1	n2	magnitude
MST	OTMFG	0.7144886	4704	4704	large
MST	PMFG	0.6232274	4704	4704	large
MST	$PROP_{10}$	0.5694680	4704	4704	large
MST	$PROP_{20}$	0.6742707	4704	4704	large
MST	TMFG	0.6506873	4704	4704	large
OMST	OTMFG	0.1072281	4704	4704	small
OMST	PMFG	0.3108939	4704	4704	moderate
OMST	$PROP_{10}$	0.2977166	4704	4704	small
OMST	$PROP_{20}$	0.1111673	4704	4704	small
OMST	TMFG	0.2713060	4704	4704	small
OTMFG	PMFG	0.2809687	4704	4704	small
OTMFG	$PROP_{10}$	0.2638212	4704	4704	small
OTMFG	$PROP_{20}$	0.0798667	4704	4704	small
OTMFG	TMFG	0.2305216	4704	4704	small
PMFG	$PROP_{10}$	0.0210514	4704	4704	small
PMFG	$PROP_{20}$	0.1549509	4704	4704	small
PMFG	TMFG	0.1861855	4704	4704	small
$PROP_{10}$	$PROP_{20}$	0.4119006	4704	4704	moderate
$PROP_{10}$	TMFG	0.0511920	4704	4704	small
$PROP_{20}$	TMFG	0.1263285	4704	4704	small

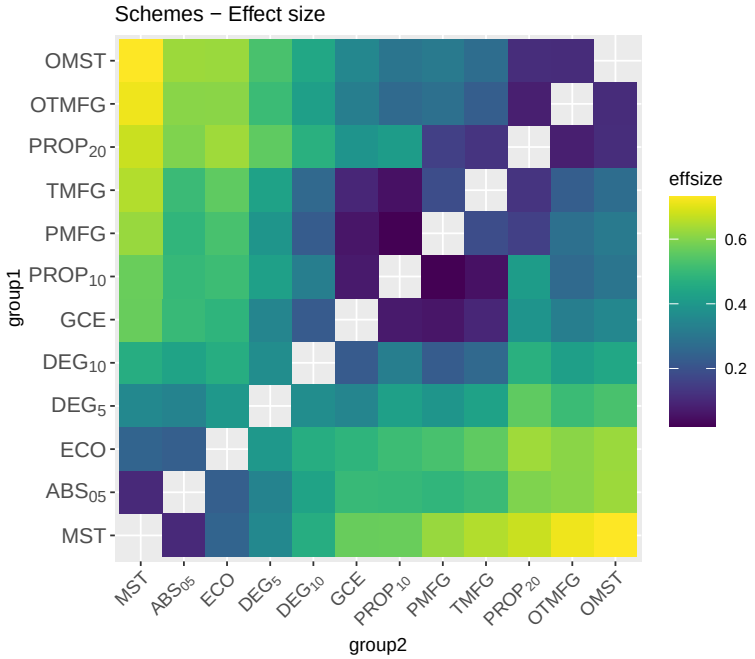

Fig. S26. Schemes - Effect size

bioRxiv preprint doi: https://doi.org/10.1101/2021.05.06.442886; this version posted September 4, 2021. The copyright holder for this preprint (which was not certified by peer review) is the author/funder, who has granted bioRxiv a license to display the preprint in perpetuity. It is made available under aCC-BY-NC-ND 4.0 International license.

5 Metrics - Network Analysis

5.1 Metrics

Table S31. Brief descriptions of the network metrics examined

Level	Measure	Attribute	Character
Global	basic	degree	k
		number of edge	n_e
		density	d
	integration	global efficiency	Eg
		average shortest path length	Lp_a
		average nodal path length	Lp_b
		pseudo diameter	D
	segregation	clusteringcoef by BCT toolbox	Cp_a
		clusteringcoef by Graph-tool	Cp_b
		local efficiency algorithm 1 by BCT toolbox	$Eloc_1$
		local efficiency algorithm 2 by BCT toolbox	$Eloc_2$
		modularity	Q
		transitivity by BCT toolbox	Tr_a
		transitivity by Graph-tool	Tr_b
	centrality	average betweenness	Bc
		average eigenvector	Ec
		average pagerank	Pc
		average subgraph	Sc
	resilience	assortativity	r
		scalar assortativity	r_s
		synchronizability	S
		average resolvent	Rv
Nodal	integration	nodal path length	Lp_a
		local path length	Lp_b
	segregation	clustering coefficient by BCT toolbox	Cp_a
		clustering coefficient Graph-tool	Cp_b
		local efficiency 1 by BCT toolbox	$Eloc_1$
		local efficiency 2 by BCT toolbox	$Eloc_2$
		nodal efficiency	E_{nodal}
	centrality	degree centrality	Dc
		betweeness centrality	Bc
		eigenvector centrality	Ec
		pagerank centrality	Pc
		subgraph centrality	Sc
		resolvent centrality	Rc

Superscript b (eg. Eg^b) is used for the binary graphs, superscript w (eg. Eg^w) is used for the weighted graphs, and superscript n (eg. Eg^n) is used for the normalized weighted graphs.

bioRxiv preprint doi: https://doi.org/10.1101/2021.05.06.442886; this version posted September 4, 2021. The copyright holder for this preprint (which was not certified by peer review) is the author/funder, who has granted bioRxiv a license to display the preprint in perpetuity. It is made available under aCC-BY-NC-ND 4.0 International license.

5.2 ICC Density distribution

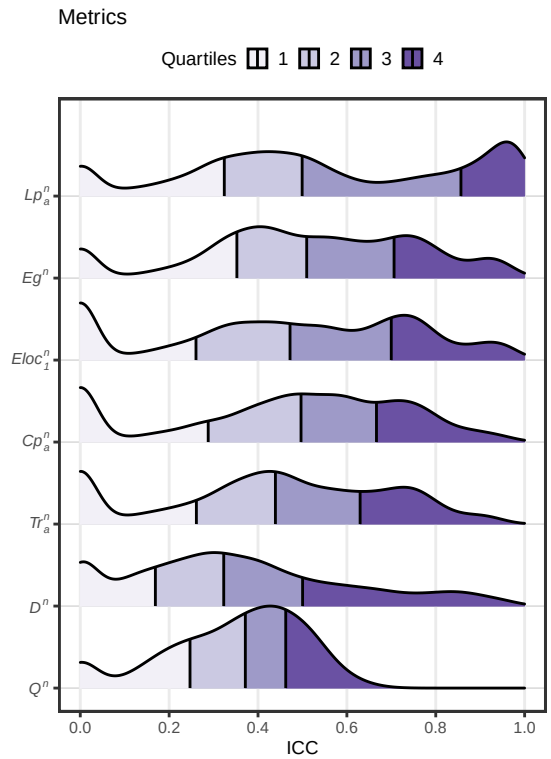

Fig. S27. Metrics - Density distribution

5.3 Almost Perfect (ICCs > 0.8)

Table S32. Metrics - Number of ICCs > 0.8

	character	n
3	Lp_a^n	2350
4	Eg^n	924
2	$Eloc_1^n$	835
1	Cp_a^n	575
5	D^n	559
6	Tr_a^n	433

bioRxiv preprint doi: https://doi.org/10.1101/2021.05.06.442886; this version posted September 4, 2021. The copyright holder for this preprint (which was not certified by peer review) is the author/funder, who has granted bioRxiv a license to display the preprint in perpetuity. It is made available under aCC-BY-NC-ND 4.0 International license.

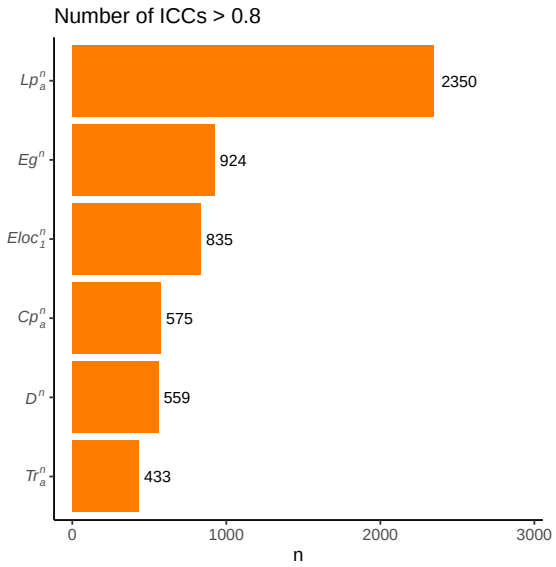

Fig. S28. Metrics - Number of ICC > 0.8

5.4 Substantial or Above (ICCs > 0.6)

Table S33. Metrics - Number of ICCs > 0.6

	character	n
3	Lp_a^n	3194
4	Eg^n	3032
2	$Eloc_1^n$	2886
1	Cp_a^n	2709
7	Tr_a^n	2273
6	D^n	1383
5	Q^n	140

bioRxiv preprint doi: https://doi.org/10.1101/2021.05.06.442886; this version posted September 4, 2021. The copyright holder for this preprint (which was not certified by peer review) is the author/funder, who has granted bioRxiv a license to display the preprint in perpetuity. It is made available under aCC-BY-NC-ND 4.0 International license.

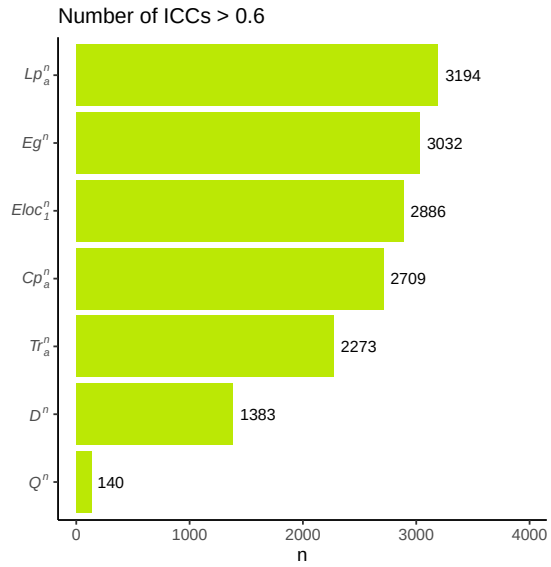

Fig. S29. Metrics - Number of ICC > 0.6

5.5 Descriptive statistics Mean

Table S34. Metrics - ICC Mean

character	n	meanz2r
Lp_a^n	8064	0.6847483
Eg^n	8064	0.5628534
$Eloc_1^n$	8064	0.5241176
Cp_a^n	8064	0.5057482
Tr_a^n	8064	0.4683854
D^n	8064	0.3952442
Q^n	8064	0.3531167

5.6 Descriptive statistics Median

Table S35. Metrics - ICC Median

character	n	median
Eg^n	8064	0.510
Lp_a^n	8064	0.499
Cp_a^n	8064	0.497
$Eloc_1^n$	8064	0.472
Tr_a^n	8064	0.439
Q^n	8064	0.371
D^n	8064	0.323

5.7 Paired Wilcoxon signed rank test

bioRxiv preprint doi: https://doi.org/10.1101/2021.05.06.442886; this version posted September 4, 2021. The copyright holder for this preprint (which was not certified by peer review) is the author/funder, who has granted bioRxiv a license to display the preprint in perpetuity. It is made available under aCC-BY-NC-ND 4.0 International license.

Table S36. Metrics - ICC group1 vs. group2

character1	character2	n1	statistic	alternative	p	p.adj	p.adj.signif
Cp_a^n	$Eloc_1^n$	8064	12227711	two.sided	9.20e-06	0.0001934	***
Cp_a^n	Lp_a^n	8064	8726636	two.sided	0.00e+00	0.0000000	****
Cp_a^n	Eg^n	8064	13406103	two.sided	0.00e+00	0.0000000	****
Cp_a^n	Q^n	8064	23845905	two.sided	0.00e+00	0.0000000	****
Cp_a^n	D^n	8064	23503271	two.sided	0.00e+00	0.0000000	****
Cp_a^n	Tr_a^n	8064	18879595	two.sided	0.00e+00	0.0000000	****
$Eloc_1^n$	Lp_a^n	8064	8214982	two.sided	0.00e+00	0.0000000	****
$Eloc_1^n$	Eg^n	8064	13804539	two.sided	0.00e+00	0.0000000	****
$Eloc_1^n$	Q^n	8064	23296271	two.sided	0.00e+00	0.0000000	****
$Eloc_1^n$	D^n	8064	24208558	two.sided	0.00e+00	0.0000000	****
$Eloc_1^n$	Tr_a^n	8064	17771904	two.sided	0.00e+00	0.0000000	****
Lp_a^n	Eg^n	8064	21277439	two.sided	0.00e+00	0.0000000	****
Lp_a^n	Q^n	8064	26286171	two.sided	0.00e+00	0.0000000	****
Lp_a^n	D^n	8064	28471330	two.sided	0.00e+00	0.0000000	****
Lp_a^n	Tr_a^n	8064	24806988	two.sided	0.00e+00	0.0000000	****
Eg^n	Q^n	8064	26666127	two.sided	0.00e+00	0.0000000	****
Eg^n	D^n	8064	27744888	two.sided	0.00e+00	0.0000000	****
Eg^n	Tr_a^n	8064	21280096	two.sided	0.00e+00	0.0000000	****
Q^n	D^n	8064	15808230	two.sided	3.65e-01	1.0000000	ns
Q^n	Tr_a^n	8064	9856527	two.sided	0.00e+00	0.0000000	****
D^n	Tr_a^n	8064	8856878	two.sided	0.00e+00	0.0000000	****

5.8 Significance map

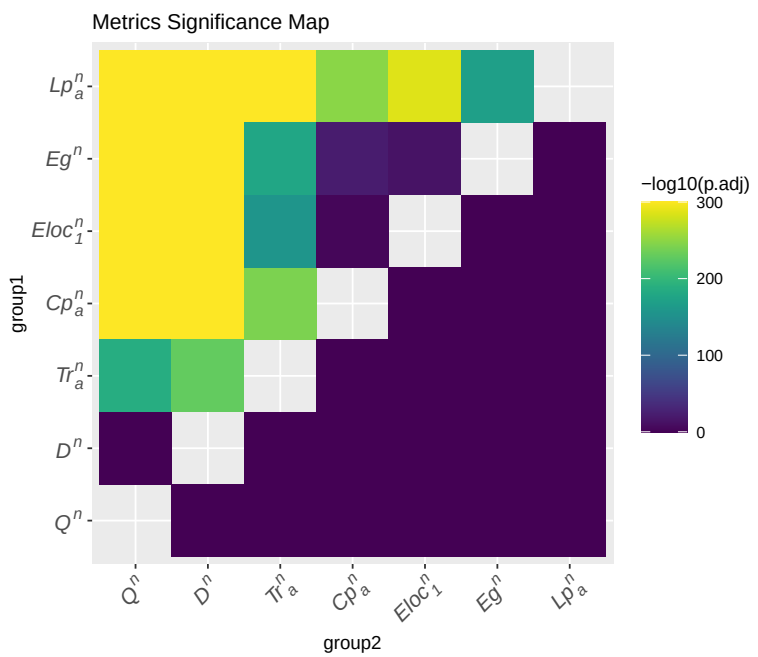

Fig. S30. Metrics - Significance Map

bioRxiv preprint doi: https://doi.org/10.1101/2021.05.06.442886; this version posted September 4, 2021. The copyright holder for this preprint (which was not certified by peer review) is the author/funder, who has granted bioRxiv a license to display the preprint in perpetuity. It is made available under aCC-BY-NC-ND 4.0 International license.

5.9 Effect size

Table S37. Metrics - Effect size

character1	character2	effsize	n1	n2	magnitude
Cp_a^n	$Eloc_1^n$	0.0442149	8064	8064	small
Cp_a^n	Lp_a^n	0.3729141	8064	8064	moderate
Cp_a^n	Eg^n	0.1094179	8064	8064	small
Cp_a^n	Q^n	0.4462449	8064	8064	moderate
Cp_a^n	D^n	0.4629948	8064	8064	moderate
Cp_a^n	Tr_a^n	0.3823045	8064	8064	moderate
$Eloc_1^n$	Lp_a^n	0.4014701	8064	8064	moderate
$Eloc_1^n$	Eg^n	0.0895200	8064	8064	small
$Eloc_1^n$	Q^n	0.4124881	8064	8064	moderate
$Eloc_1^n$	D^n	0.5027420	8064	8064	large
$Eloc_1^n$	Tr_a^n	0.3025436	8064	8064	moderate
Lp_a^n	Eg^n	0.3055529	8064	8064	moderate
Lp_a^n	Q^n	0.5641222	8064	8064	large
Lp_a^n	D^n	0.7079035	8064	8064	large
Lp_a^n	Tr_a^n	0.5101946	8064	8064	large
Eg^n	Q^n	0.6054757	8064	8064	large
Eg^n	D^n	0.6915405	8064	8064	large
Eg^n	Tr_a^n	0.3167091	8064	8064	moderate
Q^n	D^n	0.0132182	8064	8064	small
Q^n	Tr_a^n	0.3249259	8064	8064	moderate
D^n	Tr_a^n	0.3637976	8064	8064	moderate

bioRxiv preprint doi: https://doi.org/10.1101/2021.05.06.442886; this version posted September 4, 2021. The copyright holder for this preprint (which was not certified by peer review) is the author/funder, who has granted bioRxiv a license to display the preprint in perpetuity. It is made available under aCC-BY-NC-ND 4.0 International license.

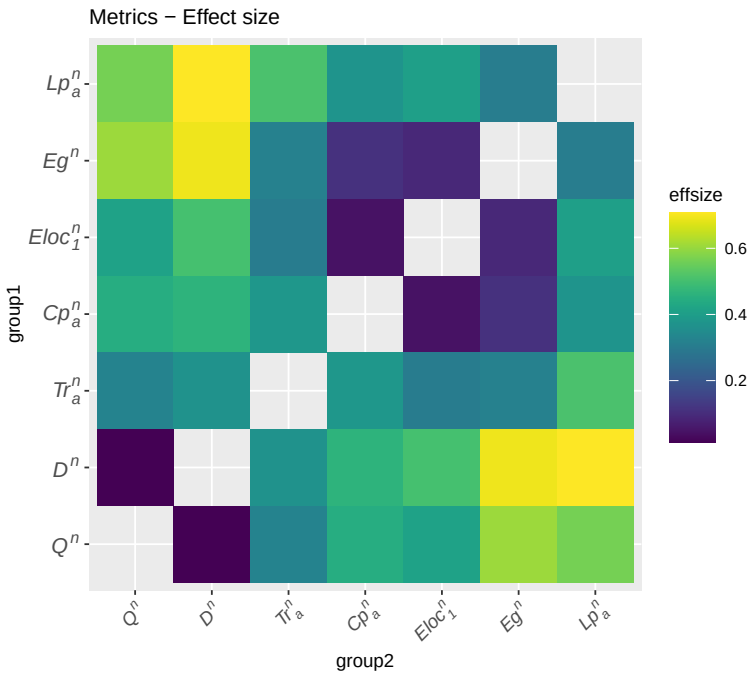

Fig. S31. Metrics - Effect size

bioRxiv preprint doi: https://doi.org/10.1101/2021.05.06.442886; this version posted September 4, 2021. The copyright holder for this preprint (which was not certified by peer review) is the author/funder, who has granted bioRxiv a license to display the preprint in perpetuity. It is made available under aCC-BY-NC-ND 4.0 International license.

6 More Metrics - Network Analysis

6.1 ICC Density distribution

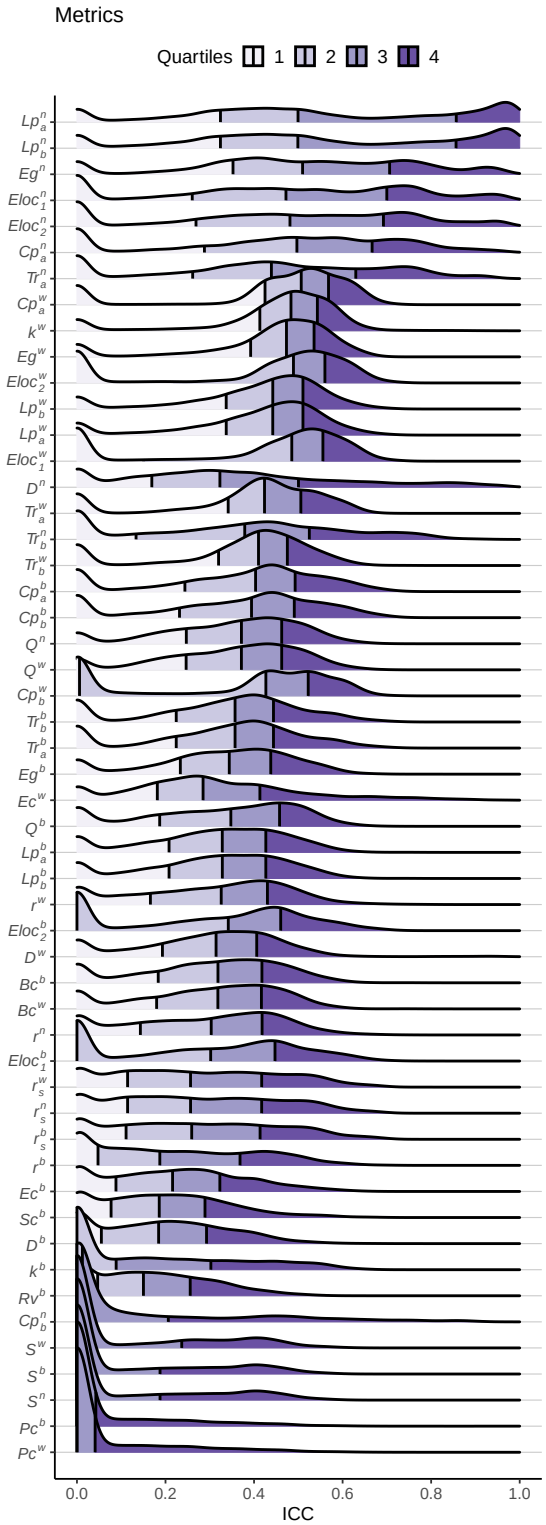

Fig. S32. Metrics - Density distribution

bioRxiv preprint doi: https://doi.org/10.1101/2021.05.06.442886; this version posted September 4, 2021. The copyright holder for this preprint (which was not certified by peer review) is the author/funder, who has granted bioRxiv a license to display the preprint in perpetuity. It is made available under aCC-BY-NC-ND 4.0 International license.

6.2 Almost Perfect (ICCs > 0.8)

Table S38. Metrics - Number of ICCs > 0.8

	character	n
14	Lp_a^n	2350
11	Lp_b^n	2349
16	Eg^n	924
8	$Eloc_1^n$	835
9	$Eloc_2^n$	792
5	Cp_a^n	575
17	D^n	559
21	Tr_a^n	433
6	Ec^w	137
19	Tr_b^n	131
4	Cp_b^n	114
18	D^w	57
15	k^w	27
12	Pc^b	4
1	r^w	2
2	Bc^b	1
3	Bc^w	1
7	$Eloc_1^b$	1
10	Lp_b^b	1
13	Lp_a^b	1
20	Tr_b^w	1

bioRxiv preprint doi: https://doi.org/10.1101/2021.05.06.442886; this version posted September 4, 2021. The copyright holder for this preprint (which was not certified by peer review) is the author/funder, who has granted bioRxiv a license to display the preprint in perpetuity. It is made available under aCC-BY-NC-ND 4.0 International license.

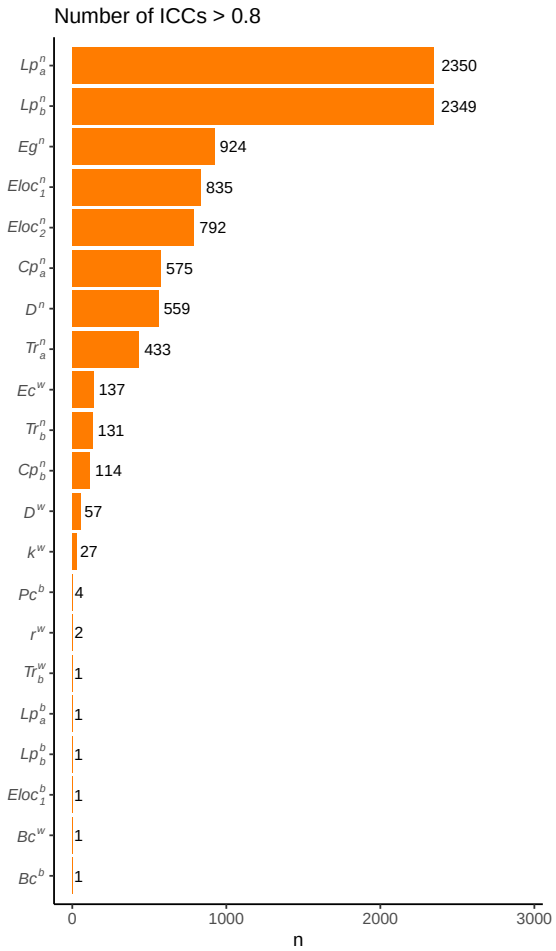

Fig. S33. Metrics - Number of ICC > 0.8

6.3 Substantial or Above (ICCs > 0.6)

Table S39. Metrics - Number of ICCs > 0.6

	character	n
27	Lp_a^n	3194
21	Lp_b^n	3190
33	Eg^n	3032
18	$Eloc_2^n$	2913
15	$Eloc_1^n$	2886
10	Cp_a^n	2709
51	Tr_a^n	2273
39	D^n	1383
48	Tr_b^n	1316
11	Cp_a^w	1302
19	$Eloc_2^w$	1085
16	$Eloc_1^w$	998
13	Ec^w	664

bioRxiv preprint doi: https://doi.org/10.1101/2021.05.06.442886; this version posted September 4, 2021. The copyright holder for this preprint (which was not certified by peer review) is the author/funder, who has granted bioRxiv a license to display the preprint in perpetuity. It is made available under aCC-BY-NC-ND 4.0 International license.

Table S39. Metrics - Number of ICCs > 0.6 *(continued)*

	character	n
9	Cp_a^b	603
6	Cp_b^b	595
8	Cp_b^w	592
31	k^w	481
34	Eg^w	467
7	Cp_b^n	463
52	Tr_a^w	385
22	Lp_b^w	375
28	Lp_a^w	375
17	$Eloc_2^b$	345
14	$Eloc_1^b$	314
47	Tr_b^b	276
50	Tr_a^b	276
41	r_s^b	247
42	r_s^n	229
43	r_s^w	229
49	Tr_b^w	153
3	r^w	148
36	Q^n	140
37	Q^w	140
35	Q^b	109
40	D^w	107
2	r^n	100
32	Eg^b	83
1	r^b	81
20	Lp_b^b	67
26	Lp_a^b	67
30	k^b	64
4	Bc^b	50
12	Ec^b	40
29	Sc^b	40
5	Bc^w	32
23	Pc^b	18
38	D^b	16
24	Pc^w	14
46	S^w	12
25	Rv^b	2
44	S^b	2
45	S^n	2

bioRxiv preprint doi: https://doi.org/10.1101/2021.05.06.442886; this version posted September 4, 2021. The copyright holder for this preprint (which was not certified by peer review) is the author/funder, who has granted bioRxiv a license to display the preprint in perpetuity. It is made available under aCC-BY-NC-ND 4.0 International license.

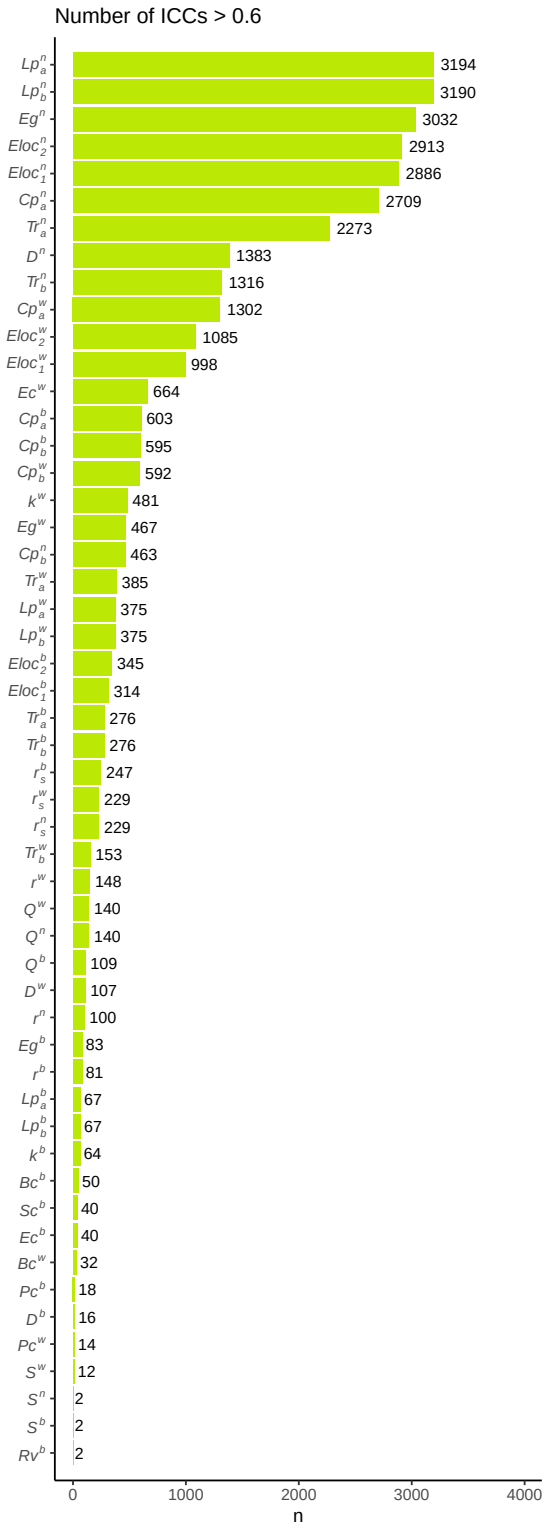

Fig. S34. Metrics - Number of ICC > 0.6

6.4 Descriptive statistics Mean

bioRxiv preprint doi: https://doi.org/10.1101/2021.05.06.442886; this version posted September 4, 2021. The copyright holder for this preprint (which was not certified by peer review) is the author/funder, who has granted bioRxiv a license to display the preprint in perpetuity. It is made available under aCC-BY-NC-ND 4.0 International license.

Table S40. Metrics - ICC Mean

character	n	meanz2r
Lp_a^n	8064	0.6847483
Lp_b^n	8064	0.6842168
Eg^n	8064	0.5628534
$Eloc_1^n$	8064	0.5241176
$Eloc_2^n$	8064	0.5219382
Cp_a^n	8064	0.5057482
Tr_a^n	8064	0.4683854
Cp_a^w	8064	0.4621172
k^w	8064	0.4542164
Eg^w	8064	0.4381993
$Eloc_2^w$	8064	0.4144730
Lp_b^w	8064	0.4094914
Lp_a^w	8064	0.4094914
$Eloc_1^w$	8064	0.4053213
D^n	8064	0.3952442
Tr_a^w	8064	0.3935553
Tr_b^n	8064	0.3790930
Tr_b^w	8064	0.3704978
Cp_a^b	8064	0.3679068
Cp_b^b	8064	0.3627075
Q^n	8064	0.3531167
Q^w	8064	0.3531167
Cp_b^w	8064	0.3487325
Tr_b^b	8064	0.3346006
Tr_a^b	8064	0.3346006
Eg^b	8064	0.3301530
Ec^w	8064	0.3265843
Q^b	8064	0.3239017
Lp_b^b	8064	0.3140209
Lp_a^b	8064	0.3140209
r^w	8064	0.3067918
$Eloc_2^b$	8064	0.3049789
D^w	8064	0.3031638
Bc^b	8064	0.3013466
Bc^w	8064	0.2986165
r^n	8064	0.2885648
$Eloc_1^b$	8064	0.2858122
r_s^n	8064	0.2802930
r_s^w	8064	0.2802930
r_s^b	8064	0.2784491
r^b	8064	0.2231797

bioRxiv preprint doi: https://doi.org/10.1101/2021.05.06.442886; this version posted September 4, 2021. The copyright holder for this preprint (which was not certified by peer review) is the author/funder, who has granted bioRxiv a license to display the preprint in perpetuity. It is made available under aCC-BY-NC-ND 4.0 International license.

Table S40. Metrics - ICC Mean *(continued)*

character	n	meanz2r
Ec^b	8064	0.2222293
Sc^b	8064	0.1983362
D^b	8064	0.1916023
k^b	8064	0.1712945
Rv^b	8064	0.1664371
Cp_b^n	8064	0.1566982
S^w	8064	0.1135087
S^b	8064	0.1036267
S^n	8064	0.1036267
Pc^b	8064	0.0629168
Pc^w	8064	0.0619207

6.5 Descriptive statistics Median

Table S41. Metrics - ICC Median

character	n	median
Eg^n	8064	0.510
Cp_a^w	8064	0.507
Lp_b^n	8064	0.499
Lp_a^n	8064	0.499
Cp_a^n	8064	0.497
$Eloc_2^w$	8064	0.489
$Eloc_1^w$	8064	0.485
k^w	8064	0.483
$Eloc_2^n$	8064	0.481
Eg^w	8064	0.473
$Eloc_1^n$	8064	0.472
Lp_b^w	8064	0.442
Lp_a^w	8064	0.442
Tr_a^n	8064	0.439
Cp_b^w	8064	0.427
Tr_a^w	8064	0.424
Tr_b^w	8064	0.410
Cp_a^b	8064	0.403
Cp_b^b	8064	0.394
Tr_b^n	8064	0.379
Q^n	8064	0.371
Q^w	8064	0.371
Tr_b^b	8064	0.357
Tr_a^b	8064	0.357
Q^b	8064	0.348

bioRxiv preprint doi: https://doi.org/10.1101/2021.05.06.442886; this version posted September 4, 2021. The copyright holder for this preprint (which was not certified by peer review) is the author/funder, who has granted bioRxiv a license to display the preprint in perpetuity. It is made available under aCC-BY-NC-ND 4.0 International license.

Table S41. Metrics - ICC Median *(continued)*

character	n	median
Eg^b	8064	0.344
$Eloc_2^b$	8064	0.342
Lp_b^b	8064	0.328
Lp_a^b	8064	0.328
r^w	8064	0.326
D^n	8064	0.323
Bc^b	8064	0.318
Bc^w	8064	0.318
D^w	8064	0.314
r^n	8064	0.303
$Eloc_1^b$	8064	0.302
Ec^w	8064	0.285
r_s^b	8064	0.259
r_s^n	8064	0.257
r_s^w	8064	0.257
Ec^b	8064	0.216
r^b	8064	0.187
Sc^b	8064	0.186
D^b	8064	0.184
Rv^b	8064	0.150
k^b	8064	0.089
Cp_b^n	8064	0.012
Pc^b	8064	0.000
Pc^w	8064	0.000
S^b	8064	0.000
S^n	8064	0.000
S^w	8064	0.000

bioRxiv preprint doi: https://doi.org/10.1101/2021.05.06.442886; this version posted September 4, 2021. The copyright holder for this preprint (which was not certified by peer review) is the author/funder, who has granted bioRxiv a license to display the preprint in perpetuity. It is made available under aCC-BY-NC-ND 4.0 International license.

6.6 Significance map

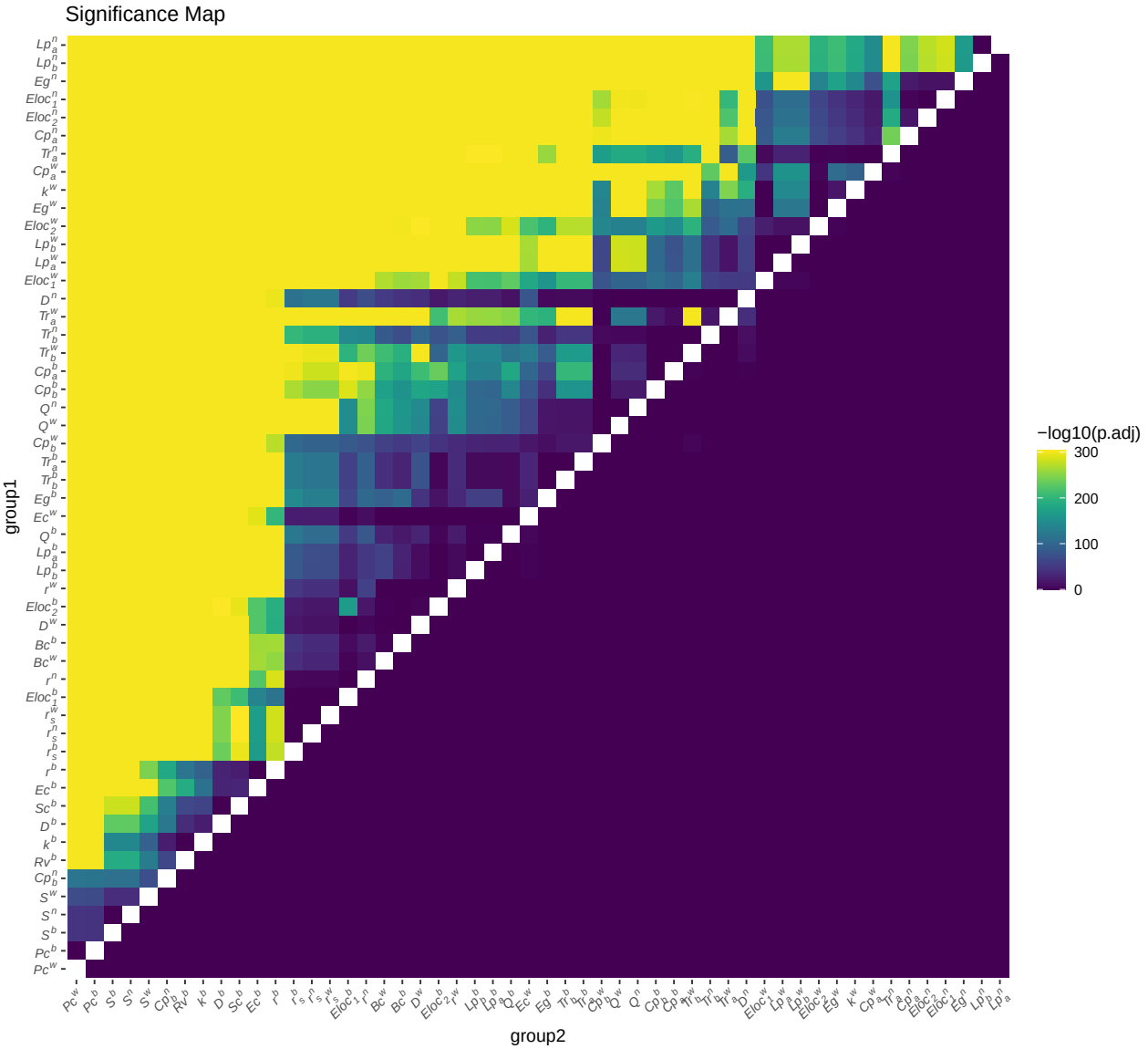

Fig. S35. Metrics - Significance Map